

See discussions, stats, and author profiles for this publication at: <https://www.researchgate.net/publication/302546326>

Underwater Acoustics

Chapter · January 2014

DOI: 10.1007/978-1-4939-0755-7_5

CITATIONS
16

READS
16,561

2 authors, including:



Philippe Roux
University Grenoble Alpes
470 PUBLICATIONS 10,803 CITATIONS

[SEE PROFILE](#)

Some of the authors of this publication are also working on these related projects:



Old Faithful [View project](#)



Seismic tomography of the San Jacinto Fault zone [View project](#)

Underwater Acoustics

William A. Kuperman, Philippe Roux

It is well established that sound waves, compared to electromagnetic waves, propagate long distances in the ocean. Hence, in the ocean as opposed to air or a vacuum, one uses sound navigation and ranging (SONAR) instead of radar, acoustic communication instead of radio, and acoustic imaging and tomography instead of microwave or optical imaging or X-ray tomography. Underwater acoustics is the science of sound in water (most commonly in the ocean) and encompasses not only the study of sound propagation, but also the masking of sound signals by interfering phenomenon and signal processing for extracting these signals from interference. This chapter we will present the basics physics of ocean acoustics and then discuss applications.

5.1 Ocean Acoustic Environment	3
5.1.1 Ocean Environment.....	3
5.1.2 Basic Acoustic Propagation Paths ...	4
5.1.3 Geometric Spreading Loss.....	6
5.2 Physical Mechanisms	7
5.2.1 Transducers	7
5.2.2 Volume Attenuation	9
5.2.3 Bottom Loss.....	10
5.2.4 Scattering and Reverberation	11
5.2.5 Ambient Noise	12
5.2.6 Bubbles and Bubbly Media.....	14
5.3 SONAR and the SONAR Equation	17
5.3.1 Detection Threshold and Receiver Operating Characteristics Curves	17

5.3.2 Passive SONAR Equation	18
5.3.3 Active SONAR Equation	19
5.4 Sound Propagation Models	19
5.4.1 The Wave Equation and Boundary Conditions.....	20
5.4.2 Ray Theory	20
5.4.3 Wavenumber Representation or Spectral Solution	21
5.4.4 Normal-Mode Model	21
5.4.5 Parabolic Equation (PE) Model	24
5.4.6 Propagation and Transmission Loss	26
5.4.7 Fourier Synthesis of Frequency-Domain Solutions.....	27
5.5 Quantitative Description of Propagation	29
5.6 SONAR Array Processing	31
5.6.1 Linear Plane-Wave Beam-Forming and Spatio-Temporal Sampling.....	31
5.6.2 Some Beam-Former Properties	33
5.6.3 Adaptive Processing.....	34
5.6.4 Matched Field Processing, Phase Conjugation and Time Reversal	34
5.7 Active SONAR Processing	37
5.7.1 Active SONAR Signal Processing.....	37
5.7.2 Underwater Acoustic Imaging	39
5.7.3 Acoustic Telemetry.....	43
5.7.4 Travel-Time Tomography.....	44
5.8 Acoustics and Marine Animals	47
5.8.1 Fisheries Acoustics.....	47
5.8.2 Marine Mammal Acoustics	50
5.A Appendix: Units	53
References	53

During the two World Wars, both shallow and deep-water acoustics studies were pursued, but during the Cold War, emphasis shifted sharply to deep water. The post-World War II (WWII) history of antisubmarine warfare (ASW) actually started in 1943 with Ewing and Worzel discovering the deep sound channel (DSC) caused by a minimum in the temperature-dependent

sound speed. (Brekhovskikh of the Soviet Union also discovered it independently, but later.) This minimum has been mapped (dotted line in Fig. 5.1), and typically varies from the cold surface at the poles to a depth of about 1300 m at the equator. Since sound refracts toward lower sound speeds, the DSC produces a refraction-generated waveguide (gray lines) contained



2 Part A | Propagation of Sound

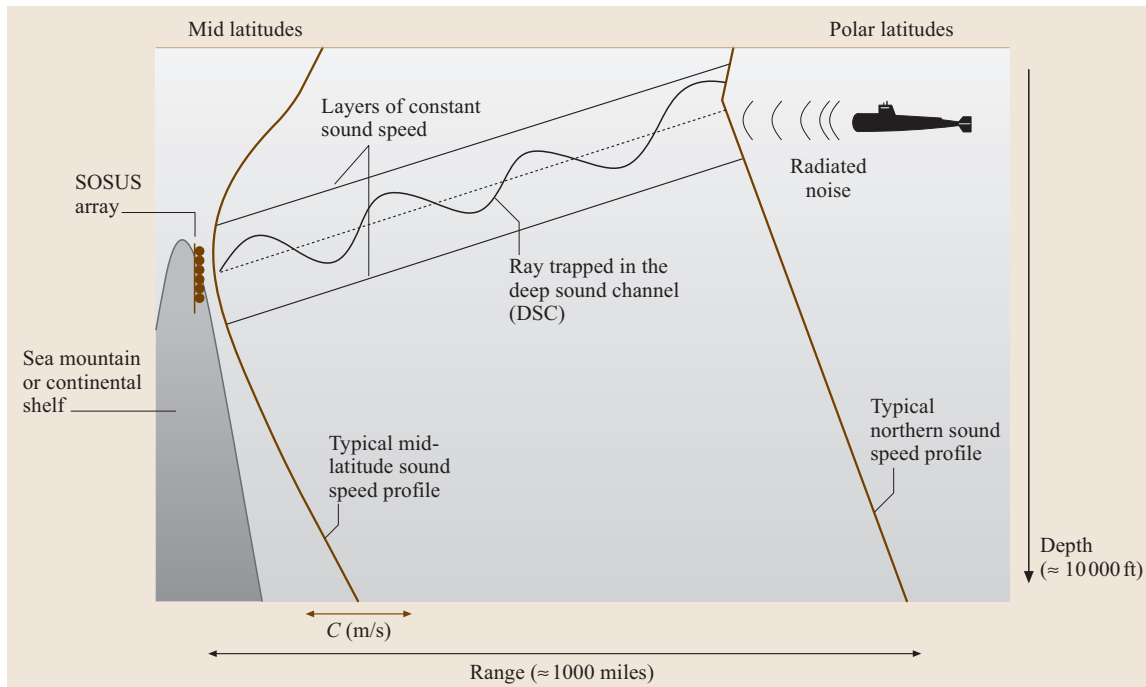


Fig. 5.1 Schematic of a long-range passive detection of a submarine in polar waters by a surveillance system in a temperate region (after [5.1])

within the ocean, such that sound paths oscillate about the sound speed minimum and can propagate thousands of kilometers.

Exploiting the DSC, the US Navy created the multi-billion dollar sound ocean surveillance system (SOSUS) network to monitor Soviet ballistic-missile nuclear submarines. Acoustic antennas were placed on ocean mountains or continental rises whose height extended into the DSC. These antennas were hard-wired to land stations using reliable undersea telephone cable technology. Submarines typically go down to depths of a few hundred meters. With many submarines loitering in polar waters, they were coupling into the DSC at shallower depths. Detections were made on very narrow-band radiation caused by imperfect, rotating machinery such as propellers. The advantage of detecting a set of narrow-band lines is that most of the broadband ocean noise can be filtered out. Though it was a Cold War, the multi-decade success of SOSUS was, in effect, a major Naval victory. The system was compromised by a spy episode, when the nature of the system was revealed. The result was a Soviet submarine quietening program and over the years, the Soviet fleet became quieter, reducing the long-range capabil-

ity of the SOSUS system. The end of the Cold War led to an emphasis on the issue of detecting very quiet diesel-electric submarines in the noisy, shallow water that encompasses about 5% of the World's oceans on the continental shelves, roughly the region from the beach to the shelfbreak at about ≈ 200 m depth. However, there are also signs of a rekindling of interest in deep-water problems.

Parallel to these military developments, the field of ocean acoustics also grew for commercial, environmental and other purposes. Since the ocean environment has a large effect on acoustic propagation and therefore SONAR performance, acoustic methods to map and otherwise study the ocean were developed. As active SONARs were being put forward as a solution for the detection of quiet submarines, there was a growing need to study the effects of sound on marine mammals. Commercially, acoustic methods for fish finding and counting were developed as well as bottom-mapping techniques, the latter being having both commercial and military applications. All in all, ocean acoustics research and development has blossomed in the last half-century and many standard monographs and textbooks are now available ([5.2–10]).



5.1 Ocean Acoustic Environment

The acoustic properties of the ocean, such as the paths along which sound from a localized source travel, are mainly dependent on the ocean sound speed structure, which in turn is dependent on the oceanographic environment. The combination of water column and bottom properties leads to a set of generic sound-propagation paths descriptive of most propagation phenomena in the ocean.

5.1.1 Ocean Environment

Sound speed in the ocean water column is a function of temperature, salinity and ambient pressure. Since the ambient pressure is a function of depth, it is customary to express the sound speed (c) in m/s as an empirical function of temperature (T) in degrees centigrade, salinity (S) in parts per thousand and depth (z) in meters, for example [5.7, 11, 12]

$$c = 1449.2 + 4.6T - 0.055T^2 + 0.00029T^3 + (1.34 - 0.01T)(S - 35) + 0.016z. \quad (5.1)$$

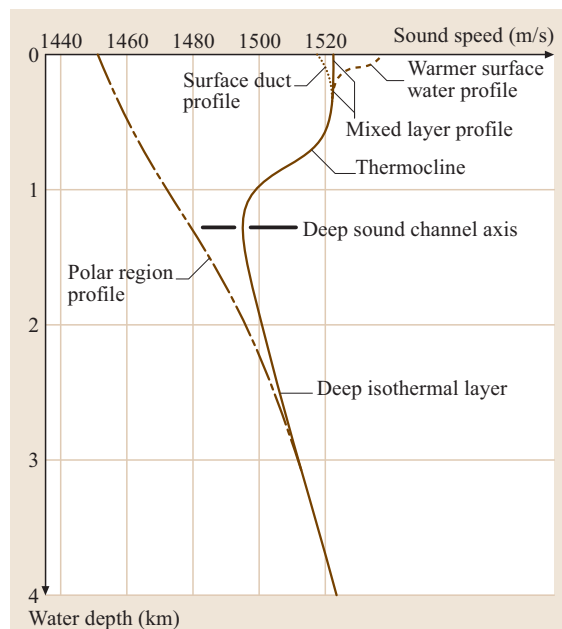


Fig. 5.2 Generic sound-speed profiles. The profiles reflect the tendencies that sound speed varies directly with temperature and hydrostatic pressure. Near-surface mixing can lead to almost isovelocity in that region. In polar waters, the coldest region is at the surface

Figure 5.2 shows a typical set of sound speed profiles indicating the greatest variability near the surface. In a warmer season (or warmer part of the day, sometimes referred to as the *afternoon effect*), the temperature increases near the surface and hence the sound speed increases toward the sea surface. In nonpolar regions where mixing near the surface due to wind and wave activity is important, a *mixed layer* of almost constant temperature is often created. In this isothermal layer the sound speed increases with depth because of the increasing ambient pressure, the last term in (5.1). This is the *surface duct* region. Below the mixed layer is the thermocline where the temperature and hence the sound speed decreases with depth. Below the thermocline, the temperature is constant and the sound speed increases because of increasing ambient pressure. Therefore, between the deep isothermal region and the mixed layer, there is a depth at minimum sound speed referred to as the axis of the *deep sound channel*. However, in polar regions, the water is coldest near the surface so that the minimum sound speed is at the surface. Figure 5.3 is a contour display of the sound speed structure of the North and South Atlantic with the deep sound channel axis indicated by the heavy dashed line. Note that the deep sound channel becomes shallower toward the poles. Aside from sound speed effects, the ocean volume is absorptive and causes attenuation that increases with acoustic frequency.

Shallower water such as that in continental shelf and slope regions is not deep enough for the depth-pressure term in (5.1) to be significant. Thus the winter profile tends to isovelocity, simply because of mixing, whereas the summer profile has a higher sound speed near the surface due to heating; both are schematically represented in Fig. 5.4.

The sound speed structure regulates the interaction of sound with the boundaries. The ocean is bounded above by air, which is a nearly perfect reflector; however, the sea surface is often rough, causing sound to scatter in directions away from the specular reflecting angle. The ocean bottom is typically a complicated, rough, layered structure supporting elastic waves. Its geoacoustic properties are summarized by density, compressional and shear speed, and attenuation profiles. The two basic interfaces, air/sea and sea/bottom, can be thought of as the boundaries of an acoustic waveguide whose internal index of refraction is determined by the

internal gravity wave (IW)
underwater propagation
very short-range paths



4 Part A | Propagation of Sound

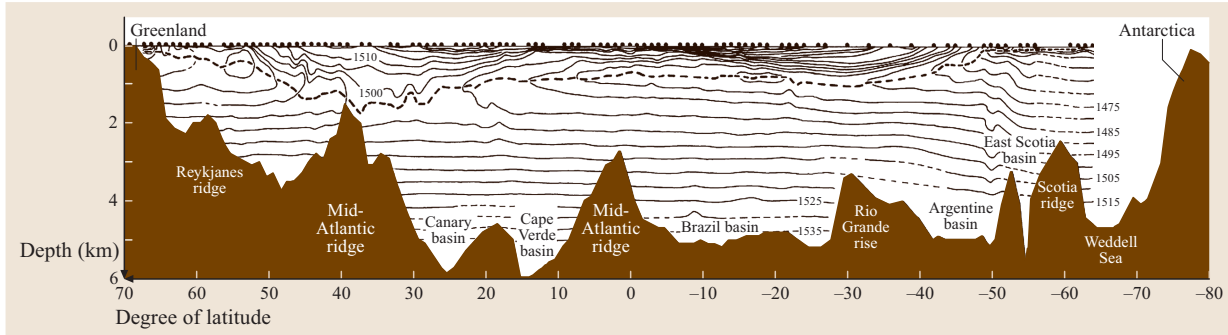


Fig. 5.3 Sound-speed contours at 5 m/s intervals taken from the North and South Atlantic along 30.50° W. The dashed line indicates the axis of the deep sound channel (after [5.13]). The sound channel is deepest near the equator and comes to the surface at the poles

fundamental oceanographic parameters represented in the sound speed equation (5.2).

Due to the density stratification of the water column, the interior of the ocean supports a variety of waves, just as the ocean surface does. One particularly important type of wave in both shallow water and deep water is the internal gravity wave (IW) [5.14]. This wave type is bounded in frequency between the inertial frequency, $f = 2\Omega \sin \theta$, where Ω is the rotation frequency of the earth and θ is the latitude, and the highest buoyancy frequency (or Brunt–Vaisala frequency) $N_{\max}(z)$, where $N^2(z) = -(g/\rho)d\rho/dz$, and $\rho(z)$ is the density of the fluid as a function of depth z . The inertial frequency varies from two cycles per day at the poles to zero cycles per day at the equator, and the maximum buoyancy frequency is usually on the order of 5–10 cycles per hour.

Two categories of IWs are found in stratified coastal waters: linear and nonlinear waves. The linear waves, found virtually everywhere, obey a standard linear wave equation for the displacement of the surfaces of constant density (*isopycnal* surfaces). The nonlinear IWs, which are generated under somewhat more specialized circumstances than the linear waves (and thus are not always present), can obey a family of nonlinear wave equations. The most useful and illustrative of them is the familiar Korteweg–deVries equation (KdV), which governs the horizontal components of the nonlinear internal waves. The vertical component of the nonlinear internal waves obeys a normal-mode equation.

5.1.2 Basic Acoustic Propagation Paths

Sound propagation in the ocean can be qualitatively broken down into three classes: very-short-range, deep-water and shallow-water propagation.

Very-Short-Range Propagation

The pressure amplitude from a point source in free space falls off with range r as r^{-1} ; this geometric loss is called *spherical spreading*. Most sources of interest in the deep ocean are closer to the surface than to the bottom. Hence, the two main short-range paths are the direct path and the surface reflected path. When these two paths *interfere*, they produce a spatial distribution of sound often referred to as a Lloyd mirror pattern, as shown in insert of Fig. 5.5. Also, with reference to Fig. 5.5, note that the *transmission loss* is a decibel measure of the decay with distance of acoustic intensity from a source relative to its value at unit distance (see Appendix), the latter being proportional to the square of the acoustic amplitude.

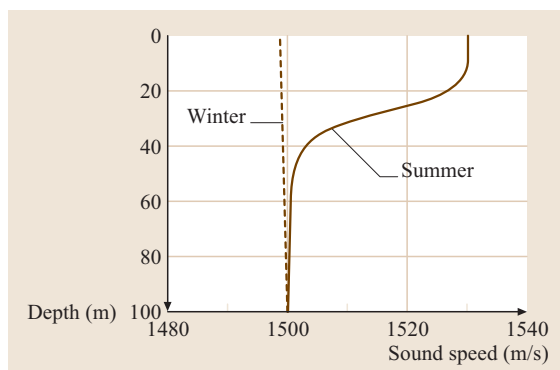


Fig. 5.4 Typical summer and winter shallow-water sound-speed profiles. Warming causes the high-speed region near the surface in the summer. Without strong heating, mixing tends to make the shallow-water region isovelocity in the winter



Long-Range Propagation Paths

Figure 5.6 is a schematic of propagation paths in the ocean resulting from the sound-speed profiles (indicated by the dashed line) described above in Fig. 5.2. These paths can be understood from *Snell's law*,

$$\frac{\cos \theta(z)}{c(z)} = \text{constant}, \quad (5.2)$$

which relates the ray angle $\theta(z)$ with respect to the horizontal, to the local sound speed $c(z)$ at depth z . The equation requires that, the higher the sound speed, the smaller the angle with the horizontal, meaning that sound bends away from regions of high sound speed; or said another way, sound bends toward regions of low sound speed. Therefore, paths 1, 2, and 3 are the simplest to explain since they are paths that oscillate about the local sound speed minima. For example, path 3 depicted by a ray leaving a source near the deep sound channel axis at a small horizontal angle propagates in the deep sound channel. This path, in temperate latitudes where the sound speed minimum is far from the surface, permits propagation over distances of thousands of kilometers.

The upper turning point of this path typically interacts with the thermocline, which is a region of strong internal wave activity. Path 4, which is at slightly steeper angles and is usually excited by a near-surface source, is *convergence zone* propagation, a spatially periodic (35–65 km) refocusing phenomenon producing zones of high intensity near the surface due to the upward refracting nature of the deep sound-speed profile. Regions between these zones are referred to as shadow regions. Referring back to Fig. 5.2, there may be a depth in the deep isothermal layer at which the sound speed is the same as it is at the surface. This depth is called the *critical depth* and is the lower limit of the deep sound channel. If the critical depth is in the water column, the environment supports long-distance propagation without bottom interaction whereas if there is no critical depth in the water column, the ocean bottom is the lower boundary of the deep sound channel. The *bottom bounce* path 5 is also a periodic phenomenon but with a shorter cycle distance and shorter propagation distance because of losses when sound is reflected from the ocean bottom. Finally, note that when bottom bathymetry is described in the general context of the spectral properties of waveguide propagation, they are described in terms of the continuous horizontal wavenumber region as explained in the discussion associated with Fig. 5.32a.

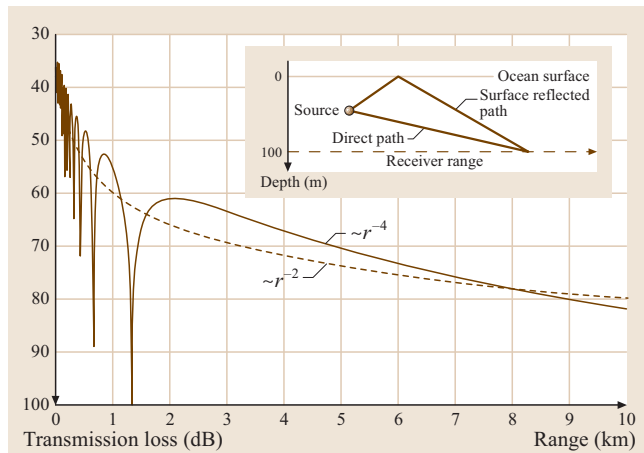


Fig. 5.5 The insert shows the geometry of the Lloyd's mirror effect. The plots show a comparison of Lloyd's mirror (full line) to spherical spreading (dashed line). Transmission losses are plotted in decibels corresponding to losses of $10 \log r^2$ and $10 \log r^4$, respectively, as explained in Sect. 5.1.3

Shallow Water and Waveguide Propagation

In general the ocean can be thought of as an acoustic waveguide [5.1]; this waveguide physics is particularly evident in shallow water (inshore out to the continental slope, typically to depths of a few hundred meters). Snell's law applied to the summer profile in Fig. 5.4 produces rays which bend more toward the bottom than winter profiles in which the rays tend to be straight. This implies two effects with respect to the ocean bottom: (1) for a given range, there are more bounces off

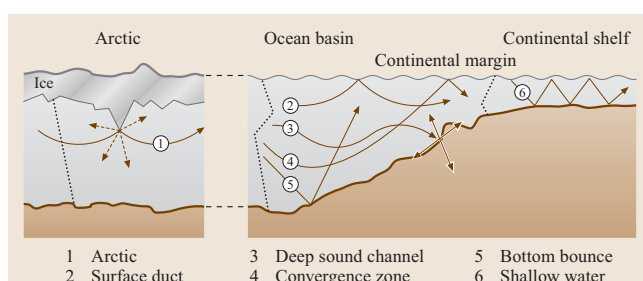


Fig. 5.6 Schematic representation of various types of sound propagation in the ocean. An intuitive guide is that Snell's law has sound turning toward lower-speed regions. That alone explains all the refractive paths: 1, 2, 3 and 4. It will also explain any curvature associated with paths 5 and 6. Thus, the summer profile would have path 6 curving downward (this curvature is not shown in the figure) while the deep sound-speed profile below the minimum curves upward (4)



6 Part A | Propagation of Sound

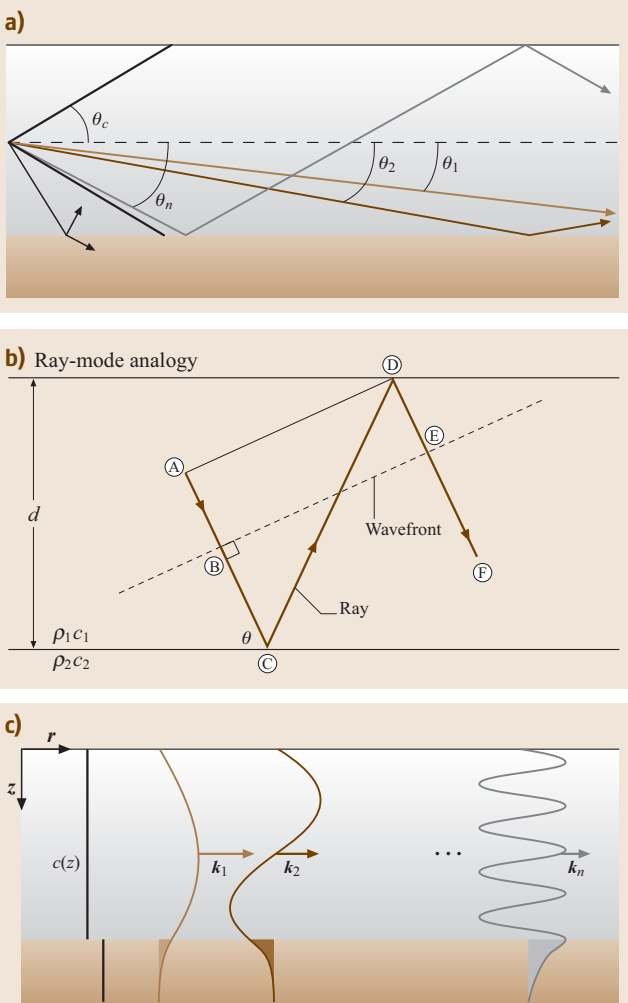


Fig. 5.7a–c Ocean waveguide propagation. (a) Long-distance propagation occurs within the critical angle cone of $2\theta_c$. (b) For the example shown, the condition for constructive interference is that the phase change along BCDE be a multiple of 2π . (c) The constructive interference can be interpreted as discrete modes traveling in the waveguide, each with their own horizontal wavenumber

the ocean bottom in summer than in the winter, and (2) the ray angles intercepting the bottom are steeper in the summer than in the winter. A qualitative understanding of the reflection properties of the ocean bottom should therefore be very revealing of sound propagation in summer versus winter. Basically, near-grazing incidence is much less lossy than larger, more-vertical angles of incidence. Since summer propagation paths have more bounces, each of which are at steeper angles

than winter paths, summer shallow-water propagation is lossier than winter. This result is tempered by rough winter surface conditions that generate large scattering losses at the higher frequencies.

For simplicity we consider an isovelocity waveguide bounded above by the air–water interface and below by a two-fluid interface that is classically defined as a Pekeris waveguide. From Sect. 5.2.3, we have perfect reflection with a 180° phase change at the surface and for grazing angles lower than the bottom critical angle, there will also be perfect bottom reflection. Therefore, as schematically indicated in Fig. 5.7a, ray paths within a cone of $2\theta_c$ will propagate unattenuated down the waveguide. Because the up- and down-going rays have equal amplitudes, preferred angles will exist for which constructive interference occurs. These particular angles are associated with the normal modes of the waveguide, as formally derived from the wave equation in the Sect. 5.4. However, it is instructive to understand the geometric origin of the waveguide modal structure. Figure 5.7b is a schematic of a ray reflected from the bottom and then the surface of a Pekeris waveguide. Consider a ray along the path ACDF and its wavefront, which is perpendicular to the ray. The two down-going rays of equal amplitude, AC and DF, will constructively interfere if points B and E have a phase difference of a multiple of 2π (and similarly for up-going rays). The phase change at the two boundaries must be included. There is a discrete set of angles up to the critical angle for which this constructive interference takes place and, hence, for which sound propagates. This discrete set, in terms of wave physics, are called the normal modes of the waveguide, illustrated in Fig. 5.7c. They correspond to the ray schematic of Fig. 5.7a. Mode propagation is further discussed in the Sect. 5.4.4.

5.1.3 Geometric Spreading Loss

The energy per unit time emitted by a sound source is flowing through a larger area with increasing range. Intensity is the power flux through a unit area, which translates to the energy flow per unit time through a unit area. The simplest example of geometric loss is spherical spreading for a point source in free space where the area increases as r^2 , where r is the range from the point source. So spherical spreading results in an intensity decay proportional to r^{-2} . Since intensity is proportional to the square of the pressure amplitude, the fluctuations in pressure induced by the sound p , decay as r^{-1} . For range-independent ducted propagation, that is, where rays are refracted or reflected back towards the horizon-



tal direction, there is no loss associated with the vertical dimension. In this case, the spreading surface is the area of the cylinder whose axis is in the vertical direction passing through the source $2\pi rH$, where H is the depth of the duct (waveguide), and is constant. Geometric loss in the near-field Lloyd-mirror regime requires consideration of interfering beams from direct and surface

reflected paths. To summarize, the geometric spreading laws for the pressure field (recall that intensity is proportional to the square of the pressure.) are:

- Spherical spreading loss: $p \propto r^{-1}$;
- Cylindrical spreading loss: $p \propto r^{-1/2}$;
- Lloyd-mirror loss: $p \propto r^{-2}$.

5.2 Physical Mechanisms

The physical mechanisms associated with the generation, reception, attenuation and scattering of sound in the ocean are discussed in this section.

5.2.1 Transducers

A transducer converts some sort of energy to sound (source) or converts sound energy (receiver) to an electrical signal [5.15]. In underwater acoustics piezoelectric and magnetostrictive transducers are commonly used; the former connects electric polarization to mechanical strain and the latter connects the magnetization of a ferromagnetic material to mechanical strain. Piezoelectric transducers represent more than 90% of the sound sources used in the ocean. Magnetostrictive transducers are more expensive, have poor efficiency and a narrow frequency bandwidth. However, they allow large vibration amplitudes and are relevant to low-frequency high-power applications. In addition there are: electrodynamic transducers in which sound pressure oscillations move a current-carrying coil through a magnetic field causing a back emf, and electrostatic transducers in which charged electrodes moving in a sound field change the capacitance of the system. Explosives, air guns, electric discharges, and lasers are also used as wide-band sources.

Hydrophones, underwater acoustic receivers, are commonly piezoelectric devices with good sensitivity and low internal noise levels. Hydrophones usually work on large frequency bandwidths since they do not need to be adjusted to a resonant frequency. They are associated with low-level electronics such as preamplifiers and filters.

Because the field of transducers is large by itself, we concentrate in this section on some very practical issues that are immediately necessary to either convert received voltage levels to pressure levels or transmitter excitation to pressure levels. Practical issues about transducers and hydrophones deal with the understanding of specification sheets given by the manufacturer.

Among those, we will describe, based on a practical example, the definition and the use of the following quantities:

- Transmitting voltage response
- Open-circuit receiving response
- Transmitting and receiving beam patterns at specific frequencies
- Impedance and/or admittance versus frequency
- Resonant frequency, maximum voltage and maximum source level (for a transducer).

Figure 5.8 is a specification sheet provided by the ITC (International Transducer Corp.) for a deep-water omnidirectional transducer. Figure 5.8a corresponds to the transmitting sensitivity versus frequency. The units are in dB re $\mu\text{Pa}/\text{V}@1\text{m}$, which means that, at the resonant frequency 11.5 kHz for example, the transducer excited with a 1 V amplitude transmits at one meter a pressure p_t such that $20 \log_{10} \left(\frac{p_t}{1 \times 10^{-6}} \right) = 149 \text{ dB}$, i.e. $p_t \approx 28.2 \text{ Pa}$. Similarly, Fig. 5.8b shows the receiving sensitivity versus frequency. The units are now in dB re $1\text{V}/\mu\text{Pa}$ which means that, at 11.5 kHz for example, the transducer converts a 1 μPa amplitude field into a voltage V_r such that $20 \log_{10} \left(\frac{V_r}{1} \right) = -186 \text{ dB}$, i.e. $V_r \approx 5 \times 10^{-10} \text{ V}$. Figure 5.8c shows the admittance versus frequency. The complex admittance Y is the inverse of the complex impedance Z . The real part of the admittance is called the conductance G ; the imaginary part is the susceptance B . Those curves directly yield the calculation of the electrical impedance of the transducer. For example, the impedance of ITC-1007 at the resonant frequency is $|Z| = 1 / (\sqrt{G^2 + B^2}) \approx 115 \Omega$. When used as a source, the transducer electrical impedance has to match the output impedance of the power amplifier to allow for a good power transfer through the transducer. In the case where the impedances do not match, a customized matching box will be necessary. Knowing the electrical impedance $|Z|$ and the input power $I = 10000 \text{ W}$, the maximum voltage can be determined as $U_{\max} = \sqrt{|Z|I} \approx 1072 \text{ V}$. According to

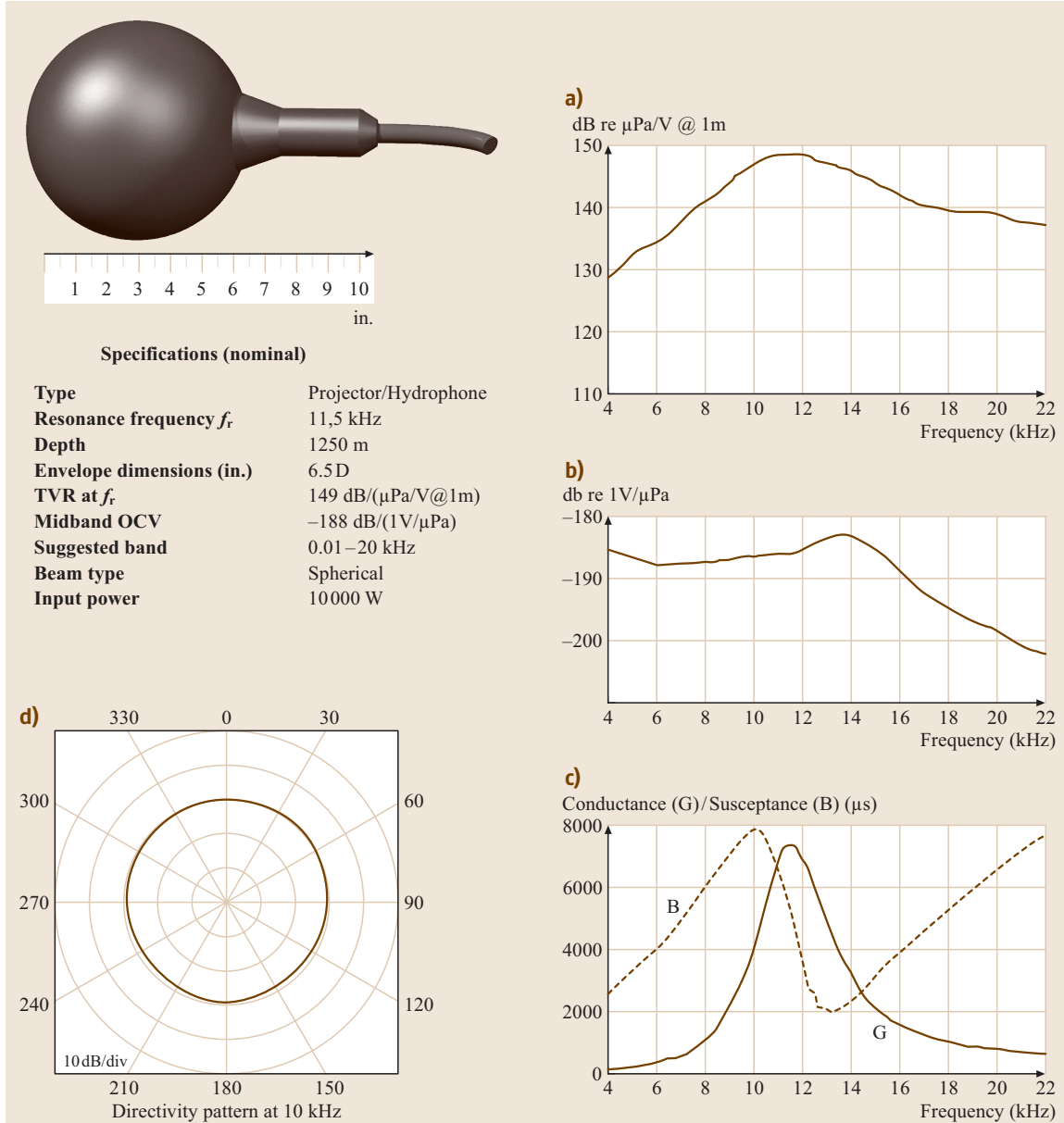


Fig. 5.8a–d Typical specification sheet of a powerful underwater acoustic transponder (top left). (a) Transmitting voltage response. (b) Receiving voltage response. (c) Real (full line) and imaginary part (dashed line) of the water admittance Y . (d) Directionality pattern at one frequency (Courtesy of International Transducer Corp.)

the transmitting voltage response, this corresponds to a source level of nearly 210 dB re μPa at the resonant frequency. Finally, Fig. 5.8d represents the directivity pattern at a given frequency. It shows that the ITC-1007 is omnidirectional at 10 kHz.

When transducers have to be coupled to a power amplifier or another electronic device, it may be useful to model the transducer as an electronic circuit (Fig. 5.9a). The frequency dependence of the conductance G and susceptance B (Fig. 5.8c) yield the components of the



equivalent circuit, as shown in Fig. 5.9b. Similarly, an important parameter is the quality factor Q , which measures the ratio between the mechanical energy transmitted by the transducer and the energy dissipated (Fig. 5.10). Finally, the equivalent circuit leads to the measure of the electroacoustic power efficiency k^2 that corresponds to the ratio of the output acoustic power and the input electric power.

Hydrophones are usually described with the same characteristics as transducers but they are only designed to work in reception. To this goal, hydrophones are usually connected to a preamplifier with high input impedance to avoid any loss in the signal reception. A typical hydrophone exhibits a flat receiving response on a large bandwidth far away from its resonance frequency (Fig. 5.11a). As expected, the sensitivity of a hydrophone is much higher than the sensitivity of a transducer. Low electronic noise below the ocean ambient-noise level is also an important characteristic for hydrophones (Fig. 5.11b). Finally, hydrophones are typically designed to be omnidirectional (Fig. 5.11c).

5.2.2 Volume Attenuation

Attenuation is characterized by an exponential decay of the sound field. If A_0 is the root-mean-square (rms) amplitude of the sound field at unit distance from the source, then the attenuation of the sound field causes the amplitude to decay with distance along the path r

$$A = A_0 \exp(-\alpha r), \quad (5.3)$$

where the unit of α is Nepers/distance. The attenuation coefficient can be expressed in decibels per unit distance by the conversion $\alpha' = 8.686\alpha$. Volume attenuation increases with frequency and the frequency dependence of attenuation can be roughly divided into four regimes as displayed in Fig. 5.12. In region I, leakage out of the sound channel is believed to be the main cause of attenuation. The main mechanisms associated with regions II and III are boric acid and magnesium sulfate chemical relaxation. Region IV is dominated by the shear and bulk viscosity associated with fresh water. A summary of the approximate frequency dependence (f in kHz) of attenuation (in units of dB/km) is given by

$$\begin{aligned} \alpha'(\text{dB/km}) = & 3.3 \times 10^{-3} + \frac{0.11f^2}{1+f^2} \\ & + \frac{43f^2}{4100+f^2} + 2.98 \times 10^{-4} f^2, \end{aligned} \quad (5.4)$$

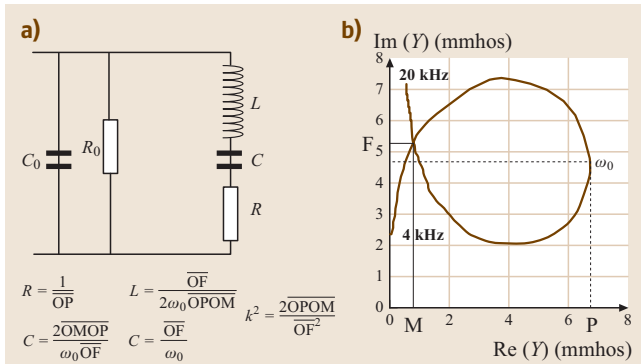


Fig. 5.9 (a) Representation of the transducer as an electronic circuit around the resonant frequency. The resistor R_0 corresponds to the dielectric loss in the transducer and is commonly supposed infinite. C_0 is the transducer capacity, L and C are the mass and rigidity of the material, respectively. R includes both the mechanic loss and the energy mechanically transmitted by the transducer. (b) The values of C_0 , L , C and R are obtained from the positions of the points F , M and P in the real–imaginary admittance curve given in the specification sheet

with the terms sequentially associated with regions I–IV in Fig. 5.12.

In Fig. 5.6, the losses associated with path 3 only include volume attenuation and scattering because this path does not involve boundary interactions. The volume scattering can be biological in origin or arise from interaction with internal wave activity in the vicinity

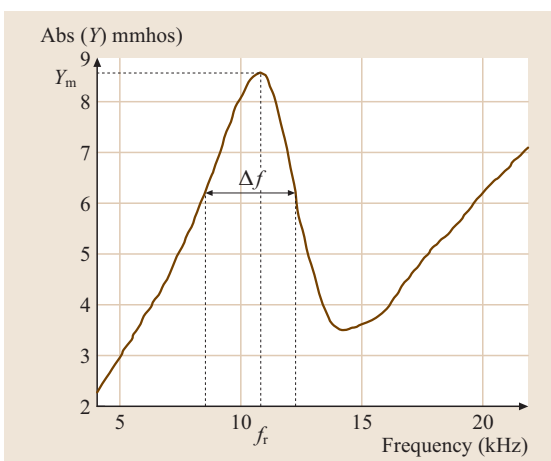


Fig. 5.10 Frequency dependence of the admittance curve that allows the calculation of the quality factor $Q = f_r/\Delta f$ of the transducer at the resonant frequency f_r . Y_m is the maximum of the admittance

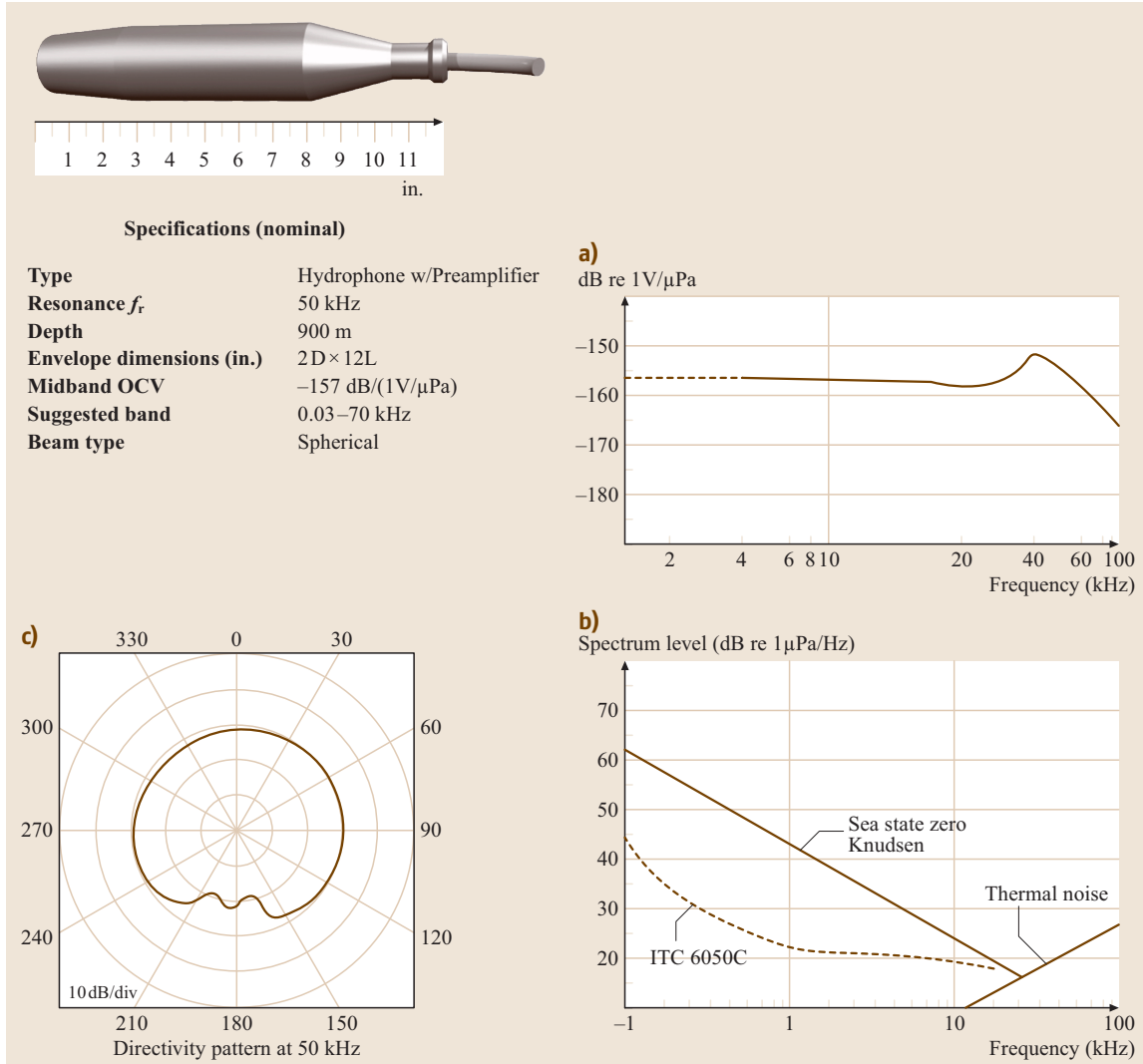


Fig. 5.11a–c Typical specification sheet of a hydrophone (top). (a) Receiving frequency response. (b) Spectral noise level of the hydrophone to be compared to the ocean ambient noise level. (c) Directionality pattern at one frequency (Courtesy of International Transducer Corp.)

of the upper part of the deep sound channel where paths are refracted before they interact with the surface. Both of these effects are small at low frequencies. This same internal wave region is also on the lower boundary of the surface duct, allowing scattering out of the surface duct, thereby also constituting a loss mechanism for the surface duct. This mechanism also leaks sound into the deep sound channel, a region that without scattering would be a shadow zone for a surface duct source. This type of scattering from internal

waves is also a source of fluctuation of the sound field.

5.2.3 Bottom Loss

The structure of the ocean bottom affects those acoustic paths which interact with it. This bottom interaction is summarized by *bottom reflectivity*, the amplitude ratio of reflected and incident plane waves at the ocean–bottom interface as a function of grazing angle, θ

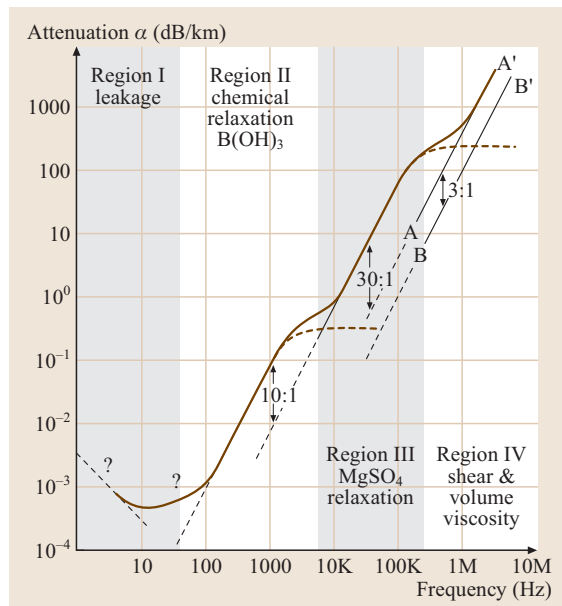


Fig. 5.12 Regions of the different dominant attenuation processes for sound propagating in seawater (after [5.16]). The attenuation is given in dB per kilometer

(Fig. 5.13a). For a simple bottom, which can be represented by a semi-infinite half-space with constant sound speed c_2 and density ρ_2 , the reflectivity is given by

$$R(\theta) = \frac{\rho_2 k_{1z} - \rho_1 k_{2z}}{\rho_2 k_{1z} + \rho_1 k_{2z}}, \quad (5.5)$$

with the subscripts 1 and 2 denoting the water and ocean bottom, respectively; the wavenumbers are given by

$$k_{iz} = (\omega/c_i) \sin \theta_i = k \sin \theta_i; i = 1, 2. \quad (5.6)$$

The incident and transmitted grazing angles are related by Snell's law,

$$c_2 \cos \theta_1 = c_1 \cos \theta_2, \quad (5.7)$$

and the incident grazing angle θ_1 is also equal to the angle of the reflected plane wave.

For this simple water–bottom interface for which we take $c_2 > c_1$, there exists a critical grazing angle θ_c below which there is perfect reflection,

$$\cos \theta_c = \frac{c_1}{c_2}. \quad (5.8)$$

For a lossy bottom, there is no perfect reflection, as also indicated in a typical reflection curve in Fig. 5.13b. These results are approximately frequency indepen-

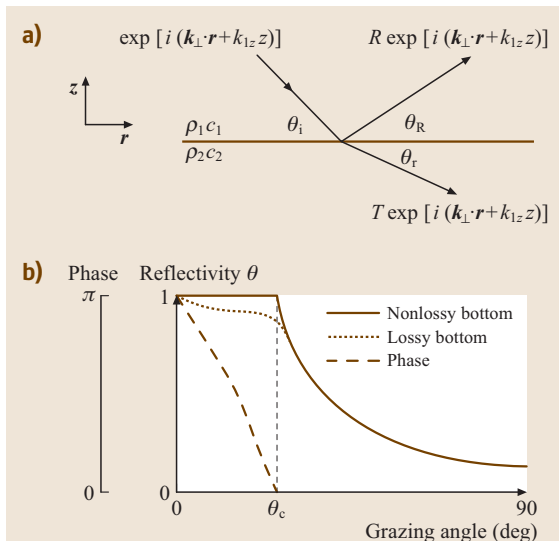


Fig. 5.13a,b The reflection and transmission process. Grazing angles are defined relative to the horizontal.

(a) A plane wave is incident on an interface separating two media with densities and sound speeds ρ , c . $R(\theta)$ and $T(\theta)$ are reflection and transmission coefficients. Snell's law is a statement that k_\perp , the horizontal component of the wave vector, is the same for all three waves. **(b)** Rayleigh reflection curve $R(\theta)$ as a function of the grazing angle indicating critical angle θ_c . The dashed curve shows that, if the second medium is lossy, there is no perfect reflection below the critical angle. Note that for the non-lossy bottom, there is complete reflection below the critical angle, but with a phase change

dent. However, for a layered bottom, the reflectivity has a complicated frequency dependence. It should be pointed out that, if the density of the second medium vanishes, the reflectivity reduces to the pressure release case of $R(\theta) = -1$.

5.2.4 Scattering and Reverberation

Scattering caused by rough boundaries or volume heterogeneities is a mechanism for loss (attenuation), reverberant interference and fluctuation. Attenuation from volume scattering is addressed in Sect. 5.2.2. In most cases, it is the mean or coherent (or specular) part of the acoustic field which is of interest for a SONAR or communications application and scattering causes part of the acoustic field to be randomized. Rough surface scattering out of the *specular direction* can be thought of as an attenuation of the mean acoustic field and typ-



ically increases with increasing frequency. A formula often used to describe reflectivity from a rough boundary is

$$R'(\theta) = R(\theta) \exp\left(-\frac{\Gamma^2}{2}\right), \quad (5.9)$$

where $R(\theta)$ is the reflection coefficient of the smooth interface and Γ is the Rayleigh roughness parameter defined as $\Gamma \equiv 2k\sigma \sin \theta$ where $k = 2\pi/\lambda$, λ is the acoustic wavelength, and σ is the rms roughness height [5.18–20].

The scattered field is often referred to as reverberation. Surface, bottom or volume scattering strength, $S_{S,B,V}$ is a simple parameterization of the production of reverberation and is defined as the ratio in decibels of the sound scattered by a unit surface area or volume referenced to a unit distance I_{scat} to the incident plane wave intensity I_{inc}

$$S_{S,B,V} = 10 \log \frac{I_{\text{scat}}}{I_{\text{inc}}}. \quad (5.10)$$

The Chapman–Harris [5.21] curves predicts the ocean surface scattering strength in the 400–6400 Hz region,

$$S_S = 3.3\beta \log \frac{\theta}{30} - 42.4 \log \beta + 2.6; \\ \beta = 107(wf^{1/3})^{-0.58}, \quad (5.11)$$

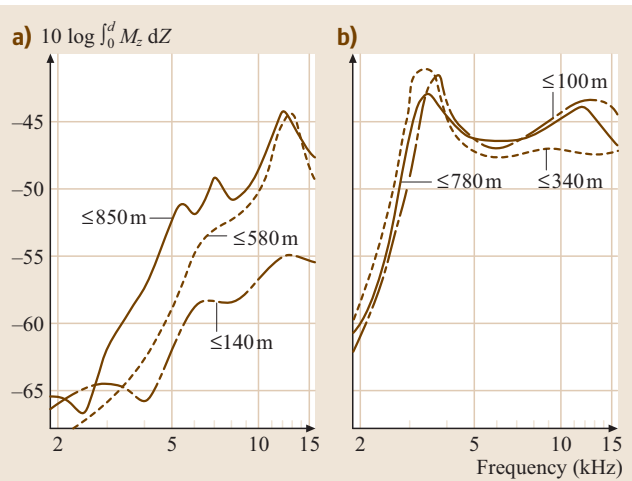


Fig. 5.14 (a) Day and (b) night scattering strength measurements using an explosive source as a function of frequency (after [5.17]). The spectra measured at various times after the explosion are labeled with the depth of the nearest scatterer that could have contributed to the reverberation. The ordinate corresponds to S_V in (5.13)

where θ is the grazing angle in degrees, w the wind speed in m/s and f the frequency in Hz. Ocean surface scattering is further discussed in [5.22].

The simple characterization of bottom backscattering strength utilizes Lambert's rule for diffuse scattering,

$$S_B = A + 10 \log \sin^2 \theta, \quad (5.12)$$

where the first term is determined empirically. Under the assumption that all incident energy is scattered into the water column with no transmission into the bottom, A is -5 dB. Typical realistic values for A [5.23] which have been measured are -17 dB for the large basalt mid-Atlantic ridge cliffs and -27 dB for sediment ponds.

The volume scattering strength is typically reduced to a surface scattering strength by taking S_V as an average volume scattering strength within some layer at a particular depth; then the corresponding surface scattering strength is

$$S_S = S_V + 10 \log H, \quad (5.13)$$

where H is the layer thickness. The column or integrated scattering strength is defined as the case for which H is the total water depth.

Volume scattering usually decreases with depth (about 5 dB per 300 m) with the exception of the deep scattering layer. For frequencies less than 10 kHz, fish with air-filled swim bladders are the main scatterers. Above 20 kHz, zooplankton or smaller animals that feed upon phytoplankton and the associated biological chain are the scatterers. The deep scattering layer (DSL) is deeper in the day than in the night, changing most rapidly during sunset and sunrise. This layer produces a strong scattering increase of 5–15 dB within 100 m of the surface at night and virtually no scattering in the daytime at the surface since it migrates down to hundreds of meters. Since higher pressure compresses the fish swim bladder, the backscattering acoustic resonance (Sect. 5.2.6) tends to be at a higher frequency during the day when the DSL migrates to greater depths. Examples of day and night scattering strengths are shown in Fig. 5.14.

Finally, as explained in Sect. 5.2.6, near-surface bubbles and bubble clouds can be thought of as either volume or surface scattering mechanisms acting in concert with the rough surface. Bubbles have resonances (typically greater than 10 kHz) and at these resonances, scattering is strongly enhanced. Bubble clouds have collective properties; among these properties is that a bubbly mixture, as specified by its void fraction (total bubble gas volume divided by water volume) has a considerable lower sound speed than water.



5.2.5 Ambient Noise

There are essentially two types of ocean acoustic noise: manmade and natural. Generally, shipping is the most important source of manmade noise, though noise from offshore oil rigs is becoming increasingly prevalent. See also Table 5.2 in the Marine Mammal section for specific examples of manmade noise. Typically, natural noise dominates at low frequencies (below 10 Hz) and high frequencies (above a few hundred Hz). Shipping fills in the region between ten and a few hundred Hz and this component is increasing over time [5.25, 26]. A summary of the spectrum of noise is shown in Fig. 5.15. The higher-frequency noise is usually parameterized according to the sea state (also Beaufort number) and/or wind. Table 5.1 summarizes the description of the sea state.

The sound-speed profile affects the vertical and angular distribution of noise in the deep ocean. When

there is a critical depth (Sect. 5.1.2), sound from surface sources travels long distances without interacting with the ocean bottom, but a receiver below this critical depth should sense less surface noise because propagation involves interaction with lossy boundaries, the surface and/or bottom. This is illustrated in Fig. 5.16a,b which shows a deep-water environment with measured ambient noise. Figure 5.16c is an example of vertical directivity of noise which also follows the propagation physics discussed above. The shallower depth is at the axis of the deep sound channel while the other is at the critical depth. The pattern is narrower at the critical depth where the sound paths tend to be horizontal since the rays are turning around at the lower boundary of the deep sound channel.

In a range-independent ocean, Snell's law predicts a horizontal noise notch at depths where the speed of sound is less than the near-surface sound speed. Returning to (5.2) and reading off the sound speeds

Table 5.1 Descriptor of the ocean sea surface (after [5.24])

Sea criteria	Beau-fort scale	Wind speed range knots (m/s)	mean knots (m/s)	12 h wind Wave height ^{a,b} ft (m)	Fully arisen sea Wave height ^{a,b} ft (m)	Duration ^{b,c} h	Fetch ^{b,c} naut. miles (km)	Sea-state scale
Mirror-like	0	< 1 (< 0.5)						0
Ripples	1	1–3 (0.5–1.7)	2 (1.1)					0.5
Small wavelets	2	4–6 (1.8–3.3)	5 (2.5)	< 1 (< 0.30)	< 1 (< 0.30)			1
Large wavelets, scattered whitecaps	3	7–10 (3.4–5.4)	8.5 (4.4)	1–2 (0.30–0.61)	1–2 (0.30–0.61)	< 2.5	< 10 (< 19)	2
Small waves, frequent whitecaps	4	11–16 (5.5–8.4)	13.5 (6.9)	2–5 (0.61–1.5)	2–6 (0.61–1.8)	2.5–6.5	10–40 (19–74)	3
Moderate waves, many whitecaps	5	17–21 (8.5–11.1)	19 (9.8)	5–8 (1.5–2.4)	6–10 (1.8–3.0)	6.5–11	40–100 (74–185)	4
Large waves, whitecaps everywhere, spray	6	22–27 (11.2–14.1)	24.5 (12.6)	8–12 (2.4–3.7)	10–17 (3.0–5.2)	11–18	100–200 (185–370)	5
Heaped-up sea, blown spray, streaks	7	28–33 (14.2–17.2)	30.5 (15.7)	12–17 (3.7–5.2)	17–26 (5.2–7.9)	18–29	200–400 (370–740)	6
Moderately high, long waves, spindrift	8	34–40 (17.3–20.8)	37 (19.0)	17–24 (5.2–7.3)	26–39 (7.9–11.9)	29–42	400–700 (740–1300)	7

Notes:

a The average height of the highest one-third of the waves (significant wave height)

b Estimated from data given in US Navy Hydrographic Office (Washington, D.C.) publications HO 604 (1951) and HO 603 (1955)

c The minimum fetch and duration of the wind needed to generate a fully arisen sea



14 Part A | Propagation of Sound

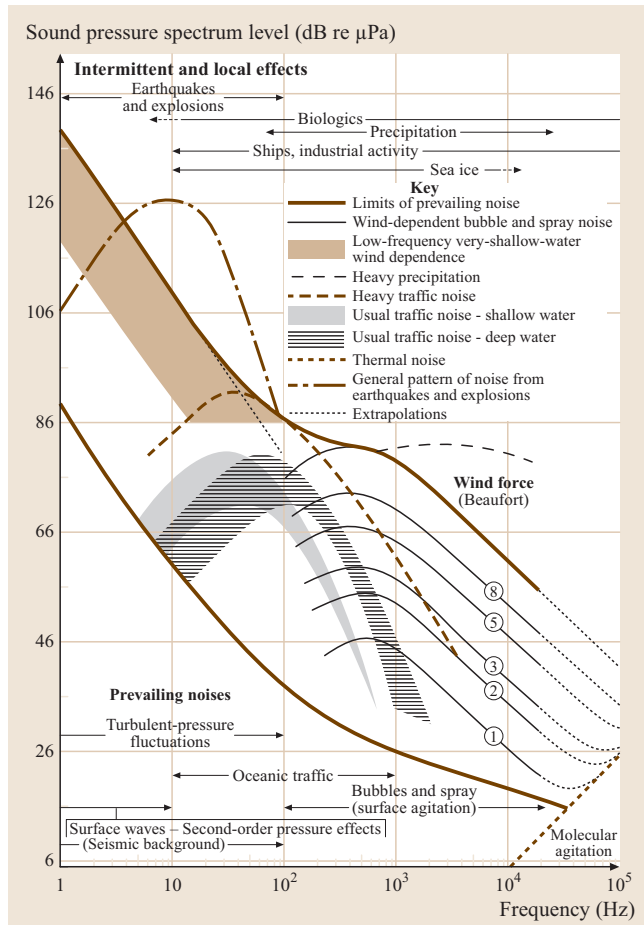


Fig. 5.15 Composite of ambient noise spectra (after [5.24])

from Fig. 5.16 at the surface ($c = 1530 \text{ m/s}$) and say, 300 m (1500 m/s), a horizontal ray ($\theta = 0$) launched from the ocean surface would have an angle with respect to the horizontal of about 11° at 300 m depth. All other rays would arrive with greater vertical angles. Hence we expect this horizontal notch. However, the horizontal notch is often not seen at shipping noise frequencies. That is because shipping tends to be concentrated in continental-shelf regions and propagation down a continental slope converts high-angle rays to lower angles at each bounce. There are also deep-sound-channel shoaling effects that result in the same trend in angle conversion.

The vertical directionality of noise in shallow water has a simple environmental dependence [5.27]. For example, in the summer with a downward refracting profile, the same discussion as above leads to a horizon-

tal noise notch. However the vertical directionality of noise from the surface in the winter tends to be driven by bottom properties. Thus, if the bottom is not very lossy, surface sources exciting low-order modes can come from large distances (and hence large areas). These paths are close to the horizontal and noise will then tend to have a strong horizontal component. On the other hand, a very lossy bottom will prevent long-range propagating paths from contributing to the noise field and the noise will tend to be local and subsequently vertical.

5.2.6 Bubbles and Bubbly Media

Bubbles not only occur naturally in the ocean, but the swim bladders of fish can also be thought of as bubbles. The physics of bubbles is a large area of activity in acoustics [5.7, 28]. Here we will confine ourselves to some aspects relevant to ocean acoustics. First we discuss some properties of bubbles in terms of resonators, scatterers and then go on to some aspects of bubbly media and scattering from bubbles.

Bubble scattering follows two regimes depending on the magnitude of the bubble radius oscillations in response to the incident fluctuating pressure field [5.29]:

1. For small pressure amplitudes, the response is linear. The first step in any linear analysis is the identification of the resonance frequency of an oscillating bubble and the measurement of the bubble scattering cross section.
2. Due to nonlinear terms in the governing equations, the response of a bubble will be affected by nonlinearities as the amplitude of the pressure field is increased. In this case, the bubble may continue to oscillate stably (stable acoustic cavitation) generating (sub)harmonics in the scattered field. Under other circumstances, the change in bubble size during a single cycle of oscillation becomes so large that the bubble undergoes a cycle of explosive cavitation growth and violent collapse. Such a response is termed *transient acoustic cavitation* and is distinguished from stable acoustic cavitation by the fact that the bubble radius changes by several orders of magnitude during each cycle.

The Bubble as a Scattering

The calculation of the natural acoustic resonance of an oscillating bubble in the linear regime requires considerable algebra combining: (1) the equation of motion, (2) mass conservation, and (3) continuity relations at the bubble surface. These developments go beyond the



scope of this chapter. In the following, we simply summarize the final results, which are the expression of the bubble natural acoustic resonance ω_0^2 , and the expression for the scattered field from an acoustic bubble under an incident pressure field at frequency ω .

The acoustic resonance in the linear regime of a single bubble of radius a is

$$\omega_0^2 = \left[\frac{3\gamma p_0}{\rho_w a^2} + (3\gamma - 1) \frac{2T}{\rho_w a^3} \right], \quad (5.14)$$

where p_0 is the ambient pressure outside the bubble, T is surface tension (tensile force/length in units N/m), ρ_w is the density of water and γ is the ratio of specific heats. Neglecting surface tension in (5.14) for bubble sizes larger than 1 μm and considering the acoustic expansion/compression process to be adiabatic ($c_{\text{air}}^2 = \gamma p_0 / \rho_{\text{air}}$), we obtain the approximate expression

$$\omega_0 = \frac{1}{a} \sqrt{\frac{3c_{\text{air}}^2 \rho_{\text{air}}}{\rho_w}}, \quad (5.15)$$

and for $c_{\text{air}} \approx 340 \text{ m/s}$, we get $f_0 \approx \frac{3}{a}$ with a in m and f_0 in Hz.

We now consider an incident plane wave at frequency ω in the regime $ka = \omega a/c = 2\pi a/\lambda \ll 1$. The far-field expression for the spatial part of the radiated acoustic field p_r is

$$p_r(r) = -\frac{a}{r} p_i \exp\left[-\frac{i\omega}{c}(r-a)\right] \times \left[1 - \frac{\omega_0^2}{\omega^2} \left(1 - \frac{i\omega a}{c}\right)\right]^{-1}. \quad (5.16)$$

First, we note that in the high-frequency limit, we recover $p_r(r, t) = -\frac{a}{r} p_i (t - \frac{r-a}{c})$ that was given by the boundary conditions at the bubble surface.

To understand the effect of the resonance frequency, consider two cases. The first case is $\omega \gg \omega_0$ for which we obtain

$$p_r(r) = -\frac{a}{r} p_i e^{-\frac{i\omega}{c}(r-a)}, \quad (5.17)$$

whereas for the case $\omega = \omega_0$ we get

$$p_r(r) = -\frac{ic}{\omega r} p_i e^{-\frac{i\omega}{c}(r-a)} = -\frac{i\lambda}{2\pi r} p_i e^{-\frac{i\omega}{c}(r-a)}. \quad (5.18)$$

Comparing the two equations, (5.18) appears to be the field radiating from a sphere of radius $\lambda/2\pi$ which is much larger than a . For example, neglecting surface tension, at 1 atm, $\omega_0 a \approx 20$ so that $\lambda \approx 500a$. This resonance effect is also quite apparent when considering the scattering cross section of the bubble.

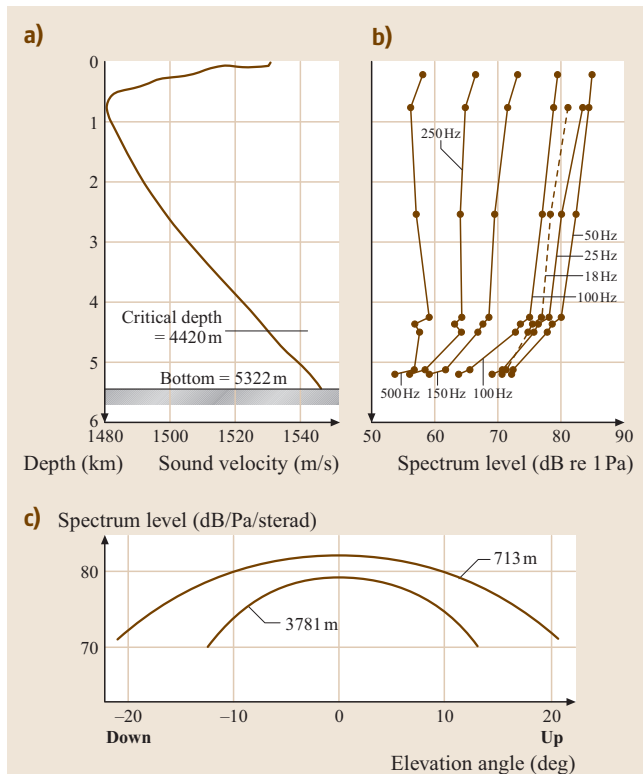


Fig. 5.16a–c Noise in the deep ocean. (a) Sound-speed profile and (b) noise level as a function of depth in the Pacific (after [5.30]). (c) The vertical directivity of noise at the axis of the deep sound channel and at the critical depth in the Pacific (after [5.31])

The scattering cross section σ_s is the ratio of the total scattered power (intensity \times area = pressure \times velocity \times enclosing area) to the incident plane-wave intensity (given by $p_i^2/2\rho_w c$, with the factor of 1/2 coming from averaging over a cycle) and therefore has the units of area. We perform this calculation in the far field using (5.16) to obtain

$$\sigma_s = \frac{4\pi a^2}{\left[1 - \frac{\omega_0^2}{\omega^2} \left(1 - \frac{i\omega a}{c}\right)\right]^2} \xrightarrow{\omega=\omega_0} \frac{\lambda^2}{\pi}, \quad (5.19)$$

which is consistent with a surface area associated with the discussion below (5.18). The resonance makes the bubble appear larger in surface area than its dimension. On the other hand, for the case $\omega \ll \omega_0$, we have

$$\sigma_s = 4\pi a^2 \left(\frac{\omega}{\omega_0}\right)^4, \quad (5.20)$$

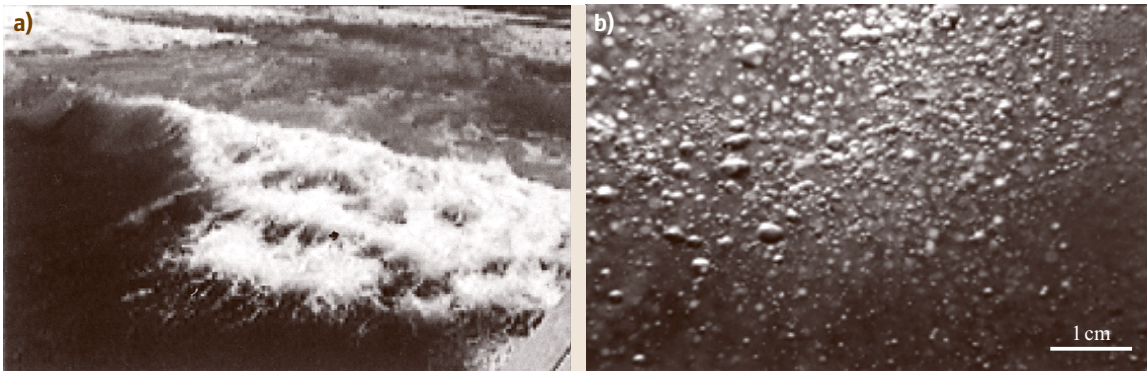


Fig. 5.17 (a) Wave breaking on the shore; (b) magnified view of individual bubbles within the plumes taken a second or so after wave breaking. The void fraction of air in these plumes is a few percent and bubbles range in size from less than 50 µm to a few mm radius. Bubble plumes found beneath breaking waves in 15–20 m/s winds in the open ocean have a similar size distribution (Courtesy of Grant Deane, Scripps Institution of Oceanography)

which is Rayleigh scattering. The analogous mechanism in electromagnetics explains why the sky is blue: blue has a higher frequency than red so it is scattered more. The above derivations only included radiation damping and we have not included lossy effects caused by thermal conductivity and shear viscosity. Looking at, for example (5.16), we can think of the radiation damping constant to be $\delta_r = ka$ or, in other words, at resonance $\sigma_s = 4\pi a^2/\delta_r^2$. Finally, we mention that the extinction cross section is the sum of the scattering cross section and the absorption cross section. The damping coefficients for thermal conductivity and shear viscosity are typically experimentally determined.

Bubbly Media

The region immediately below the surface of the ocean is a bubbly medium (Fig. 5.17). The existence of bubbles changes the effective compressibility of the water. We define a volume fraction of bubble (also called the void fraction) μ so that the density of the mixture is simply $\rho_m = \mu\rho_b + (1 - \mu)\rho_w$ where the subscripts b and w refer to a bubble and water, respectively. We consider low frequencies with respect to resonance and we use the compressibility, the inverse of the bulk modulus $B = \rho(\delta p/\delta\rho)$, since it is additive and permits us to write down the compressibility of the mixture,

$$\begin{aligned} K_m &= \mu K_b + (1 - \mu) K_w \rightarrow \frac{1}{B_m} \\ &= \mu \frac{1}{B_b} + (1 - \mu) \frac{1}{B_w}. \end{aligned} \quad (5.21)$$

Using the above discussion relating sound speed and the adiabatic bulk modulus for the air bubble with $\gamma = 1.4$ (the bulk modulus of water is 2.3×10^9 Pa) we then obtain:

$$\begin{aligned} \frac{1}{\rho_m c_m^2} &= \frac{\mu}{1.4 p_b} + \frac{(1 - \mu)}{\rho_w c_w^2} \rightarrow c_m^2 \\ &= \left(\frac{1.4 p_b}{\mu \rho_w c_w^2 + 1.4 p_b(1 - \mu)} \right) c_w^2, \end{aligned} \quad (5.22)$$

where we have taken $\rho_m \approx \rho_w$. Substituting some typical numbers, we use atmospheric pressure, $p_b \approx 10^5$ Pa, $\rho_w \approx 10^3$ kg/m³, $c_w = 1500$ m/s and we consider two void fractions: μ of 0.0001 and 0.001 (large). The corresponding sound speeds in the bubbly mixture are about 930 m/s and 370 m/s, respectively. A small amount of bubbles significantly changes the compressibility of the medium and therefore drastically changes the sound speeds. In reality, the speed of sound through the bubbly medium varies with frequency since compressibility is the ratio of the fractional change in volume to the incident pressure. The volume change is related to the bubble surface displacement and hence to velocity or radiated pressure as per (5.16). Therefore, the bubble compressibility is actually frequency dependent and a more rigorous treatment of propagation in bubbly media would show the dispersion of the speed through the bubbly medium.

When sound propagates through a bubbly medium, the scattering will also cause attenuation due to scattering and absorption. As stated above, the extinction cross section, σ_e , is a measure of this phenomenon. For

detection threshold (DT)
 PD (probability of detection)
 probability of detection (PD)
 PFA (probability of false alarm)
 probability density function (PDF)
 PDF (probability density function)
 SONAR

Index entries on this page

a bubbly medium (and for the simple case of single-sized bubbles), an acoustic beam will be altered by the absorption and scattering out of the beam. For an incident plane wave of intensity I_0 , the power removed by each bubble is $I_0\sigma_e$ so that the rate of change of intensity as the beam travels through a bubble medium of N

bubbles per unit volume is

$$\frac{dI}{dx} = -I_0\sigma_e N \rightarrow I = I_0 \exp(-\sigma_e Nx). \quad (5.23)$$

Therefore, a bubbly medium changes the sound speed, absorbs sound, and is dispersive.

5.3 SONAR and the SONAR Equation

A major application of underwater acoustics is SONAR system technology. The performance of SONAR is often approximately described by the SONAR equation. The methodology of the SONAR equation is analogous to an accounting procedure involving acoustic signal, interference and system characteristics. Figure 5.18 provides a schematic of passive and active SONARS.

5.3.1 Detection Threshold and Receiver Operating Characteristics Curves

The detection threshold (DT) [5.16] is a decibel number that essentially incorporates the SONAR system's (which includes the operator) ability to decide that a detection is made or not made. The detection process includes the following probabilities:

- the probability of detection (PD): the probability that a signal is detected if it is present;
- 1-PD: the probability the signal will not be detected if it is present;
- the probability of false alarm (PFA): the probability that a signal is detected when it is not present;
- 1-PFA: the probability that the signal will not be detected when it is not present.

In practical terms, since the signal and noise are fluctuating, the detection is made (over a time interval) when the fluctuating sum of the signal and noise exceeds a threshold that is determined from empirically derived probability density functions (PDFs) of noise and signal plus noise. For example, the case that the noise alone rises above the threshold contributes to the PFA. Therefore, the process for determining a detection threshold level will depend on the PD and PFA. Typically numbers might be a PD of 0.5 and PFA of 0.0001. The probabilities will themselves be a function of the relation between the signal and noise statistics, as represented by their mean and variance. The detection index d succinctly characterizes this relation in that it

indicates how easy it is to observe a signal in noise,

$$d = \frac{(M_{sn} - M_n)^2}{\sigma_n^2}, \quad (5.24)$$

where M_{sn} is the mean of the signal plus noise, M_n is the noise mean and σ_n^2 is the noise variance. Figure 5.19 shows schematically the implications of the detection index where the relative proximity of the two probability density functions (PDFs) determine the detection

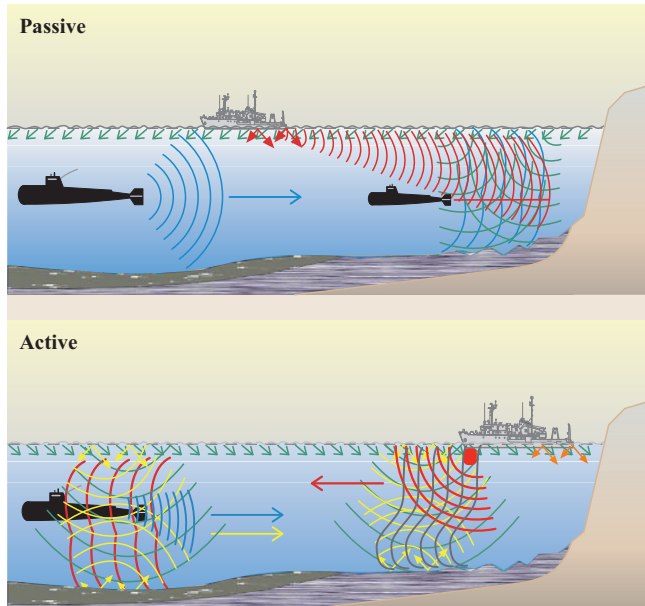


Fig. 5.18 Passive and active SONAR for submarine detection. *Passive*: the submarine on the right tries to detect sounds (blue) from the other submarine using a towed array (antenna). These sounds are distorted by the shallow-water environment and are embedded in ocean surface noise (green) and surface shipping noise (red). *Active*: the ship on the right sends out a pulse (red) and an echo (blue), distorted by the shallow-water environment, is returned to the ship SONAR which tries to distinguish it from backscattered reverberation (yellow) and ocean noise (green) (after [5.1])

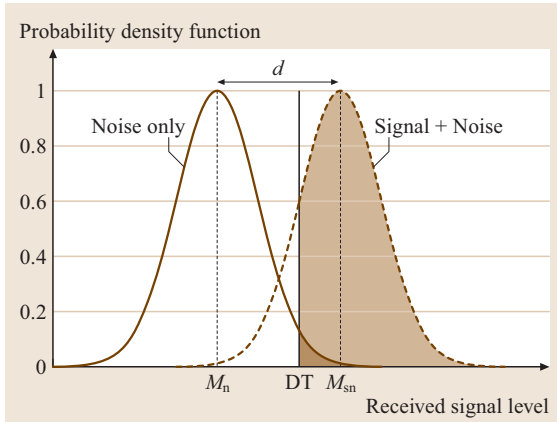


Fig. 5.19 Probability density functions (PDF) of noise and signal+noise. Various probabilities as explained in the text are related to specific regions under the curves. Thus, the probability of detection (PD) is the *light-shaded area* under the signal+noise PDF curve that is to the right of DT, the detection threshold (*thick vertical line*). Similarly, the probability of false alarm is the *dark shaded area* under the noise PDF curve that is to the right of DT

statistics. We first note that the PD is the area under the signal-plus-noise curve to the right of the DT and the PFA is the area under the noise curve to the right of the DT. Then, for example, if the mean of the signal-plus-noise PDF was further to the right (higher signal-to-noise ratio (SNR)), the detection index and PD would be larger.

We could then move the DT to the right, changing the PD, but the PFA would be smaller. Receiver operating characteristics (ROC) curves are plots of PD versus PFA parameterized by d (Fig. 5.19). Figure 5.20 gives a typical example of using this methodology and refer the reader to the SONAR literature [5.16] for a more complete treatment. A square-law detector is commonly used for a passive system dealing with unknown signal. In that case, it has been shown that the detection index for a small-SNR, narrow-band signal in Gaussian noise is given by

$$d = \omega t \left(\frac{S}{N} \right)^2, \quad (5.25)$$

where ω , t , S and N are the bandwidth (taken to be larger than the width of the spectral line of the signal), integration time, signal power and noise power in the bandwidth, respectively. If 1 Hz is the noise bandwidth reference, the detection index is $d = \omega t (S/N_0)$, where N_0 is the noise in a 1 Hz band. This gives a relation between the signal-to-noise ratio at the output of an en-

ergy detector of a narrow-band signal in Gaussian noise to the detection index

$$\text{SNR} = 5 \log \left(\frac{d}{\omega t} \right) \equiv \text{DT}, \quad (5.26)$$

where the equivalence symbol is for a detection criteria of a specified PD, PFA.

In reality, there are correction factors for the detection threshold related to the length of observations used to make a decision, human factors, and others that we omit from this discussion. Since the criteria are specified through the ROC curves, we can now estimate the DT for specific cases. We simply go to the the ROC curves for a selected PD versus PFA and read off the detection index, from which we can compute the detection threshold. For example, from Fig. 5.20, for a PD of 50% and a PFA of 0.01%, the detection index is $d = 16$. Using unit bandwidth and integration time, the detection threshold is $\text{DT} = 5 \log 16 = 6 \text{ dB}$. This methodology is an example of the meaning of the DT term in the SONAR equation below, though the relationship between DT and d is different depending on the type of receiver and SONAR.

5.3.2 Passive SONAR Equation

A passive SONAR system uses the radiated sound from a target to detect and locate the target. A radiating object of source level (SL) (all units are in decibels) is received at a hydrophone of a SONAR system at a lower signal level S because of the transmission loss (TL) it suffers (e.g., cylindrical spreading plus attenuation or a TL computed from one of the propagation models of Sect. 5.4),

$$S = SL - TL. \quad (5.27)$$

The noise, N at a single hydrophone is subtracted from (5.27) to obtain the signal-to-noise ratio at a single hydrophone,

$$\text{SNR} = SL - TL - N. \quad (5.28)$$

Typically a SONAR system consists of an array or antenna of hydrophones which provides signal-to-noise enhancement through a beam-forming process (Sect. 5.6). This process is quantified in decibels by the array gain (AG) (see Sect. 5.6.2) that is added to the single-hydrophone SNR to give the SNR at the output of the beam-former,

$$\text{SNR}_{\text{BF}} = SL - TL - N + AG. \quad (5.29)$$



As discussed, because detection involves additional factors including SONAR operator ability, it is necessary to specify a detection threshold, DT level above the SNR_{BF} at which there is a 50% (by convention) probability of detection. The difference between these two quantities is called the signal excess (SE),

$$SE = SL - TL - N + AG - DT. \quad (5.30)$$

This decibel bookkeeping leads to an important SONAR engineering descriptor called the figure of merit (FOM) which is the transmission loss that gives a zero signal excess,

$$FOM = SL - N + AG - DT. \quad (5.31)$$

The FOM encompasses the various parameters a SONAR engineer must deal with: expected source level, the noise environment, array gain and the detection threshold. Conversely since the FOM is a transmission loss, one can use the output of a propagation model (or if appropriate, a simple geometric loss plus attenuation) to estimate the minimum range at which a 50% probability of detection can be expected. This range changes with oceanographic conditions and is often referred to as the range of the day in navy SONAR applications. Finally, we mention that formal detection theory involves a criterion involving the probability of detection PD versus probability of false alarm PFA. Plots of PD versus PFA as parameterized by, say SNR, are called receiver operating characteristic (ROC) curves [5.16]. Clearly, for a PFA of 1, the probability of detection goes to unity.

5.3.3 Active SONAR Equation

A monostatic active SONAR transmits a pulse to a target and its echo is detected at a receiver co-located with the transmitter. A bistatic active SONAR has the receiver in a different location than the transmitter. The main differences between the passive and active cases are the addition of a target strength (TS) term; reverberation (reverberation level, RL) is usually the dominant source of interference, as opposed to noise; and the transmission loss is over two paths: transmitter to target and target

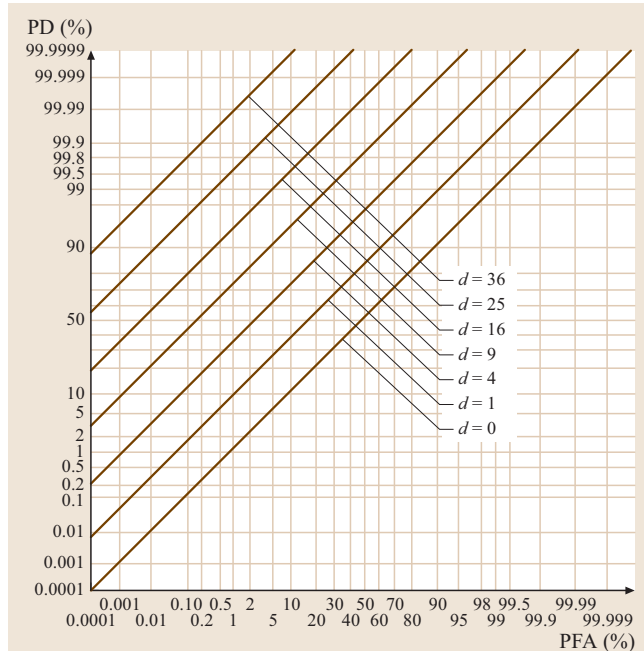


Fig. 5.20 Example of ROC curves. For a given signal plus noise, different threshold settings correspond to different PD and PFA. The ROC curves summarize the relation between PD and PFA for different thresholds as parameterized through the detection index (after [5.16])

to receiver. In the monostatic case, the transmission loss is $2TL$, where TL is the one-way transmission loss, and in the bistatic case, the transmission loss is the sum (in dB) over paths from the transmitter to the target and the target to the receiver, $TL_1 + TL_2$. The concept of the detection threshold is useful for both passive and active SONARs. Hence, for signal excess, we have

$$SE = SL - TL_1 + TS - TL_2 - (RL + N) + AG - DT. \quad (5.32)$$

The corresponding FOM for an active system is defined for the maximum allowable two-way transmission loss with $TS = 0$ dB.

5.4 Sound Propagation Models

The wave equation describing sound propagation is derived from the equations of hydrodynamics and its coefficients and boundary conditions are descriptive of the

ocean environment. There are essentially four types of models (computer solutions to the wave equation [5.4]) to describe sound propagation in the sea: ray theory,



the spectral method or fast field program (FFP), normal mode (NM) and parabolic equation (PE). All of these models allow for the fact that the ocean environment varies with depth. A model that also takes into account horizontal variations in the environment (i.e., sloping bottom or spatially variable oceanography) is termed range-dependent. For high frequencies (a few kilohertz or above), ray theory is the most practical. The other three model types are more applicable and useable at lower frequencies (below 1 kHz). Between these frequencies, one can choose either, noting that the wave solution is the most accurate and should probably be used in all cases where the calculation is still feasible and/or practical. The models discussed here are essentially two-dimensional models since the index of refraction has much stronger dependence on depth than on horizontal distance. Nevertheless, bottom topography and strong ocean features can cause horizontal refraction (out of the range-depth plane). Ray models are most easily extendable to include this added complexity. Full three-dimensional wave models are extremely computationally intensive. A compromise that often works for weakly three-dimensional problems is the $N \times 2D$ approximation that combines two-dimensional solutions along radials to produce a three-dimensional solution.

5.4.1 The Wave Equation and Boundary Conditions

The wave equation for the pressure p in cylindrical coordinates with the range coordinates denoted by $\mathbf{r} = (x, y)$ and the depth coordinate denoted by z (taken positive downward) for a source-free region is

$$\nabla^2 p(\mathbf{r}, z, t) - \frac{1}{c^2(\mathbf{r}, z)} \frac{\partial^2 p(\mathbf{r}, z, t)}{\partial t^2} = 0, \quad (5.33)$$

where $c(\mathbf{r}, z)$ is the sound speed in the wave-propagating medium.

It is convenient to solve (5.33) in the frequency domain by assuming a solution with a frequency dependence of $\exp(-i\omega t)$ to obtain the Helmholtz equation ($K \equiv \omega/c$),

$$\nabla^2 p(\mathbf{r}, z) + K^2 p(\mathbf{r}, z) = 0 \quad (5.34)$$

with

$$K^2(\mathbf{r}, z) = \frac{\omega^2}{c^2(\mathbf{r}, z)}. \quad (5.35)$$

The range-dependent environment manifests itself as the coefficient $K^2(\mathbf{r}, z)$ of the partial differential equation for the appropriate sound speed profile. The

range-dependent bottom type and topography appears as boundary conditions. In underwater acoustics both fluid and elastic (shear-supporting sediments and bottom strata) media are of interest. For simplicity we only consider fluid media below. This is most often a good approximation to describing the bottom near the bottom interface since the material typically has a low shear speed which can be inserted into the fluid equation solution by a perturbation procedure [5.32].

The most common plane-interface boundary conditions encountered in underwater acoustics are the pressure release condition at the ocean surface,

$$p = 0, \quad (5.36)$$

and at the ocean-bottom interface, continuity of pressure

$$p_1 = p_2, \quad (5.37)$$

and vertical particle velocity

$$\frac{1}{\rho_1} \frac{\partial p_1}{\partial z} = \frac{1}{\rho_2} \frac{\partial p_2}{\partial z}, \quad (5.38)$$

where the ρ_i are the densities of the two media. These latter boundary conditions applied to the plane-wave fields in Fig. 5.13a yield the Rayleigh reflection coefficient given by (5.5).

The Helmholtz equation for an acoustic field from a point source is

$$\nabla^2 G(\mathbf{r}, z) + K^2(\mathbf{r}, z)G(\mathbf{r}, z) = -\delta^2(\mathbf{r} - \mathbf{r}_s)\delta(z - z_s), \quad (5.39)$$

where the subscript ‘s’ denotes the source coordinates. The acoustic field from a point source, $G(\mathbf{r})$ is either obtained by solving the boundary-value problem of (5.39) (spectral method or normal modes) or by approximating (5.39) using an initial-value problem (ray theory, parabolic equation).

5.4.2 Ray Theory

Ray theory is a geometrical, high-frequency approximate solution to (5.39) of the form

$$G(\mathbf{R}) = A(\mathbf{R}) \exp[iS(\mathbf{R})], \quad (5.40)$$

where the exponential term allows for rapid variations as a function of range and $A(\mathbf{R})$ is a more slowly varying *envelope* that incorporates both geometrical spreading and loss mechanisms. The geometrical approximation is that the amplitude varies slowly with range (i.e., $(1/A)\nabla^2 A \ll K^2$) so that (5.34) yields the

fast field program (FFP)
FFP (fast field program)
fast Fourier transform (FFT)
FFT (fast Fourier transform)
underwater propagation
normal-mode model



eikonal equation

$$(\nabla S)^2 = K^2. \quad (5.41)$$

The ray trajectories are perpendicular to surfaces of constant phase (wavefronts), S , and may be expressed mathematically as follows

$$\frac{d}{dl} \left(K \frac{d\mathbf{R}}{dl} \right) = \nabla K, \quad (5.42)$$

where l is the arc length along the direction of the ray and \mathbf{R} is the displacement vector to a point on the ray. The direction of average flux (energy) follows that of the trajectories and the amplitude of the field at any point can be obtained from the density of rays.

The ray theory method is computationally rapid and extends to range-dependent problems. Furthermore, the ray traces give a physical picture of the acoustic paths. It is helpful in describing how sound redistributes itself when propagating long distances over paths that include shallow and deep environments and/or mid-latitude to polar regions. The disadvantage of conventional ray theory is that it does not include diffraction, including effects that describe the low-frequency dependence (degree of trapping) of ducted propagation.

5.4.3 Wavenumber Representation or Spectral Solution

The wave equation can be solved efficiently with spectral methods when the ocean environment does not vary with range. The term fast field program (FFP) had been used because the spectral methods became practical with the advent of the fast Fourier transform (FFT). Assume a solution of (5.39) of the form

$$G(\mathbf{r}, z) = \frac{1}{2\pi} \int_{-\infty}^{\infty} d^2k g(\mathbf{k}, z, z_s) \exp[i\mathbf{k} \cdot (\mathbf{r} - \mathbf{r}_s)], \quad (5.43)$$

which then leads to the equation for the depth-dependent Green's function $g(\mathbf{k}, z, z_s)$,

$$\frac{d^2g}{dz^2} + [K^2(z) - k^2] g = -\frac{1}{2\pi} \delta(z - z_s). \quad (5.44)$$

Furthermore, we assume azimuthal symmetry, $kr > 2\pi$ and $\mathbf{r}_s = 0$ so that (5.43) reduces to

$$G(r, z) = \frac{\exp(-i\pi/4)}{(2\pi r)^{1/2}} \times \int_{-\infty}^{+\infty} dk k^{1/2} g(k, z, z_s) \exp(ikr). \quad (5.45)$$

This integral is then evaluated using the fast Fourier transform algorithm. Although the method was initially labeled *fast field* it is fairly slow because of the time required to calculate the Green's functions (solve (5.44)). However, it has advantages when one wishes to calculate the near-field region or to include shear-wave effects in elastic media; it is also often used as a benchmark for other less exact techniques. With a great deal of additional computational effort, this method is extendable to range-dependent environments.

5.4.4 Normal-Mode Model

Rather than solve (5.44) for each g for the complete set of k_s (typically thousands of times), one can utilize a normal-mode expansion of the form

$$g(\mathbf{k}, z) = \sum a_n(\mathbf{k}) u_n(z), \quad (5.46)$$

where the quantities u_n are eigenfunctions of the following eigenvalue problem

$$\frac{d^2 u_n}{dz^2} + [K^2(z) - k_n^2] u_n(z) = 0. \quad (5.47)$$

The eigenfunctions u_n are zero at $z = 0$, satisfy the local boundary conditions descriptive of the ocean bottom properties and satisfy a radiation condition for $z \rightarrow \infty$. For pressure, they form an orthonormal set in a Hilbert space with weighting function $\rho^{-1}(z)$, the local density. The range of discrete eigenvalues corresponding to the poles in the integrand of (5.45) is given by the condition

$$\min[K(z)] < k_n < \max[K(z)]. \quad (5.48)$$

These discrete eigenvalues correspond to discrete angles within the critical angle cone in Fig. 5.7a as discussed in Sect. 5.1.2. The eigenvalues k_n typically have a small imaginary part α_n , which serves as the modal attenuation representative of all the losses in the ocean environment. Solving (5.39) using the normal-mode expansion given by (5.46) yields (for the source at the origin).

$$G(r, z) = \frac{i}{4\rho(z_s)} \sum_n u_n(z_s) u_n(z) H_0^1(k_n r). \quad (5.49)$$

The asymptotic form of the Hankel function can be used in the above equation to obtain the well-known normal-mode representation of a waveguide in cylindrical coordinates

$$G(r, z) = \frac{i}{(8\pi r)^{1/2} \rho(z_s)} \exp(-i\pi/4) \times \sum_n \frac{u_n(z_s) u_n(z)}{k_n^{1/2}} \exp(ik_n r). \quad (5.50)$$



Equation (5.50) is a far-field solution of the wave equation and neglects the continuous spectrum of modes ($k_n < \min[K(z)]$) of (5.48)). For the purposes of illustrating the various portions of the acoustic field, we note that k_n is a horizontal wavenumber so that a ray angle associated with a mode with respect to the horizontal can be taken to be $\theta = \cos^{-1}[k_n/K(z)]$. For a simple waveguide the maximum sound speed is the bottom sound speed corresponding to $\min[K(z)]$. At this value of $K(z)$, we have from Snell's law $\theta = \theta_c$, the bottom critical angle. In effect, if we look at a ray picture of the modes, the continuous portion of the mode spectrum corresponds to rays with grazing angles greater than the bottom critical angle of Fig. 5.13b and therefore outside the cone of Fig. 5.7a. This portion undergoes severe loss. Hence, we note that the continuous spectrum is the near (vertical) field and the discrete spectrum is the far (more-horizontal, profile-dependent) field falling within the cone in Fig. 5.7a.

The advantages of the normal-mode procedure are that: the solution is available for all source and receiver configurations once the eigenvalue problem is solved; it is easily extended in moderately range-dependent conditions using the adiabatic approximation; it can be applied (with more effort) to extremely range-dependent environments using coupled-mode theory. However, it does not include a full representation of the near field.

Adiabatic Mode Theory

All of the range-independent normal-mode calculation method developed for environmental ocean acoustic modeling applications can be adapted to mildly range-dependent conditions using adiabatic mode theory. The underlying assumption is that individual propagating normal modes adapt to the local environment, but do not scatter or couple into each other. The coefficients of the mode expansion, a_n in (5.46), now become mild functions of range, i. e., $a_n(\mathbf{k}) \rightarrow a_n(\mathbf{k}, \mathbf{r})$. This modifies (5.45) as follows

$$G(\mathbf{r}, z) = \frac{i\rho(z_s)}{(8\pi r)^{1/2}} \exp(-i\pi/4) \times \sum_n \frac{u_n(z_s)v_n(z)}{k_n^{1/2}} \exp(ik_n r), \quad (5.51)$$

where the range-averaged wavenumber (eigenvalue) is

$$\bar{k}_n = \frac{1}{r} \int_0^r k_n(r') dr', \quad (5.52)$$

and the $k_n(r')$ are obtained at each range segment from the eigenvalue problem (5.47) evaluated for the envi-

ronment at that particular range along the path. The quantities u_n and v_n are the sets of modes at the source and the field positions, respectively.

Simply stated, the adiabatic mode theory leads to a description of sound propagation such that the acoustic field is a function of the modal structure at both the source and the receiver and some average propagation conditions between the two. Thus, for example, when sound emanates from a shallow region where only two discrete modes exist and propagates into a deeper region with the same bottom (same critical angle), the two modes from the shallow region adapt to the form of the first two modes in the deep region. However, the deep region can support many more modes; intuitively, we therefore expect the resulting two modes in the deep region will take up a smaller, more-horizontal part of the cone of Fig. 5.7a than they take up in the shallow region. This means that sound rays going from shallow to deep regions tend to become more horizontal, which is consistent with a ray picture of down-slope propagation. Finally, fully coupled mode theory for range-dependent environments has been developed but requires intensive computation.

Mode Dispersion in a Waveguide

Acoustical propagation in simple free space is nondispersive. That is, all plane waves travel with speeds independent of frequency. Further, their group and phase speeds are the same as the medium sound speed. However, geometric dispersion is a property of waveguide propagation.

We consider a shallow-water waveguide of the Pekeris type, i. e., a homogeneous water column overlying a homogeneous and denser fluid bottom. A waveguide of this type supports modal propagation, where each mode is characterized by a depth-dependent modal amplitude $u_n(z)$ and a horizontally projected propagating wavenumber k_n . Each mode is characterized by a group velocity v_{gn} and a phase velocity v_{pn} , which are related through the formula

$$\frac{1}{v_{gn}} = v_{pn} \int_0^\infty \frac{u_n^2(z)}{\rho(z) c^2(z)} dz. \quad (5.53)$$

In the case of a perfect waveguide with a constant sound speed c and no penetration in the bottom, (5.53) takes the simplest form $v_{gn} v_{pn} = c^2$. The difference in group velocities between modes results in modal dispersion in a waveguide (Fig. 5.21).

In shallow water, lower-order modes usually travel faster than higher-order modes (Figs. 5.22 and 5.23).



In deep water, where the deep sound channel behaves as a waveguide, the fastest modes are the higher-order modes (Fig. 5.24), a property of refraction-dominated modal propagation. Since modal wavenumbers k_n are frequency dependent, the modes can be plotted in a frequency-wavenumber space that is the Fourier transform of the time-range representation of the dispersed field in Fig. 5.25. As already seen in Fig. 5.21, Fig. 5.26 shows that modes have a cut-off frequency and that there exist a finite number of propagating modes at a given frequency.

Dispersion and The Waveguide Invariant [5.3]

There is actually a fairly robust parameter, the waveguide invariant, that describes dispersion over a (sometimes large) interval of a group of modes. The waveguide invariant β has two important interpretations; first, it is related the local change in the modal group velocity with respect to the change in phase velocity,

$$\frac{1}{\beta} = -\frac{\partial S_g}{\partial S_p}, \quad (5.54)$$

where S_g and S_p and group and phase slowness, where slowness is the inverse of speed.

It turns out that β often has a rather robust value for certain circumstances. For example, it is unity for many shallow-water situations that are dominated by bottom reflection; on the other hand it is negative for refraction-dominated propagation.

Figure 5.27 shows a calculation for a Pacific deep-water case. Note from the definition that β is negative up to a phase speed of about 1540; this region is one of refraction such as deep sound channel and convergence zone propagation. Beyond 1540, β is positive; this is the bottom bounce region dominated by reflections rather than refraction.

The invariant also relates the change in range in the locations of the interference peaks of a transmission loss curve to a change in frequency

$$\frac{\Delta r}{r} = \frac{1}{\beta} \frac{\Delta \omega}{\omega}. \quad (5.55)$$

In Fig. 5.28, we show a set of TL curves for different frequencies; the interference peaks are shifted according to the invariant formula. Another way of representing this shift is through the striations, where TL is the third dimension of a frequency-range plot as shown in Fig. 5.29, which was derived from shallow-water transmission loss data. If one represents range as the product of the velocity of the radiator and time, then, the range axis can be replaced by time and one has

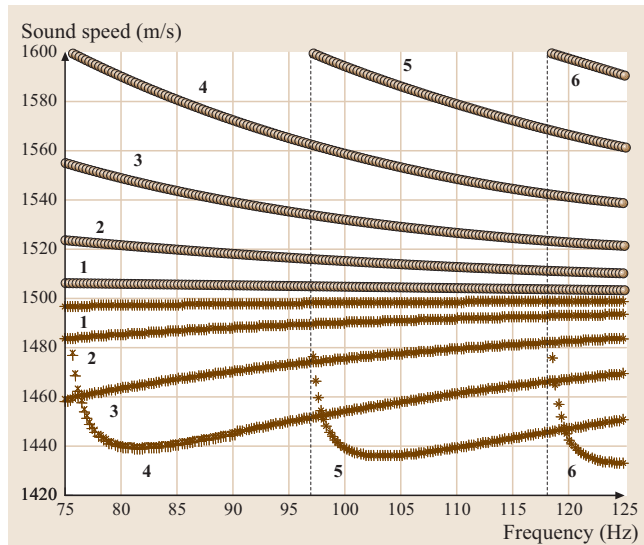


Fig. 5.21 Frequency dependence of the group speed (lower curves 1–6) and phase speed (upper curves 1–6) of modes 1–6 in a Pekeris waveguide with a 100 m water depth, a bottom sound speed c_b and density of 1600 m/s and 1800 kg/m³. Sound speed in water c_ω is constant and equal to 1500 m/s. The bold vertical lines show the cut-off frequencies of modes 4–6, respectively

a frequency-time plot, often called a spectrogram. The TL curve is a slice through the spectrogram for a given frequency and time converted to the appropriate range.

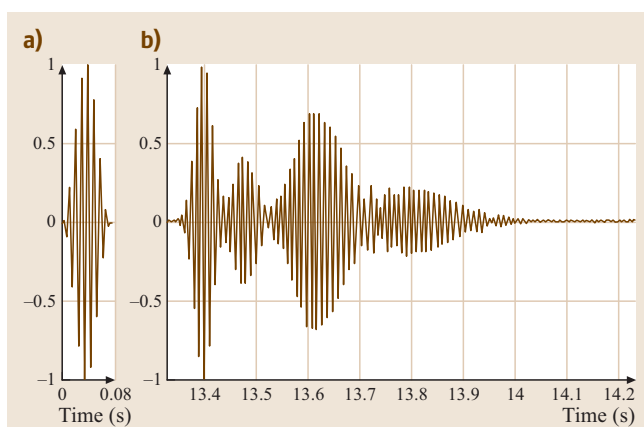


Fig. 5.22a,b Acoustic dispersion in a shallow water waveguide. The right panel (a) corresponds to the waveguide response at $R = 20$ km to the emitted signal (central frequency = 100 Hz, 50 Hz bandwidth) displayed in the left panel. (b) Source depth is at 40 m and the receiver depth at 60 m. Waveguide parameters are the same as in Fig. 5.21

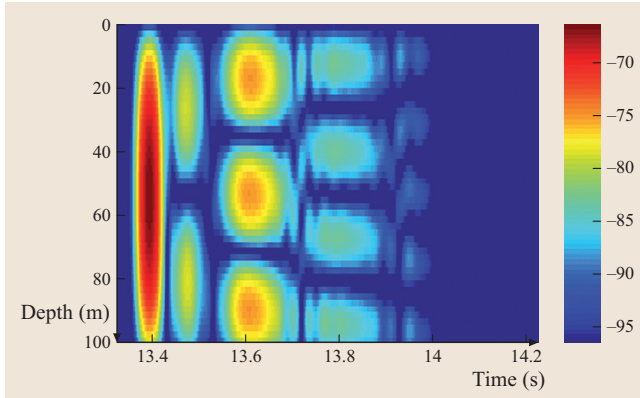


Fig. 5.23 Depth-versus-time representation of the field intensity after a $R = 20$ km propagation in a shallow-water waveguide. The waveguide characteristics are the same as in Fig. 5.21. Source depth is 40 m. The color scale is in dB with a 0 dB source level amplitude at the source

Doppler Shift in a Waveguide

The theory of Doppler shifts involving either a moving source and/or receiver is well known in acoustics, particularly in free space. However, in a waveguide, even if we limit ourselves to horizontal motion, the results are slightly more complex. The individual paths associated with modal propagation, as per Fig. 5.7a, all have finite and different angles with respect to the horizontal. Thus, each mode has a different Doppler shift. The waveguide

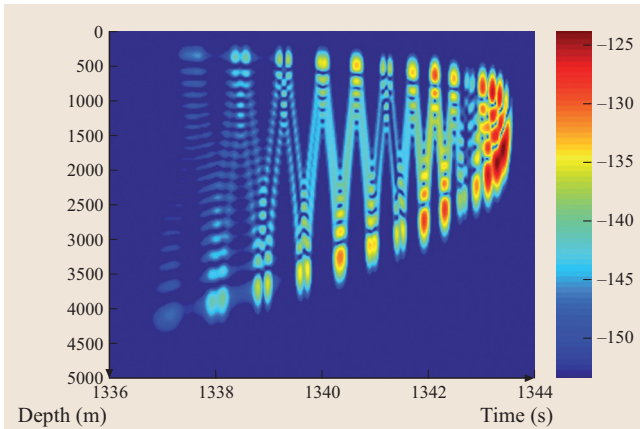


Fig. 5.24 Depth-versus-time representation of the field intensity after a $R = 2000$ km propagation in a deep-water waveguide. We used the Munk profile as a depth-dependent sound-speed profile. Source depth is 900 m, source frequency is 22.5 Hz with a 15 Hz bandwidth. The color scale is in dB with a 0 dB source level amplitude at the source

theory for both source and/or receiver has been worked out (see [5.33], in which there is also a review of the pertinent literature). We return to (5.50) for a harmonic source of angular frequency ω , which therefore results in an additional, identical (when there is no motion) factor for each term of $e^{-i\omega t}$ in the time domain. We now consider a source with a frequency spectrum $S(\omega)$. For constant, horizontal velocities, the normal-mode field results in the *receiver reference frame* are still valid

$$\psi(\mathbf{r}_0 + \mathbf{v}_r t, z, \omega) = \frac{i}{4\rho(z_s)} \times \sum_n S(\Omega_n) u_n(z_s) u_n(z) H_0^1(k_n r), \quad (5.56)$$

but with Doppler shifted modal wavenumbers

$$k_n \rightarrow k_n \left(1 + \frac{v_r}{v_g n} \cos \theta_r \right), \quad (5.57)$$

and Doppler-shifted frequencies (now for each modal term in the summation) of

$$\Omega_n = \omega - k_n (v_s \cos \theta_s - v_r \cos \theta_r), \quad (5.58)$$

where v_{gn} is the group velocity of the n -th mode, $v_s \cos \theta_s$ is the radial speed of the source, and $v_r \cos \theta_r$ is the radial speed of the receiver. Here, radial refers to the projection of the velocities onto the horizontal line between the source and receiver. Note that this latter expression, when multiplied through by the wavenumber, shows that the frequency shift is proportional to the ratio of speeds to the modal phase speed, as opposed to the wavenumber shift which involves the group speed.

5.4.5 Parabolic Equation (PE) Model

The PE method was introduced into ocean acoustics and made viable with the development of the *Tappert split-step algorithm*, which utilized fast Fourier transforms at each range step [5.6]. Subsequent numerical developments greatly expanded the applicability and accuracy of the parabolic equation method.

Standard PE Split-Step Algorithm

The PE method is presently the most practical and all-encompassing wave-theoretic range-dependent propagation model. In its simplest form, it is a far-field narrow-angle ($\approx \pm 20^\circ$) with respect to the horizontal – adequate for many underwater propagation problems – approximations to the wave equation. Assuming azimuthal symmetry about a source, we express the



solution of (5.34) in cylindrical coordinates in a source-free region in the form

$$p(r, z) = \psi(r, z)H(r), \quad (5.59)$$

and we define $K^2(r, z) \equiv K_0^2 n^2$, n therefore being an *index of refraction* c_0/c , where c_0 is a reference sound speed. Substituting (5.59) into (5.34) and taking K_0^2 as the separation constant we end up with a Bessel equation for H that has a Hankel function as the outgoing solution. If we use the asymptotic form of the Hankel function, $H_0^1(K_0 r)$, and invoke the *paraxial* (narrow-angle) approximation,

$$\frac{\partial^2 \psi}{\partial r^2} \ll 2K_0 \frac{\partial \psi}{\partial r}, \quad (5.60)$$

we obtain the parabolic equation (in r),

$$\frac{\partial^2 \psi}{\partial z^2} + 2iK_0 \frac{\partial \psi}{\partial r} + K_0^2(n^2 - 1)\psi = 0, \quad (5.61)$$

where we note that n is a function of range and depth. We use a marching solution to solve the parabolic equation. There has been an assortment of numerical solutions but the one that still remains a standard is the so-called *split-step* range-marching algorithm,

$$\begin{aligned} \psi(r + \Delta r, z) &= \exp\left[\frac{iK_0}{2}(n^2 - 1)\Delta r\right] F^{-1} \\ &\times \left\{ \left[\exp\left(-\frac{i\Delta r}{2K_0}s^2\right) \right] F[\psi(r, z)] \right\}. \end{aligned} \quad (5.62)$$

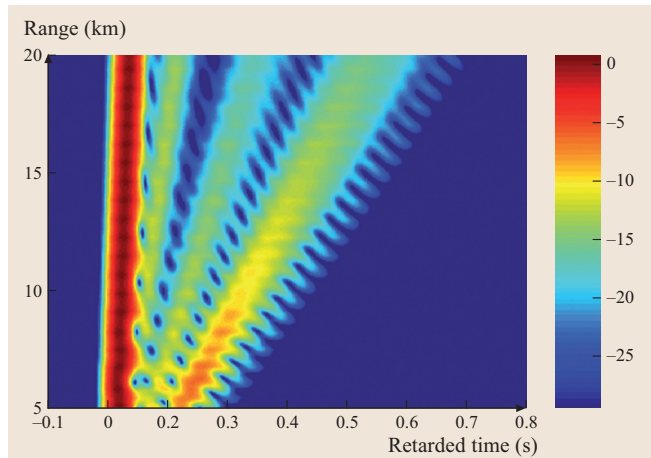


Fig. 5.25 Range-versus-time representation of the field intensity for the same waveguide and source-receiver depth as in Fig. 5.21. The figure clearly shows that modes travel at different speed. The retarded time t is $t - R/c_\omega$. The color scale is in dB with a 0dB reference at range 5 km

The Fourier transforms F , are performed using FFTs. Equation (5.62) is the solution for n constant, but the error introduced when n (profile or bathymetry) varies with range and depth can be made arbitrarily small by increasing the transform size and decreasing the range-step size. It is possible to modify the split-step algorithm to increase its accuracy with respect to higher-angle propagation.

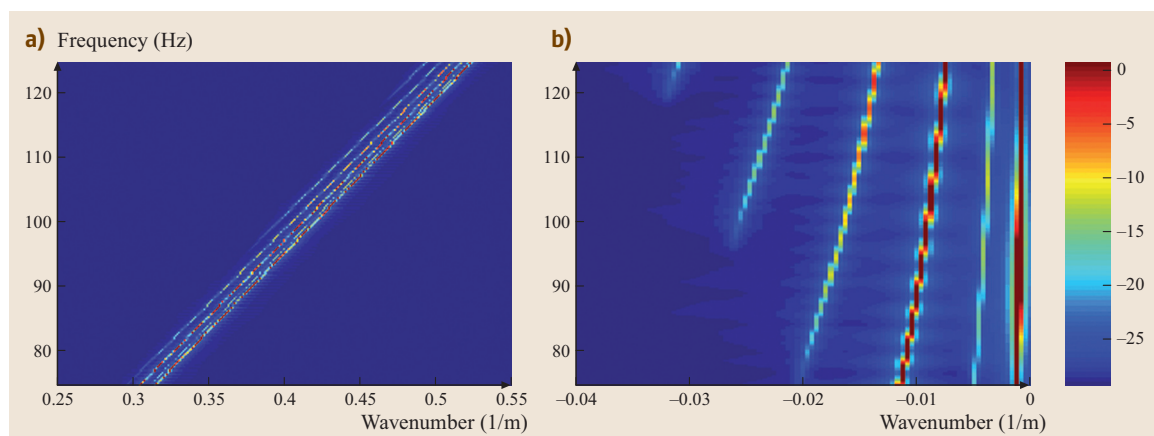


Fig. 5.26a,b Frequency-wavenumber representation of the dispersed field in the waveguide. (a) Obtained from a two-dimensional FFT of the range-time plot in Fig. 5.25. The wavenumbers of propagating modes are bounded by the upper and lower sound speeds in waveguide, ω/c_ω and ω/c_b . (b) A rotated version of (a), so that the sound speed in water appears infinite. This representation is easier to see the mode separation and the mode cut-off frequency. The color scale is in dB

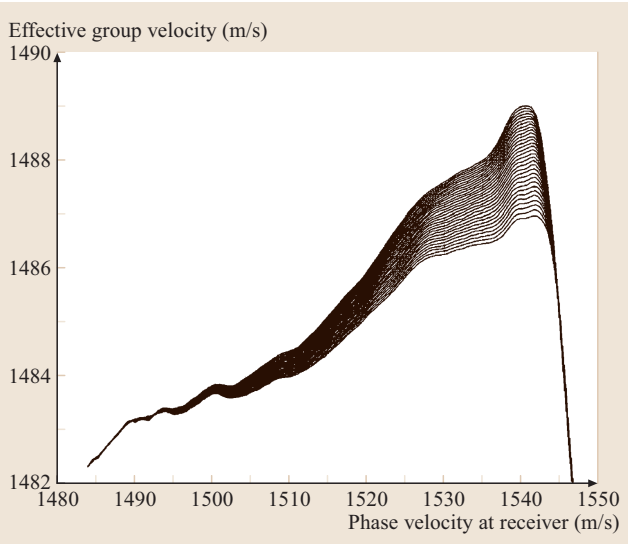


Fig. 5.27 Group speed versus phase speed in the Pacific Deep water case. The curves are for different frequencies starting with the lowest frequency 60 Hz being on top. Low phase velocity corresponds to low mode number ▶

that become more vertical such as when the bottom has a very high speed and hence, large critical angle with respect to the horizontal. In addition, for elastic propagation, the compressional and shear waves span a wide angle interval. Finally, Fourier synthesis for pulse modeling requires high accurate in phase and the high-angle PEs are more accurate in phase, even at low angles.

Equation (5.61) with the second-order range derivative which was neglected because of (5.60) can be written in operator notation as

$$[P^2 + 2iK_0 P + K_0^2(Q^2 - 1)]\psi = 0, \quad (5.63)$$

where

$$P \equiv \frac{\partial}{\partial r}, Q \equiv \sqrt{n^2 + \frac{1}{K_0^2} \frac{\partial^2}{\partial z^2}}. \quad (5.64)$$

Factoring (5.64) assuming weak range dependence and retaining only the factor associated with outgoing propagation yields a one-way equation

$$P\psi = iK_0(Q - 1)\psi, \quad (5.65)$$

which is a generalization of the parabolic equation beyond the narrow-angle approximation associated with (5.60). If we define $Q = \sqrt{1+q}$ and expand Q in a Taylor series as a function of q , the standard PE method is recovered by $Q \approx 1 + 0.5q$. The wide-angle PE to arbitrary accuracy in angle, phase, etc. can be obtained from a Padé series representation of the Q operator,

$$Q \equiv \sqrt{1+q} = 1 + \sum_{j=1}^n \frac{a_{j,n}q}{1+b_{j,n}q} + O(q^{2n+1}), \quad (5.66)$$

where n is the number of terms in the Padé expansion and

$$\begin{aligned} a_{j,n} &= \frac{2}{2n+1} \sin^2\left(\frac{j\pi}{2n+1}\right), b_{j,n} \\ &= \cos^2\left(\frac{j\pi}{2n+1}\right). \end{aligned} \quad (5.67)$$

The solution of (5.65) using Eqs. (5.66) and (5.67) has been implemented using finite-difference techniques for fluid and elastic media.

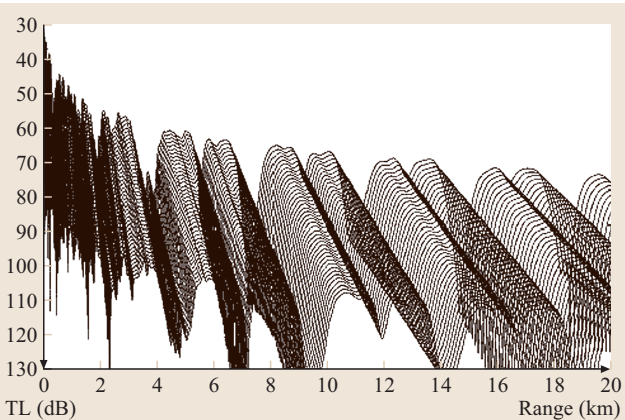


Fig. 5.28 Transmission loss versus range from 130 to 170 Hz calculated by OASES (Ocean Acoustic Seismic Exploration Synthesis) for an environment composed of a 200 m homogeneous fluid layer overlying a homogeneous, absorbing fluid half-space. The fluid layer has a 1450 m/s sound speed, whereas the bottom half-space has a sound speed of 1500 m/s and an attenuation of $10 \text{ dB}/\lambda$. The curves for increasing frequencies are progressively offset in 1 dB steps. The source and receiver depths are 20 and 100 m, respectively

Generalized or Higher-Order PE Methods

Methods of solving the parabolic equation, including extensions to higher-angle propagation, elastic media, and direct time-domain solutions including nonlinear effects have recently appeared (for example, see [5.34]). In particular, accurate high-angle solutions are important when the environment supports acoustic paths



5.4.6 Propagation and Transmission Loss

Propagation loss (PL) and transmission loss (TL) are decibel (see Appendix) quantities that are either measured or derived from propagation models. They represent the loss in intensity of the acoustic field as a function of range as referenced to some location. For modeling, we typically use the intensity at one meter range from the source using the assumption of spherical spreading over that one meter. Hence, if P is the output of a propagation code, the propagation loss is

$$\text{PL} = 20 \log \left| \frac{P}{p_0(r=1)} \right| \equiv -\text{TL}, \quad (5.68)$$

where p_0 is the pressure of the source in free space. Transmission loss is a positive quantity.

Often, one sees references to coherent and incoherent propagation loss, which can be confusing. Deterministic physics has all acoustic propagation as coherent. If the medium has some randomness, than phase information is lost by some sort of averaging process. This leads to the idea of incoherent propagation. In normal-mode theory, the results is that the cross terms involving differences of modal wavenumbers do not contribute and the propagation curve is therefore smooth, without the interference pattern (Fig. 5.30c). Clearly such a calculation is easy with modes, but there is no equivalent simple way for the other wave models other than actually to introduce randomness. Figure 5.30 shows an application of this incoherent sum of modes. In shallow water an incoherent sum of modes is more or less equivalent to frequency smoothing, over, for example a third of an octave. The environment shown in Fig. 5.30a corresponds to experimental data contours of third-octave transmission loss as a function of frequency and range shown in Fig. 5.30b. Normal-mode model runs are shown in Fig. 5.30c, in which the modes are summed incoherently. Figure 5.30d is a model result of the same type of mode computations, but over the whole frequency spectrum; note the excellent agreement. This kind of analysis can be iteratively used to estimate the environment. Figures 5.30b and 5.30d are referred to an optimum frequency curves in the sense that 300–400 Hz appears to be the optimum frequency of propagation. For example, a vertical slice at 60 km indicates that the minimum loss is in that frequency interval. The curves in Fig. 5.30c are horizontal slices of the contour plot in Fig. 5.30d. The optimum frequency comes from the combination of high loss into the bottom at low frequency because

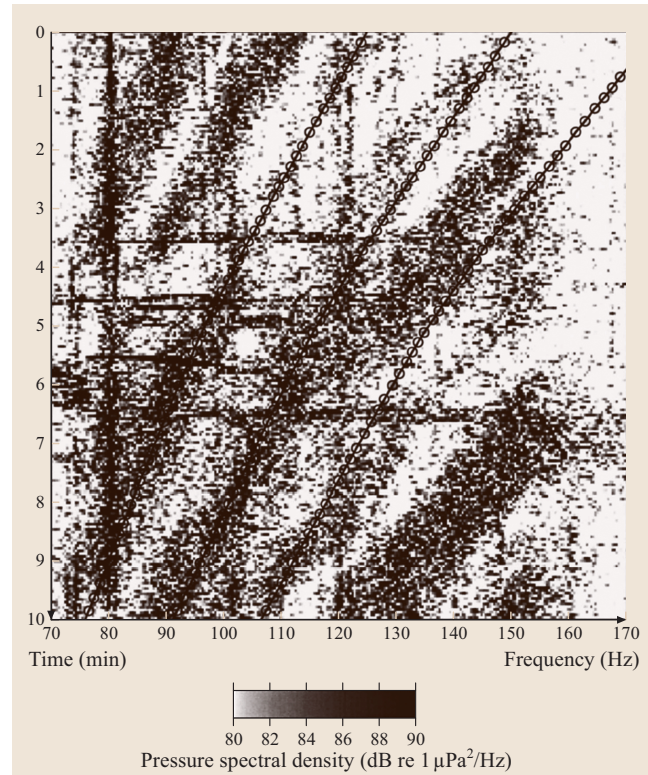


Fig. 5.29 A data example of spectrogram of a broadband moving source. The striations are the peaks in the interference pattern of the transmission loss. The time axis is converted to range if one knows the path and speed of the source (after [5.35])

of increased penetration into the lossy bottom and high losses at high frequency caused by scattering and other water volume attenuation effects that tend to have a frequency-squared dependence. Hence, the existence of an intermediate frequency at which bottom loss is small and frequency-squared dependence is not yet dominant.

Finally we note that there is also an incoherent sum of rays in which ray intensities and not amplitudes with phases are summed. This is not the equivalent of an incoherent sum of mode. For example, an incoherent sum of modes does not produce convergence zones while incoherent rays show convergence-zone properties.

5.4.7 Fourier Synthesis of Frequency-Domain Solutions

Using a Fourier transform, the frequency-domain solution $p(r, z, \omega)$ of the wave equation can be transformed



28 Part A | Propagation of Sound

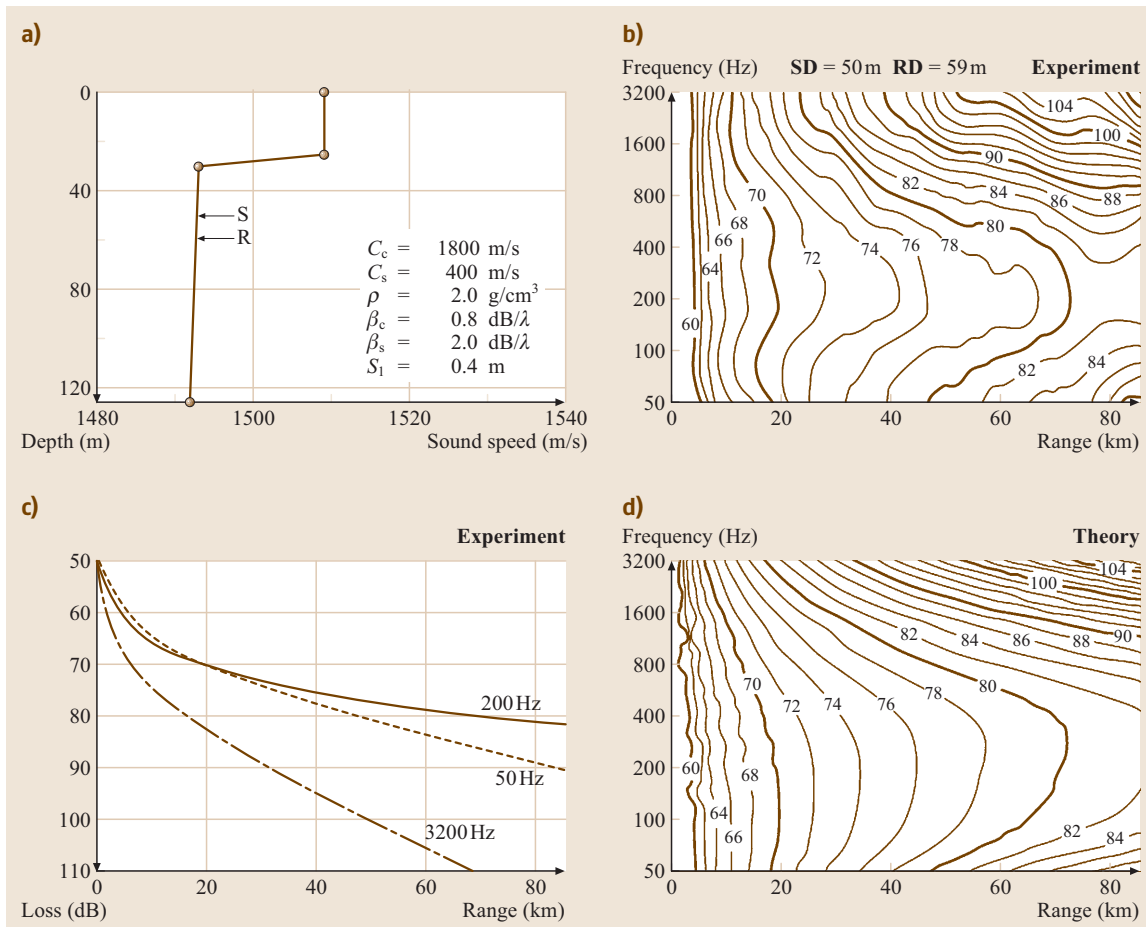


Fig. 5.30a–d Optimum frequency curves for a shallow-water environment. (a) The shallow-water environment. Source and receiver depths are marked by the arrows. (b) Contour of third-octave transmission loss data over frequency and range. (c) Incoherent normal-mode transmission loss. (d) Contour of incoherent transmission loss looking very much like the data in (b)

into the time-dependent solution $p(r, z, t)$. We have

$$p(r, z, t) = \frac{1}{2\pi} \int_{-\infty}^{+\infty} S(\omega) p(r, z, \omega) e^{-i\omega t} d\omega. \quad (5.69)$$

$S(\omega)$ is the source spectrum defined as

$$S(\omega) = \int_{-\infty}^{+\infty} s(t) e^{i\omega t} dt, \quad (5.70)$$

where $s(t)$ is the pulse source for which the time-domain solution $p(r, z, t)$ is investigated. Before (5.69)

can be used, the transfer function $p(r, z, \omega)$ has to be determined from one of the frequency-domain (or continuous-wave (CW)) propagation models described above at a number of discrete frequencies within the frequency band of interest. This means the ocean response to a pulse $s(t)$ is obtained by combining the convenient and computationally efficient CW codes (spectral integrals, normal-mode or parabolic equations) with a Fourier synthesis approach. Even if this last step is conceptually simple, there are several numerical issues that have to be addressed like frequency and time windowing, and aliasing.

The first step in evaluating the frequency integral by means of a (fast) Fourier transform is to reduce the in-



tegration interval. The source pulse $s(t)$ being known, a frequency interval $(\omega_{\min}, \omega_{\max})$ is determined, outside which the source does not emit any significant energy. Moreover, the final time-domain solution $p(r, z, t)$ being real, we know that $p(r, z, -\omega) = p(r, z, \omega)$. This reduces the integration performed in (5.69) to the interval $[\omega_{\min}, \omega_{\max}]$

$$p(r, z, t) = \operatorname{Re} \left[\frac{1}{\pi} \int_{\omega_{\min}}^{\omega_{\max}} S(\omega) p(r, z, \omega) e^{-i\omega t} d\omega \right]. \quad (5.71)$$

Now, the set of discrete frequencies on which the integration has to be performed on the interval $[\omega_{\min}, \omega_{\max}]$ depends on both the choice of the sampling frequency F_s of the signal and some a priori knowledge of the time spread T of the final solution $p(r, z, t)$. First, the sampling frequency F_s has to satisfy the Nyquist criterium $F_s > 2f_{\max} = (\omega_{\max}/\pi)$. Typically, to allow for a reasonably looking graphical signal display, an appropriate value is $F_s = 8f_{\max}$. Second, the time window T of the signal after propagation through the ocean should be taken as short as possible. However, this time window must be chosen in accordance with the waveguide physics. A conservative way to estimate the time spread is to consider that T is bounded by the slowest and fastest available speeds for the particular

environment:

$$T = t_{\max} - t_{\min} \geq R \left(\frac{1}{c_{\min}} - \frac{1}{c_{\max}} \right), \quad (5.72)$$

where R is the propagation range. With the proper choice of T and F_s , we construct an N -point time vector $\mathbf{t} = [0 : \frac{1}{F_s} : T]$, with $N = F_s T + 1$ and a frequency vector $\frac{\omega}{2\pi} = [0 : \frac{F_s}{N} : F_s(1 - \frac{1}{N})]$. The time vector \mathbf{t} corresponds to the time axis on which the time-dependent solution $p(r, z, t)$ will be computed from the frequency bins of the frequency vector ω inside the interval $[\omega_{\min}, \omega_{\max}]$. Before computing the Fourier transform, it is necessary to add a retarded time to the integral $\exp(-it_{\min}\omega)$ so that the time vector \mathbf{t} starts at the earliest possible arrival $t = t_{\min} + [0 : \frac{1}{F_s} : T]$. From (5.80), a reasonable choice for t_{\min} is $t_{\min} = (R/c_{\max})$. It follows:

$$p(r, z, t) = \operatorname{Re} \left\{ \operatorname{IFFT} \left[S(\omega) p(r, z, \omega) e^{-i\omega t_{\min}} \right]_{\omega_{\min}}^{\omega_{\max}} \right\}, \quad (5.73)$$

where the inverse fast Fourier transform (IFFT) is performed on the frequency vector ω in the interval $[\omega_{\min}, \omega_{\max}]$. We do not discuss here the numerous (fast) Fourier transform algorithms, which can be found in signal processing or numerical methods books. Typical results of this broadband modeling are presented in Figs. 5.22–5.25.

5.5 Quantitative Description of Propagation

All of the models described above attempt to describe reality and to solve in one way or another the Helmholtz equation. They therefore should be consistent and there is much insight to be gained from understanding this consistency. The models ultimately compute propagation loss which is taken as the decibel ratio (see Appendix) of the pressure at the field point to a reference pressure, typically one meter from the source.

Figure 5.31 shows convergence-zone-type propagation for a simplified profile. The ray trace in Fig. 5.31b shows the cyclic focusing discussed in Sect. 5.1.2. The same profile is used to calculate normal modes, shown in Fig. 5.31c which, when summed according to (5.50) referenced to 1 m, exhibits the same cyclic pattern as the ray picture. Figure 5.31d shows both the normal-mode (wave theory) and ray theory result. Ray theory exhibits sharply bounded shadow regions as expected whereas the normal-mode theory, which includes

diffraction, shows that the acoustic field does exist in the shadow regions and the convergence zones have structure.

Normal-mode models sum the discrete modes that roughly correspond to angles of propagation within the cone of Fig. 5.7a. The spectral method can include the full field, discrete plus continuous, the latter corresponding to larger angles. The discussion below (5.50) defines these angles in terms of horizontal wavenumbers, and the eigenvalues of the normal-mode problem are a discrete set of horizontal wavenumbers. Hence the integrand (Green's function) of the spectral method has peaks at the eigenvalues associated with the normal modes. These peaks are shown on the right of Fig. 5.32a. The smoother portion of the spectrum is the continuous part, corresponding to the larger angles. Therefore, the consistency we expect between the normal-mode and the spectral method and the physics

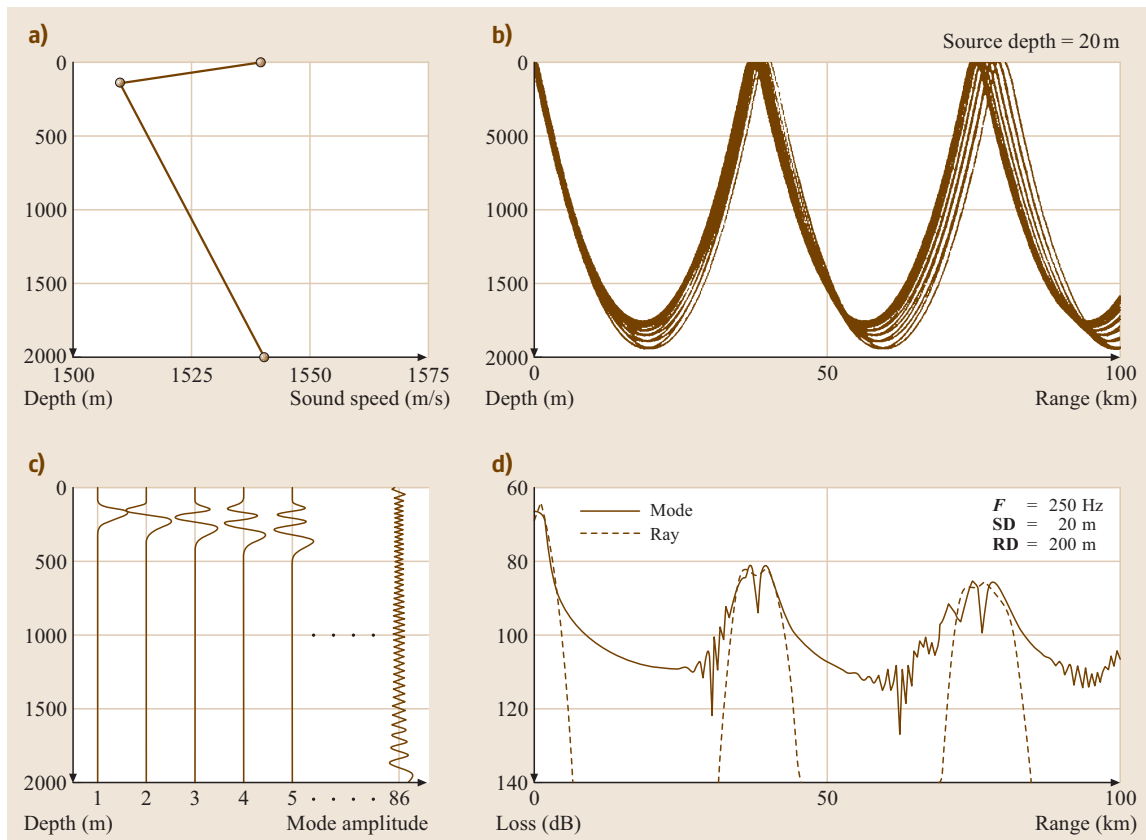


Fig. 5.31a–d Consistency between ray theory and normal mode theory. (a) Sound-speed profile, (b) ray trace, (c) normal modes, (d) propagation calculations. The shadow zones in (d) are much sharper for ray theory which does not include diffraction effects

of Fig. 5.7 is that the continuous portion of the spectral solution decays rapidly with range so that there should be complete agreement at long range between the normal-mode and spectral solutions. The Lloyd's mirror effect, a near-field effect, should also be exhibited in the spectral solution but not the normal-mode solution. These aspects are apparent in Fig. 5.32b. The PE solution is in good agreement with the other solutions but with some phase error associated with the average wavenumber that must be chosen in the split-step method. The PE solution, which contains part of the continuous spectrum including the Lloyd's mirror beams, is more accurate than the normal-mode solution at short range; however, the generalized PE can be made arbitrarily accurate at short range by including more expansion terms in (5.66).

Range-dependent results are shown in Fig. 5.33. A ray trace, a ray trace field result, a PE result and data are plotted together for a range-dependent sound-speed profile environment. The models agree with the data in general, with the exception that the ray results predict too sharp a leading edge for the convergence zone.

Up-slope propagation is modeled with the PE in Fig. 5.34. As the field propagates up-slope, sound is dumped into the bottom in what appears to be discrete beams. The flat region has three modes and each is cut off successively as sound propagates into the shallower water. The ray picture also has a consistent explanation for this phenomenon. The rays for each mode become steeper as they propagate up-slope. When the ray angle exceeds the critical angle the sound is significantly transmitted into the bottom.



5.6 SONAR Array Processing

Signal processing is common to many fields [5.36–38]. In this section we emphasize applications to underwater acoustics, mainly concentrating on spatial processing of pressure fields. We note, though, that there is also growing interest in processing vector fields such as acoustic displacement, velocity or acceleration [5.39]. Further, the array processing discussed below for passive SONARs is also applicable to active SONAR signal processing. Spatial sampling of a sound field is usually done by an array of transducers, although the synthetic aperture array, in which a sensor is moved through space to obtain measurements in both the time and space domains, is an important exception. Spatial sampling is analogous to temporal sampling with the sampling interval replaced by the sensor spacing. The Nyquist criterion requires that the sensor spacing be at least twice the spatial wavenumber of the measured sound field. Finally, we note that recently work of processing ambient noise fields have proven to yield information about the ocean environment [5.40, 41].

5.6.1 Linear Plane-Wave Beam-Forming and Spatio-Temporal Sampling

The simplest example of array processing is phase shading in the frequency domain (or time delay in the time domain) to search for the bearing of a plane-wave signal. This procedure is referred to as plane wave beam-forming, or delay and sum beam-forming in the time domain. For simplicity we consider a liner array and we take θ as the bearing angle associated with the plane-wave signal as shown in Fig. 5.35a.

Frequency-Domain Processing

A plane wave can be represented as

$$s(\theta) = \exp(i\mathbf{k} \cdot \mathbf{r}), \quad (5.74)$$

where we have suppressed the time dependence $\exp(-i\omega t)$ and $k = |\mathbf{k}| = (\omega/c)$. The field is summed in phase if the receiving element (hydrophone or microphone) inputs at position \mathbf{d} is multiplied by the complex conjugate of the plane-wave phase factor,

$$\omega_i^* = \exp(-i\mathbf{k}_s \cdot \mathbf{d}_i) = \exp[-i\mathbf{d}(k \sin \theta_s)], \quad (5.75)$$

where θ_s is a scanning angle. This process will have a maximum when the scanning angle equals the incident angle of the signal.

The output of this beam-forming process is denoted $B(\theta_s)$, but often it is the power output of the beamformer that is of interest:

$$\begin{aligned} B(\theta_s) &= \left| \sum_{i=1}^m \omega_i^*(\theta_s) [s_i(\theta) + n_i] \right|^2 \\ &= \sum_{i,j=1}^m \omega_i^*(\theta_s) (s_{ij} + n_{ij}) \omega_j(\theta_s), \end{aligned} \quad (5.76)$$

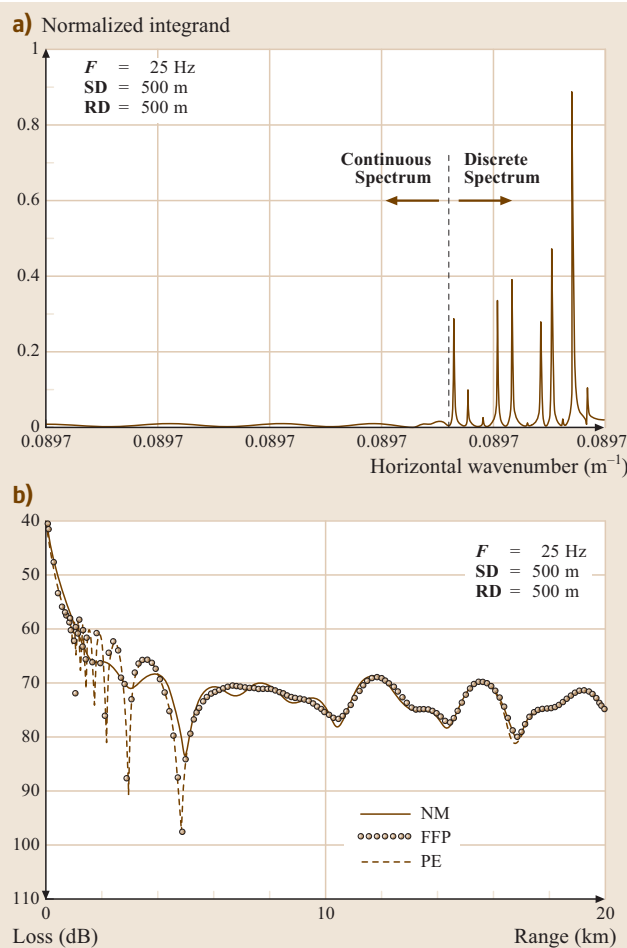


Fig. 5.32a,b Relationship between spectral (FFP), normal-mode (NM) and split-step parabolic-equation model (PE) computations. (a) FFP Green's function from (5.44). (b) Normal-mode, spectral (FFP) and PE propagation results showing some agreement in the near field and complete agreement in the far field. Higher-order PE methods will give identical results to the FFP



32 Part A | Propagation of Sound

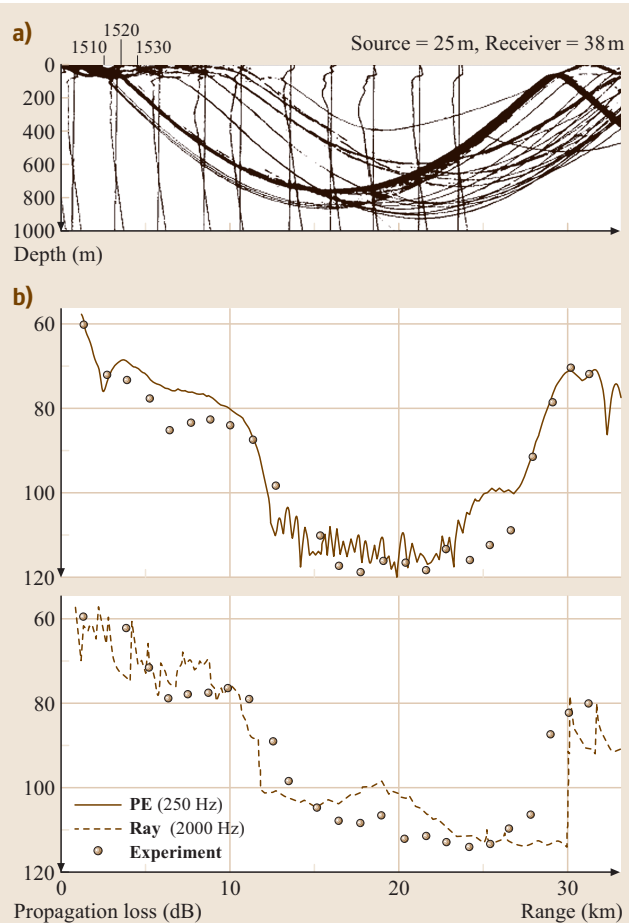


Fig. 5.33a, b Model and data comparison for a range-dependent case. (a) Profiles and ray trace for a case of a surface duct disappearing. (b) 250 Hz PE and 2 kHz ray-trace comparisons with data. Again, the diffraction-less ray theory shows more abrupt change in field

where s_i and n_i are the signal and noise at the i -th receiving element and where $s_{ij} + n_{ij}$ are elements of a cross-spectral density matrix which, when obtained from data, would involve Fourier transforms and ensemble averages as mentioned in the discussion below (5.78) augmented by Fig. 5.35b. In writing down the right-hand side of (5.76), the signal and noise fields were assumed to be mutually incoherent.

We can write the above expression in matrix notation where the boldface lower-case letters denote vectors and boldface upper-case letters denote matrices. Define a steering column vector \mathbf{w} whose i -th element is w_i and a cross-spectral density matrix (CSDM) \mathbf{K} of

the signal and noise with elements $K_{ij} = s_{ij} + n_{ij}$ since the signal and noise are assumed to be independent. Equation (5.76) can be rewritten as

$$B(\theta_s) = \mathbf{w}^\dagger(\theta_s) \mathbf{K}(\theta_{\text{true}}) \mathbf{w}(\theta_s) \equiv \mathbf{w}^\dagger \mathbf{K} \mathbf{w}, \quad (5.77)$$

where \dagger denotes the complex transpose. The CSDM or the covariance of the field is composed of uncorrelated signal and noise covariances,

$$\mathbf{K} = \mathbf{K}_s + \mathbf{K}_n. \quad (5.78)$$

The data across the array as represented in the matrix \mathbf{K} contains the information that the source is in the direction θ_{true} . Sometimes $\mathbf{w}(\theta_s)$ is referred to as a replica and this beam-forming process is viewed as matching the received data across the array with a replica. The type of beam-former represented by (5.77) is called a linear or Bartlett beam-former.

For the sample covariance estimation we assume we have an array with N sensors located at \mathbf{d}_i , $i = 1, 2, \dots, N$ and a narrow-band model as illustrated in Fig. 5.35b. These covariances are estimated by segmenting the received data, $r_i(t)$ into snapshots using a sampling window, $W(t)$, that is unity in the interval $[0, T_w]$,

$$R_i^l(f) = \int_{T_l}^{T_l+T_w} r_i(t) W(t - T_l) e^{-i2\pi f t} dt, \quad (5.79)$$

where here the notation uses frequency f , rather than angular frequency ω . In most beam-forming algorithms the data vectors are averaged to form the sample covariance matrix

$$\hat{\mathbf{K}}(f) = \frac{1}{L} \sum_{l=1}^L R^l(f) R^l(f)^H, \quad (5.80)$$

where L is the number of snapshots.

Time-Domain Processing

Time delaying a signal is the time-domain analog to phase shading of the signal in the frequency domain. In general, the time domain is a viable alternative to frequency analysis when processing coherent broadband signals such as temporal impulse. Time-delay beam-forming is then the frequency equivalent of the phase beam-forming described in Sect. 5.6.1. Indeed, it can be derived formally by taking the Fourier transform of the beam-forming process with the result that the beam-



former output is

$$\begin{aligned} b(\theta, t) &= \int_{-\infty}^{\infty} B(\theta, \omega) \exp(i\omega t) d\omega \\ &= \int_{-\infty}^{\infty} \sum_i R_i(\omega) \exp\left(-i\frac{\omega}{c_i} d_i \sin \theta\right) \\ &\quad \times \exp(i\omega t) d\omega \\ &= \sum_i R_i(t - \frac{d_i}{c_i} \sin \theta), \end{aligned} \quad (5.81)$$

where $R_i(t)$ is the time domain data, d_i the location and c_i the sound speed at the i -th phone. Physically speaking, the delay $\tau_i = (d_i/c_i) \sin \theta$ is, to a first approximation, the time delay associated with the phase shift in the frequency-domain array processing. A more rigorous approach in the case of a strong depth dependence of the sound-speed profile leads to

$$\tau_i = \int_{d_0}^{d_i} \sqrt{\frac{1}{c^2(z)} - \frac{\cos^2(\theta)}{c^2(d_0)}} dz, \quad (5.82)$$

where d_0 is the depth of a reference hydrophone on the array. Note that, in the case of a uniform sound speed profile over the array, the above processes are plane-wave beam-forming.

Examples of the practical use of time-domain versus frequency-domain beam-forming are discussed below. Consider an incident field on a 20-element vertical array made of seven pulses arriving at different angles in a noisy waveguide environment (Fig. 5.36). The SNR ratio does not allow an accurate detection and identification of the echoes. Time-delay beam-forming results applied on these broadband signals is presented in Fig. 5.37. The SNR of the time-domain processing is a combination of array gain and frequency-coherent processing. In comparison, phase beam-forming performed on the same data and averaged incoherently over frequencies show a degraded detection of the incident echoes (Fig. 5.38).

5.6.2 Some Beam-Former Properties

Figure 5.39 shows the output results of some frequency-domain plane-wave beam-formers for the cases of one and two incident signals. To be noted are the side-lobes of the Bartlett processor and the high-resolution performance of the adaptive processors (discussed in the next section). Some of the general attributes of an array beam-former are:

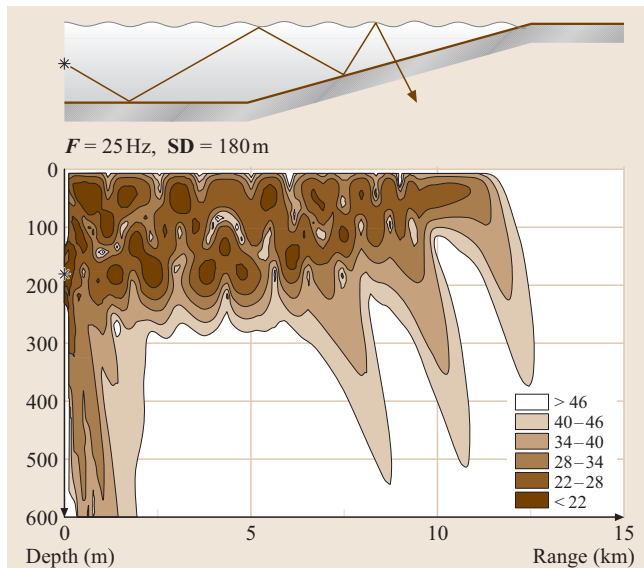


Fig. 5.34 Relation between up-slope propagation (from PE calculation) showing individual mode cut-off and energy dumping in the bottom, and a corresponding ray schematic. In this case, three modes were excited in the flat region. The ray picture shows that a ray becomes steeper as it bounces up slope and when its grazing angle exceeds the critical angle, it is partially transmitted into the bottom (and subsequently with more and more transmission with each successive, higher angle bounce)

- The main response axis (MRA): generally, one normalizes the beam pattern to have 0 dB, or unity gain in the steered direction.
- Beam width: an array with finite extent, or aperture, must have a finite beam width centered about the MRA, which is termed the *main lobe*.
- Side-lobes: angular or wavenumber regions where the array has a relatively strong response. Sometimes they can be comparable to the MRA, but in a well-designed array, they are usually -20 dB or lower, i. e., the response of the array is less than 0.1 of a signal in the direction of a side-lobe.
- Wavenumber processing: rather than scan through incident angles, one can scan through wavenumbers, $k \sin \theta_s \equiv \kappa_s$; scanning through all possible values of κ_s results in nonphysical angles that correspond to waves not propagating at the acoustic medium speed. Such waves can exist, such as those associated with array vibrations. The beams associated with these wavenumbers are sometimes referred to as virtual beams. An important aspect of these beams is that their

underwater propagation
phase conjugation (PC)
PC (phase conjugation)
CSDM (cross-spectral-density matrix)
minimum-variance distortionless processor (MV)
MV (minimum-variance distortionless processor)
maximum-likelihood method (MLM)
MLM (maximum-likelihood method)
matched field processing (MFP)
MFP (matched field processing)



34 Part A | Propagation of Sound

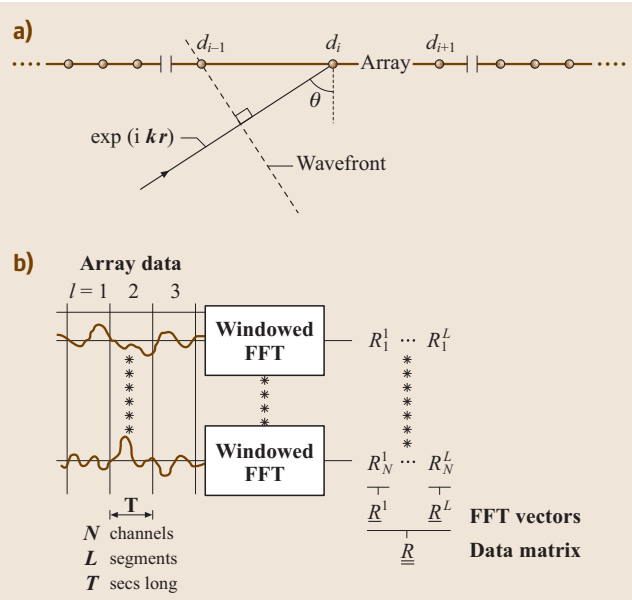


Fig. 5.35a,b Array processing. (a) Geometry for plane-wave beam-forming. (b) The data is transformed to the frequency domain in which the plane-wave processing takes place. The cross-spectral-density matrix (CSDM) is an outer product of the data vector for a given frequency

side-lobes can be in the physical angle region, thereby interfering with acoustic propagating signals.

- Array gain: defined as the decibel ratio of the signal-to-noise ratios of the array output to a single phone

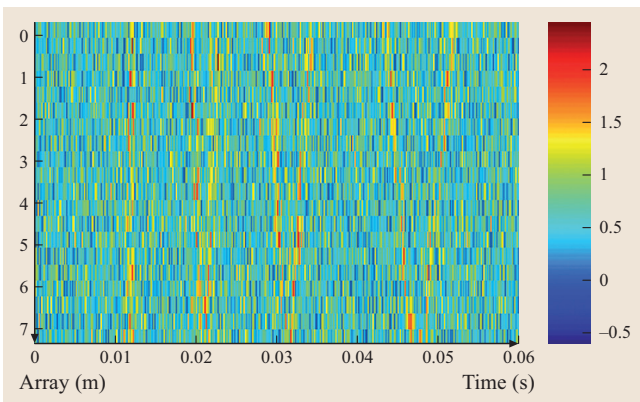


Fig. 5.36 Depth-versus-time representation of simulated broadband coherent data received on a vertical array in the presence of ambient noise. The wavefronts corresponding to different sources are nearly undistinguishable

output. If the noise field is isotropic, the array gain is also termed the directionality index.

5.6.3 Adaptive Processing

There are high-resolution methods to suppress side-lobes, usually referred to as adaptive methods since the signal processing procedure constructs weight vectors that depend on the received data itself. We briefly describe one of these procedures: the minimum-variance distortionless processor (MV), sometimes also called the maximum-likelihood method (MLM) directional spectrum-estimation procedure.

We seek a weight vector \mathbf{w}_{MV} applied to the matrix \mathbf{K} such that its effect will be to minimize the output of the beam-former (5.77) except in the look direction, where we want the signal to pass undistorted. The weight vector is therefore chosen to minimize the functional [5.38]. From (5.72)

$$F = \mathbf{w}_{\text{MV}} \mathbf{K} \mathbf{w}_{\text{MV}} + \alpha(\mathbf{w}_{\text{MV}} \mathbf{w} - 1). \quad (5.83)$$

The first term is the mean-square output of the array and the second term incorporates the constraint of unity gain by means of the Lagrangian multiplier α . Following the method of Lagrange multipliers, we obtain the MV weight vector,

$$\mathbf{w}_{\text{MV}} = \frac{\mathbf{K}^{-1} \mathbf{w}}{\mathbf{w} \mathbf{K}^{-1} \mathbf{w}}. \quad (5.84)$$

This new weight vector depends on the received data as represented by the cross-spectral density matrix; hence, the method is adaptive. Substituting back into (5.77) gives the output of our MV processor,

$$B_{\text{MV}}(\theta_s) = [\mathbf{w}(\theta_s) \mathbf{K}^{-1}(\theta_{\text{true}}) \mathbf{w}(\theta_s)]^{-1}. \quad (5.85)$$

The MV beam-former should have the same peak value at θ_{true} as the Bartlett beam-former, (5.77) but with side-lobes suppressed and a narrower main beam, indicating that it is a high-resolution beam-former. Examples are shown in Fig. 5.39. Of particular practical interest for this type of processor is the estimation procedure associated with Fig. 5.35b and (5.80). One must take sufficient snapshots to allow the stable inversion of the CSDM. This requirement may conflict with source motion when the source moves through multiple beams along the time interval needed to construct the CSDM.

5.6.4 Matched Field Processing, Phase Conjugation and Time Reversal

Matched field processing (MFP) [5.42] is a generalization of plane-wave beam-forming in which data

Fig. 5.37 Angle-versus-time representation of the simulated data in Fig. 5.36 after time-delay beam-forming. All sources appear clearly above the noise with their corresponding arrival angle ►

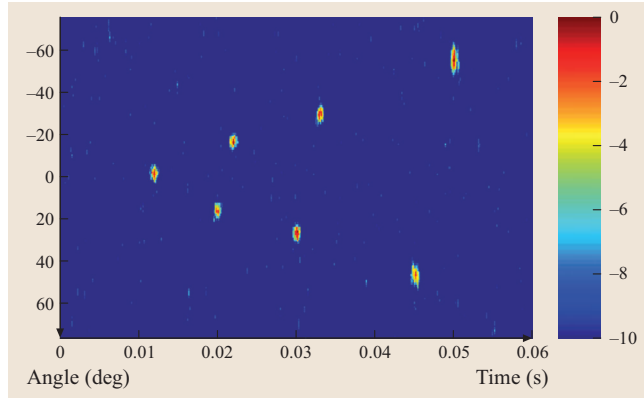
on an array is correlated with replicas from a (waveguide) propagation model for candidate locations \hat{r}, \hat{z} (Fig. 5.40). Localization of a source is accomplished with a resolution consistent with the modal structure and SNR. The central difficulty with MFP is specifying the coefficients and boundary conditions of the acoustic wave equation for shallow water propagation, *i.e.*, knowing the ocean environment in order to generate the replicas. An alternative to performing this model-based processing is phase conjugation (PC), in the frequency domain or, time reversal (TR) in the time domain, in which the conjugate or time-reversed data is used as source excitations on a transmit array co-located with the receive array (Fig. 5.41a) [5.43]. The PC/TR process is equivalent to correlating the data with the *actual* transfer function from the array to the original source location. In other words, both MFP and PC are signal processing analogs to the mechanical lens adjustment feedback technique used in adaptive optics: MFP uses data together with a model (note the feedback arrow in Fig. 5.40) whereas PC/TR is an active form of adaptive optics simply retransmitting phase-conjugate/time-reversed signal through the same medium (e.g., see result of Fig. 5.41). Though time reversal is thought of as an active process, it is presented in this section because of its relation to passive MFP.

Ocean Time-Reversal Acoustics

Phase conjugation, first demonstrated in nonlinear optics and its Fourier conjugate version, time reversal is a process that has recently implemented in ultrasonic laboratory acoustic experiments [5.44]. Implementation of time reversal in the ocean for single elements [5.45] and using a finite spatial aperture of sources, referred to as a *time-reversal mirror* (TRM) [5.46], is now well established.

The geometry of a time-reversal experiment is shown in Fig. 5.41. Using the well-established theory of PC and TRM in a waveguide, we just write down the result of the phase-conjugation and time-reversal process, respectively, propagating toward the focal position

$$P_{pc}(r, z, \omega) = \sum_{j=1}^J G_\omega(r, z, z_j) G_\omega^*(R, z, z_{ps}) S^*(\omega) \quad (5.86)$$



and

$$P_{trm}(r, z, t) = \frac{1}{(2\pi)^2} \sum_{j=1}^J \iint G(r, z, t''; 0, z_j, t') \times G(R, z_j, t'; 0, z_{ps}, 0) \times S(t'' - t + T) dt dt'', \quad (5.87)$$

where S is the source function, $G_\omega^*(R, z, z_{ps})$ is the frequency-domain Green's function and $G(R, z_j, t'; 0, z_{ps}, 0)$ is the time-domain Green's function (TDGF) from the probe source at depth z_{ps} to each element of the SRA at range R and depth z_j . Emphasizing the time-domain process, $G(r, z, t''; 0, z_j, t')$ is the TDGF

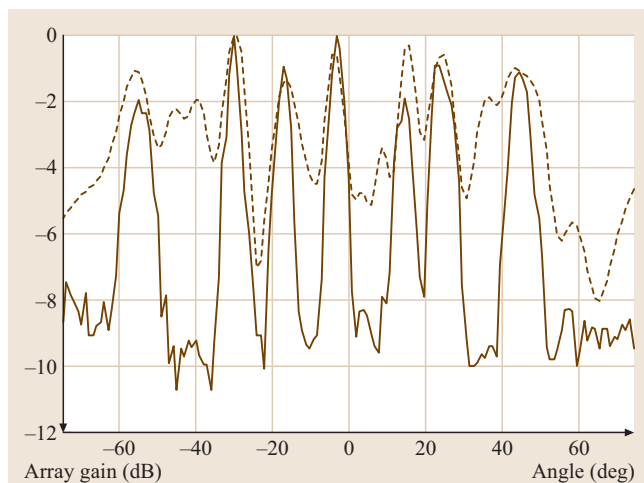


Fig. 5.38 Comparison between coherent time-delay beam-forming (in red) and incoherent frequency-domain beam-forming (in blue) for the simulated data shown in Fig. 5.35. When data come from coherent broadband sources, time-domain beam-forming show better performance than frequency analysis

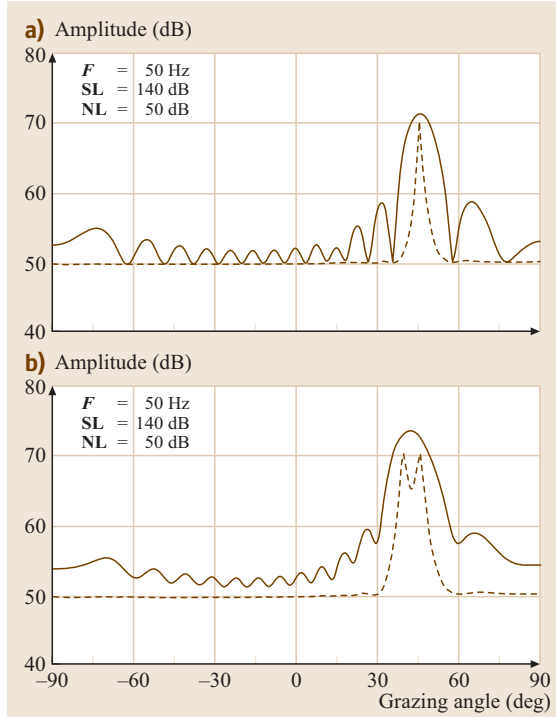


Fig. 5.39a,b Simulated beam-former outputs. **(a)** Single sources at a bearing of 45°. **(b)** Two sources with 6.3° angular separation. *Solid line:* linear processor (Bartlett). *Dashed line:* minimum variance distortion-less processor (MV) showing that the side-lobes are suppressed

from each element of the SRA back to range r and depth z . The focused field at the probe source position is $P_{\text{frm}}(R, z_{\text{ps}}, t)$. The summation is performed on the J elements of the TRM. The signal $S(t'' - t + T)$ of duration τ is the time-reversed version of the original probe source signal and the derivation of (5.87) uses the causality requirement, $T > 2\tau$, i.e., the time reversal interval T must contain the total time of reception and transmission at the SRA, 2τ .

Figure 5.41a–c shows the result of a TRM experiment. The size of the focus is consistent with the spatial structure of the highest-order mode surviving the two-way propagation and can also be mathematically described by a virtual array of sources using image theory in a waveguide.

Matched Field Processing

Linear matched field processing (MFP) can be thought of as the passive signal-processing implementation of phase conjugation. Referring to the phase-conjugation

process described by (5.86), rename $S^* G^*$ as the data at each array element and call the data vector on the array $R(a_{\text{true}})$, where a_{true} represents the (unknown) location of the source (Fig. 5.35b). Now in phase conjugation, G represents an actual propagation from the source array. In MFP, we do the propagation numerically using one of the acoustic models, but rather than use the actual Green's function, we use a normalized version of it called a replica: $\omega(a) = G(a)/|G(a)|$, where $G(a)$ is a vector of Green's functions of dimension of the number of array elements that represents the propagation from a candidate source position to the array elements and is the magnitude of the vector over the array elements. Taking the square of the PC process with replica's replacing the Green's functions yields the beam-former of the matched field processor

$$B_{\text{mf}}(a) = \omega^H(a)K(a_{\text{true}})\omega(a), \quad (5.88)$$

where a realization of the CSDM on the array is then $K(a_{\text{true}} = R(a_{\text{true}})R^H(a_{\text{true}})$ and a sample CSDM is built up as per (5.80).

MFP works because the unique spatial structure of the field permits localization in range, depth and azimuth depending on the array geometry and complexity of the ocean environment. The process is shown schematically in Fig. 5.40. MFP is usually implemented by systematically placing a test point source at each point of a search grid, computing the acoustic field (replicas) at all the elements of the array and then correlating this modeled field with the data from the real point source, $K(a_{\text{true}}) = RR^H$, whose location is unknown. When the test point source is co-located with the true point source, the correlation will be a maximum. The scalar function $B_{\text{mf}}(a)$ is also referred to as the ambiguity function (or surface) of the matched field processor because it also contains ambiguous peaks which are analogous to the side-lobes of a conventional plane-wave beam-former. Side-lobe suppression can often be accomplished by using the adaptive beam-forming methods discussed in the plane-wave section.

Adaptive processors are very sensitive to the accuracy of the replica functions which, in turn, require almost impossible knowledge of the environment. Hence, much work has been done on developing robust forms of adaptive processing such as the white-noise constraint method and others [5.47, 48]. An example of matched field processing performed incoherently on eight tones between 50 Hz and 200 Hz is shown in Fig. 5.42.

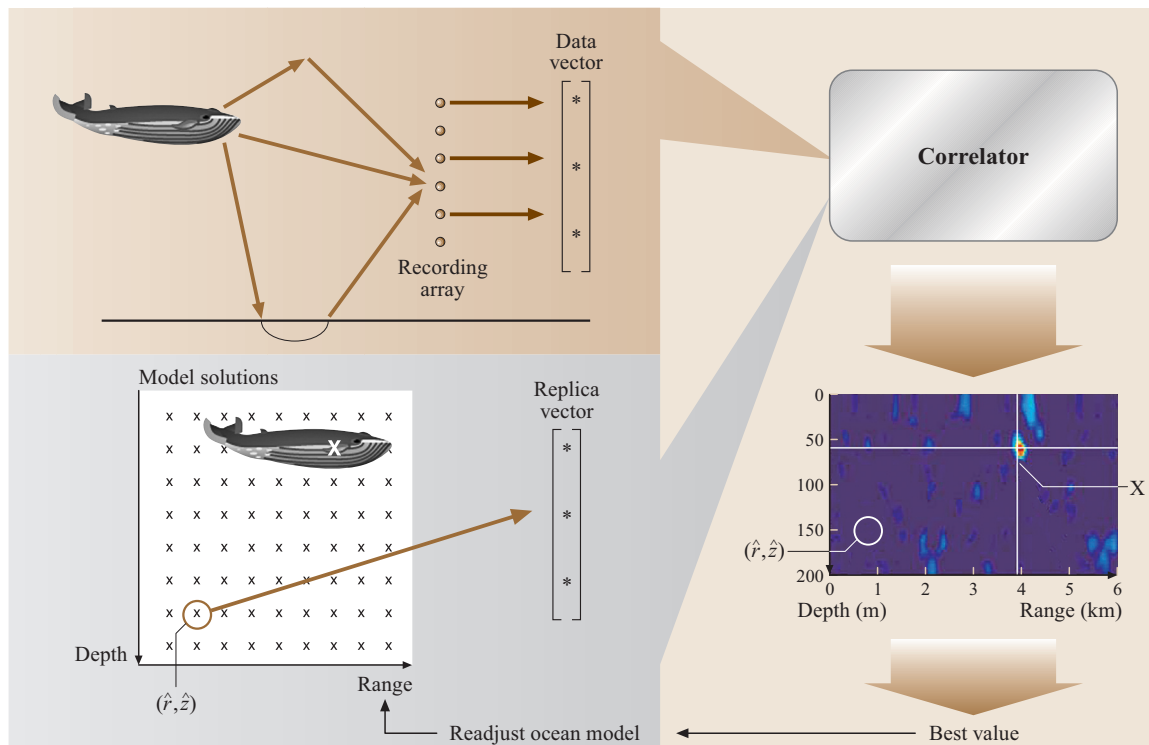


Fig. 5.40 Matched field processing (MFP). Here, the example consists in localizing a singing whale in the ocean. If your model of waveguide propagation is sufficiently accurate for this environment, then comparing the recorded sounds – the whale's data vector – one frequency at a time, for example, with replica data based on best guesses of the location (\hat{r}, \hat{z}) that the model provides, will eventually yield its location. The red peak in the data indicates the location of highest correlation. The small, circled \times represents a bad guess, which thus does not compare well with the measured data. The feedback loop suggests a way to optimize the model: by fine-tuning the focus – the peak resolution in the plot – one can readjust the model's bases (for example, the sound-speed profile). That feedback describes a signal-processing version of adaptive optics. Matched field processing can then be used to perform acoustic tomography in the ocean (after [5.49])

Part A | 5.7

5.7 Active SONAR Processing

An active SONAR system transmits a pulse and extracts information from the echo it receives as opposed to a passive SONAR system, which extracts information from signals received from radiating sources. An active SONAR system and its associated waveform is designed to detect targets and estimate their range, Doppler (speed) and bearing or to determine some properties of the medium such as ocean bottom bathymetry, ocean currents, winds, particulate concentration, etc. The spatial processing methods already discussed are applicable to the active problem so that in this section we emphasize the temporal aspects of active signal processing.

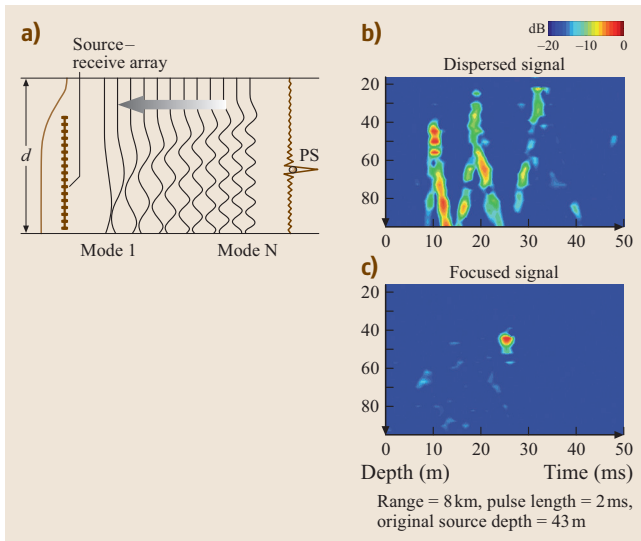
5.7.1 Active SONAR Signal Processing

The basic elements of an active SONAR are: the (waveform) transmitter, the channel through which the signal, echo and interference propagates, and the receiver [5.50]. The receiver consists of some sort of matched filter, a square-law device, and possibly a threshold device for the detector and range, Doppler and bearing scanners for the estimator.

The matched filter maximizes the ratio of the peak output signal power to the variance of the noise and is implemented by correlating the received signal with



38 Part A | Propagation of Sound



Part A | 5.7
 the transmitted signal. A simple description of the received signal, $r(t)$, is that it is an attenuated, delayed, and Doppler-shifted version of the transmitted signal $s_t(t)$,

$$r(t) \rightarrow \text{Re} [\alpha e^{i\theta} s_t(t-T) e^{2\pi i f_c t} e^{2\pi i f_d t} + n(t)], \quad (5.89)$$

where α is the attenuation transmission loss and target cross section, θ is a random phase from the range

uncertainty compared to a wavelength, T is the range delay time, f_c is the center frequency of the transmitted signal and f_d is the Doppler shift caused by the target. The correlation process will have an output related to the following process,

$$C(a) = \left| \int \tilde{r}(t) \tilde{s}(t; a) dt \right|^2, \quad (5.90)$$

where $\tilde{s}(t; a)$ is a replica of the transmitted signal modified by a parameter set a which include the propagation–reflection process, e.g., range delay and Doppler rate. For the detection problem, the correlation receiver is used to generate a sufficient statistic which is the basis for a threshold comparison in making a decision if a target is present. The performance of the detector is described by receiving operating characteristic (ROC) curves which plot the detection of probability versus false-alarm probability, as parameterized by a statistics of the signal and noise levels. The parameters a set the range and Doppler value in the particular resolution cell of concern. To estimate these parameters, the correlation is done as a function of a .

For a matched filter operating in a background of white noise detecting a point target in a given range–Doppler resolution cell, the detection signal-to-noise ratio depends on the average energy-to-noise ratio and not on the shape of the signal. The waveform becomes

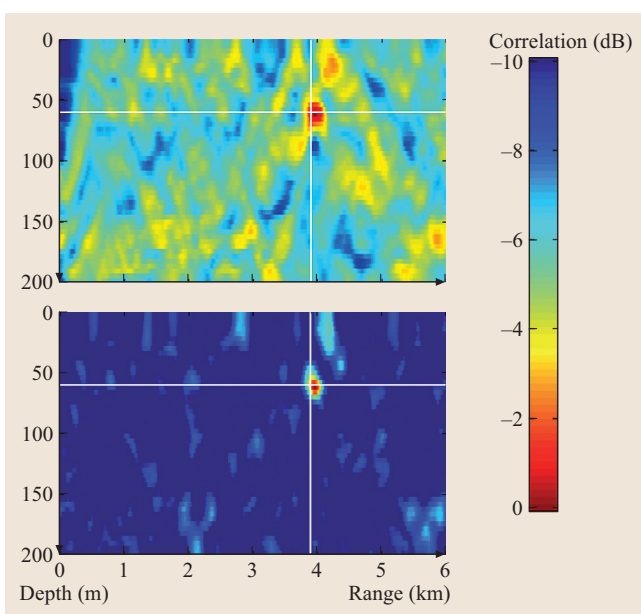


Fig. 5.42a,b Matched field processing example for a vertical array in a shallow-water environment. Specific information regarding the experiment can be found on the web at <http://www.mpl.ucsd.edu/swellex96/>. **(a)** Bartlett result with significant side-lobes only 3 dB down. **(b)** Adaptive processor results shows considerable side-lobe suppression. The processor is actually a *white-noise constrained* MVDP for which the diagonal of the CSDM is deliberately loaded by a specific algorithm to stabilize the processor to some uncertainty in the environment and/or array configuration. The ambiguity surfaces in **(a)** and **(b)** are an incoherent average over eight tones at 53, 85, 101, 117, 133, 149, 165, 181, and 197 Hz ◀



a factor when there is a reverberant environment and when one is concerned with estimating target range and Doppler. A waveform's potential for range and Doppler resolution can be ascertained from the ambiguity function of the transmitted signal. This ambiguity function is related to the correlation process of (5.90) for a transmitted signal scanned as a function of range and Doppler,

$$\Theta(\hat{T}, T_t, \hat{f}_d, f_{dt}) \propto \left| \int \tilde{s}(t - T) \tilde{s}_t(t - \hat{T}) e^{2\pi i (f_{dt} - \hat{f}_d)t} dt \right|^2, \quad (5.91)$$

where T_t and f_{dt} are the true target range (time) and Doppler, and \hat{T} and \hat{f}_d are the scanning estimates of the range and Doppler. Figure 5.43 are sketches of ambiguities functions of some typical waveforms. The range resolution is determined by the reciprocal of the bandwidth and the Doppler resolution by the reciprocal of the duration. A coded or pseudo-random (PR) sequence can attain good resolution of both by appearing as long-duration noise with a wide bandwidth. Ambiguity functions can be used to design desirable waveforms for particular situations. However, one must also consider the randomizing effect of the real ocean. The *scattering function* describes how a transmitted signal statistically redistributes its energy in the reverberant ocean environment which causes multipath and Doppler spread. In particular, in a reverberation-limited environment, only increasing the transmitted power does not change the signal-to-reverberation level. Signal design should minimize the overlap of the ambiguity function of the target displaced to its range and Doppler and the scattering function.

5.7.2 Underwater Acoustic Imaging

Imaging can be divided into categories concerned with water column and bottom properties. Here we describe several applications of active SONAR to imaging the ocean.

Water Column Imaging. Backscatter from particulate objects that move along with the water motion (such as biological matter, bubbles sediments) contains velocity information because of the Doppler shift. An acoustic Doppler current profiler (ADCP) might typically consist of three or four source-receivers pointed in slightly different directions but generally up (from the bottom) or down (from a ship). The multiple directions are for resolving motion in different directions. The Doppler

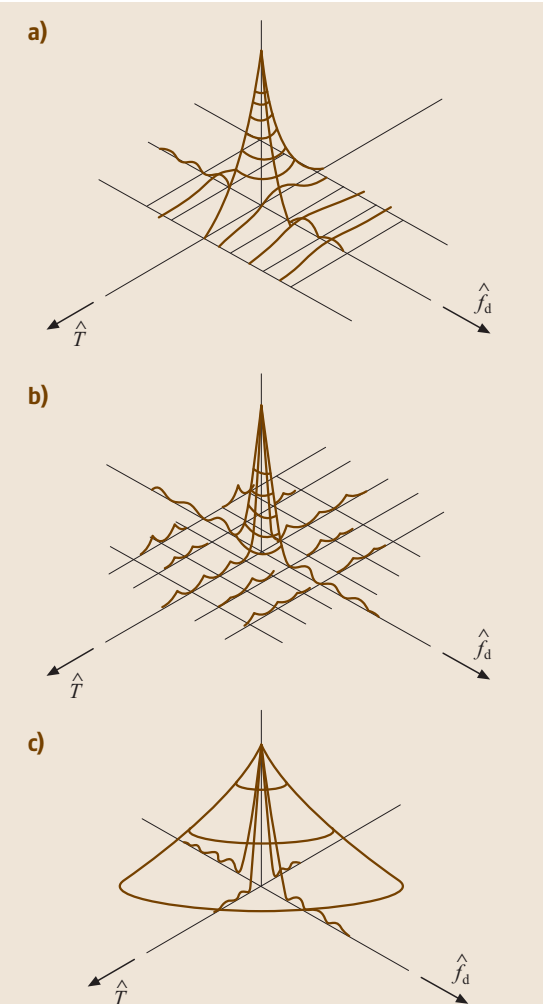


Fig. 5.43a–c Ambiguity function for several SONAR signals: (a) rectangular pulse; (b) coded pulses; (c) chirped FM pulse

shift of the returning scattered field is simply $-2f(v/c)$ (as opposed to the more-complicated long-range waveguide Doppler shift discussed in Sect. 5.4.4), where f is the acoustic frequency, v is the radial velocity of the scatterer (water motion), and c is the sound speed. With three or four narrow-beam transducers, the current vector can be ascertained as a function of distance from an ADCP by gating the received signal and associating a distance with the time gated segment of the signal. Water-column motion associated with internal waves can be determined by this process also where essentially one uses a kind of ADCP points in the horizontal

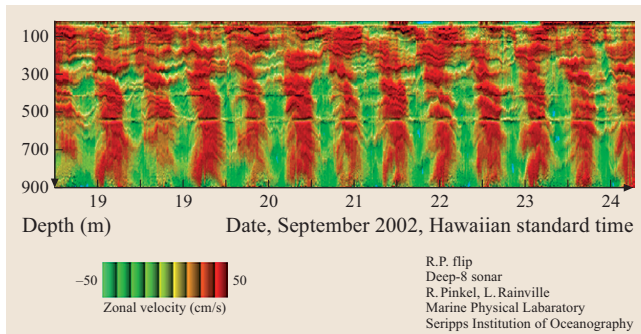


Fig. 5.44 Depth-time representation of the East–West component of water velocity over the Kaena ridge west of Oahu. The dominant signal is the 12.4 h tide, which has downward propagating crests of long vertical wavelength. The SONAR is at ≈ 390 m, where there is a fine scar in the record. The scar at ≈ 550 m is the echo of the sea floor at 1100 m, aliased back into the record (Courtesy Rob. Pinkel, Scripps Institution of Oceanography)

direction. For elaborate images of currents and the internal wave motion (Fig. 5.44), the Doppler measurements of backscattering off zooplankton are combined with array-processing techniques used in bottom mapping as discussed below.

Bottom Mapping. Because of many industrial applications, there exists a huge literature on multibeam systems for bottom mapping. Among the material avail-

able on the web, we would like to refer to two complete courses on submarine acoustic imaging methods available: (1) from the Ocean Mapping Group (University of New Brunswick, Canada) at <http://www.omg.unb.ca/GGE/>; (2) under a PDF format (*Multibeam Sonar: Theory of Operation*) from L3 Communication SeaBeam Instruments at <http://www.mbari.org/data/mbsystem/formatdoc/>. The scope of the paragraph below is to describe the basics and keywords associated with bottom mapping in underwater acoustics.

Active SONARs are devices that emit sound with specific waveforms and listen for the echoes from remote objects in the water. Among many applications, SONAR systems are used as echo-sounders for measuring water depths by transmitting acoustic pulses from the ocean surface and listening for their reflection (or echo) from the sea floor. The time between transmission of a pulse and the return of its echo is the time it takes the sound to travel to the bottom and back. Knowing this time and the speed of sound in water allows one to calculate the range to the bottom. This technique has been widely used to map much of the world's water-covered areas and has permitted ships to navigate safely through the world's oceans. The purpose of a large-scale bathymetric survey is to produce accurate depth measurements for many neighboring points on the sea floor such that an accurate picture of the geography of the bottom can be established. To do this efficiently, two things are required of the SONAR used: it must produce accurate

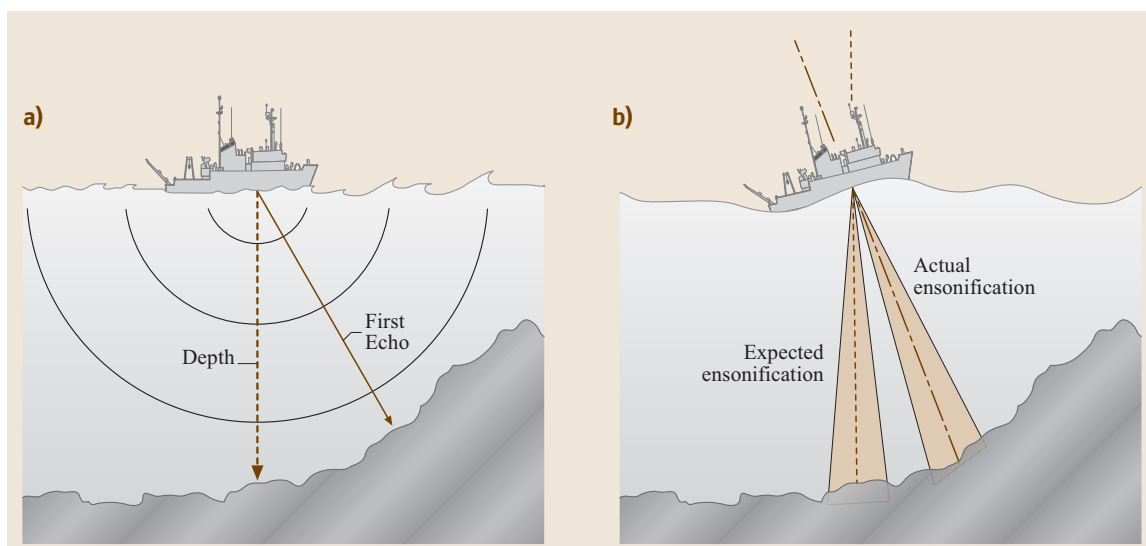


Fig. 5.45a,b Surveying an irregular sea floor (a) with a wide-beam SONAR and (b) with a narrow-beam SONAR (Courtesy L-3 Communications SeaBeam Instruments)



depth measurements that correspond to well-defined locations on the sea floor (that is, specific latitudes and longitudes); and it must be able to make large numbers of these measurements in a reasonable amount of time. In addition, information derived from echo sounding has aided in laying transoceanic telephone cables, exploring and drilling for offshore oil, locating important underwater mineral deposits, and improving our understanding of the Earth's geological processes.

The earliest, most basic and still most widely used echo-sounding devices are *single-beam echo sounders*. The purpose of these instruments is to make serial measurements of the ocean depth at many locations. Recorded depths can be combined with their physical locations to build a three-dimensional map of the ocean floor. In general, single-beam depth sounders are set up to make measurements from a vessel in motion. Until the early 1960s most depth sounding used single-beam echo sounders. These devices make a single depth measurement with each acoustic pulse (or ping) and include both wide- and narrow-beam systems (Fig. 5.45a,b). Relatively inexpensive wide-beam sounders detect echoes within a large solid angle under a vessel and are useful for finding potential hazards for safe navigation. However, these devices are unable to provide much detailed information about the sea bottom. On the other hand, more-expensive narrow-beam sounders are capable of providing high spatial resolution with the small solid angle encompassed by their beam, but can cover only a limited survey area with each ping. Neither system provides a method for creating detailed maps of the sea floor that minimizes ship time and is thus cost-effective.

A *multibeam SONAR* is an instrument that can map more than one location on the ocean floor with a single ping and with higher resolution than those of conventional echo sounders. Effectively, the function of a narrow single-beam echo sounder is performed at several different locations on the bottom at once. These bottom locations are arranged such that they map a contiguous area of the bottom – usually a strip of points in a direction perpendicular to the path of the survey vessel (Fig. 5.46). Clearly, this is highly advantageous. Multibeam SONARs can map complete scans of the bottom in roughly the time it takes for the echo to return from the farthest angle. Because they are far more complex, the cost of a multibeam SONAR can be many times that of a single-beam SONAR. However, this cost is more than compensated by the savings associated with reduced ship operating time. As a consequence, multibeam SONARs are the survey instrument of choice in most mapping applications, particularly in deep

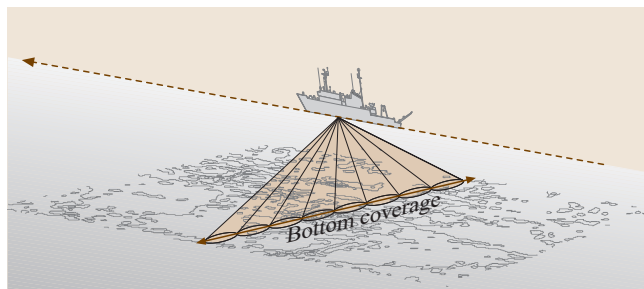


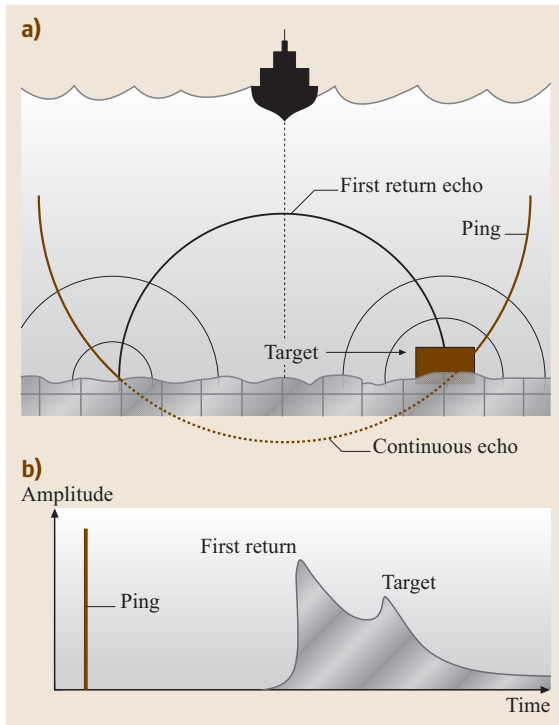
Fig. 5.46 Bottom mapping with a multibeam SONAR system (Courtesy L-3 Communications SeaBeam Instruments)

ocean environments where ship operating time is expensive [5.51]. Multibeam SONARs often utilize the *Mills Cross* technique which takes advantage of the high resolution obtained from two intersecting focusing regions from a perpendicular linear source and receive array.

Instead of measuring the depth to the ocean bottom, a *side-scan SONAR* reveals information about the sea-floor composition by taking advantage of the different sound absorbing and reflecting characteristics of different materials. Some types of material, such as metals or recently extruded volcanic rock, are good reflectors. Clay and silt, on the other hand, do not reflect sound well. Strong reflectors create strong echoes, while weak reflectors create weaker echoes. Knowing these characteristics, you can use the strength of acoustic returns to examine the composition of the sea floor. Reporting the strength of echoes is essentially what a side-scan SONAR is designed to do. Combining bottom-composition information provided by a side-scan SONAR with the depth information from a range-finding SONAR can be a powerful tool for examining the characteristics of an ocean bottom.

The name *side scan* is used for historical reasons – because these SONARs were originally built to be sensitive to echo returns from bottom locations on either side of a survey ship, instead of directly below, as was the case for a traditional single-beam depth sounder [5.52].

Side-scan SONAR employs much of the same hardware and processes as conventional depth-sounding SONAR. Pulses are transmitted by a projector (or array of projectors), and hydrophones receive echoes of those pulses from the ocean floor and pass them to a receiver system. Where side-scan SONAR differs from a depth-sounding system is in the way it processes these returns. While a single-beam echo sounder is only concerned with the time between transmission and the earliest return echo, this first returned echo only marks when



things start to get interesting to a side-scan SONAR (Fig. 5.47a). As it continues its spherical propagation, the transmitted pulse still interacts with the bottom, thus creating at the receiver a continuous series of weakening echoes in time (Fig. 5.47b).

In the example presented in Fig. 5.47, the side-scan SONAR detects a bottom feature (the box). From the amplitude-versus-time plot, an observer can tell there is a highly reflective feature on the bottom. From the time difference between the first echo (which is presumed to be due to the bottom directly below the SONAR system)

Fig. 5.47 (a) Schematic of the spherical wavefronts scattered by a detailed bottom. (b) Amplitude-versus-time representation of the backscattered signal in a side-scan SONAR system (Courtesy L-3 Communications SeaBeam Instruments) ▶

and the echo of the reflective feature, the observer can compute the range to the feature from the SONAR.

As a practical instrument, the simplistic side-scan SONAR described above is not very useful. While it provides the times of echoes, it does not provide their direction. Most side-scan SONARs deal with this problem by introducing some directionality into their projected pulses, and, to some degree, their receivers. This is done by using a line array of projectors to send pulses. The long axis of the line array is oriented parallel to the direction of travel of the SONAR survey vessel (often the arrays are towed behind the ship). In practice, side-scan SONARs tend to mount both the line array and hydrophones on a towfish, a device that is towed in the water below the surface behind a survey vessel (Fig. 5.48). As the survey vessel travels, the towfish transmits and listens to the echoes of a series of pulses. The echoes of each pulse are used to build up amplitude-versus-time plots for each side of the vessel. To adjust for the decline in the strength of echoes due to attenuation, a time-varying gain is applied to the amplitude values so that sea-floor features with similar reflectivities have similar amplitudes. Eventually the noise inherent in the system (which remains constant) becomes comparable to the amplitude of the echo, and the amplified trace becomes dominated by noise. Recording of each trace is usually cut off before this occurs so that the next ping can be transmitted.

Figure 5.49 shows an example of ship-wreck discovery using side-scan SONAR data performed from an automated underwater vehicle (AUV) in a 1500 m-deep ocean.

Often one is interested in sub-bottom profiling that requires high spatial and therefore temporal resolution to image closely spaced interfaces. Frequency-modulated (FM) sweeps provide such high-resolution high-intensity signals after matched filtering. Thus, for example, a matched filter output of a 1 s FM sweep from 2–12 kHz would compresses the energy of the 1 s pulse into one that has the temporal resolution of a 0.1 ms. With such high resolution, reflection coefficients from chirp SONARs can be related to sedimentary characteristics [5.53, 54]. Figure 5.50 is an example of a chirp SONAR output indicating very finely layered interfaces. Figure 5.50a shows the range dependency of the seabed

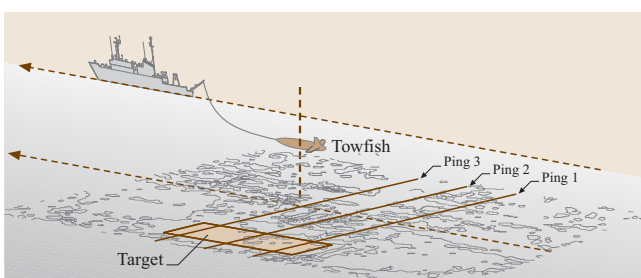


Fig. 5.48 Schematic of a side-scan SONAR imaging the ocean floor with successive pings (Courtesy L-3 Communications SeaBeam Instruments)

ts⁰ Should this be turned into an item of the bibliography?

AUV (automated underwater vehicle)	MIMO (multiple-input multiple-output)!mode
frequency shift keying (FSK)	intersymbol interference (ISI)
FSK (frequency shift keying)	ISI (intersymbol interference)
phase!shift keying (PSK)	
PSK (phase shift keying)	
single-input single-output mode (SISO)	
SISO (single-input single-output mode)	
multiple-input multiple-output (MIMO)	
MIMO (multiple-input multiple-output)	
acoustic!telemetry	
single-input single-output mode (SISO)	
SISO (single-input single-output mode)	
multiple-input multiple-output (MIMO)!mode	

Index entries on this page

along the cross-shelf track taken by a chirp SONAR. Sand ridges with less acoustic penetration occupy most of the mid-shelf area with a few km spacing. In the outer-shelf area, dipping layers over the distinct *R reflector* are detected. The spikes in the water column at the mid-shelf area are schools of fish near the bottom, which were mostly seen during the surveys conducted in daylight. Figure 5.50b shows the sub-bottom profile of the along-shelf track with acoustic penetration as deep as 40 m. Along-shelf track is relatively less range-dependent. However, several scour marks (≈ 100 m wide, a few m deep) are detected on the sea floor. These scour marks are attributed to gouging by iceberg keels and the resultant deformations of deeper sublayers is also displayed [A. Turgut, personal communications]_{TS⁰}.

5.7.3 Acoustic Telemetry

Because electromagnetic waves do not propagate in the ocean, underwater acoustic data transmission have many applications, including:

- Communication between two submarines or a submarine and a support vessel
- Communication between a ship and an automated underwater vehicle (AUV) either to get data available without recovering the instruments or to control the instruments onboard the AUV or the AUV itself
- Data transmission to an automated system

Underwater acoustic communications [5.55] are typically achieved using digital signals. We usually distinguish between coherent and incoherent transmissions. For example, incoherent transmissions might consist of transmitting the symbols “0” and “1” at different frequencies (frequency shift keying (FSK)), whereas coherent transmissions might encode using different phases of a given sinusoid (phase shift keying (PSK)) (Fig. 5.51).

Acoustic telemetry can be performed from one source to one receiver in a single-input single-output mode (SISO). To improve performance in terms of data rate and error rate, acoustic networks are now commonly used. In particular, recent works in underwater acoustic communications deal with multiple-input multiple-output (MIMO) configurations (Fig. 5.52) in shallow-water oceans [5.56].

The trend toward MIMO is justified by the fact that the amount of information – known as the information capacity, I – that can be sent between arrays of transmitters and receivers is larger than in a SISO case. Indeed, the SISO information capacity is given by Shannon’s

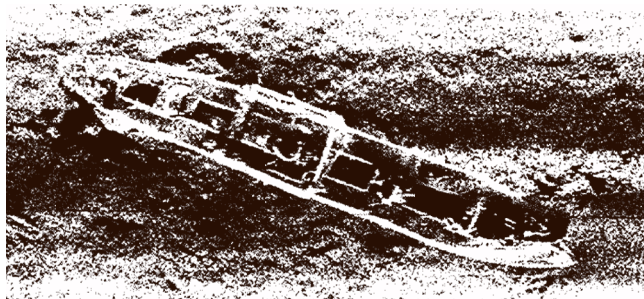


Fig. 5.49 Side-scan SONAR data obtained in 2001 from the HUGIN 3000 AUVs of a ship sunk in the Gulf of Mexico during World War II. C&C Technology Inc. (Courtesy of the National D-Day Museum, New Orleans)

famous formula [5.57]

$$I = \log_2 \left(1 + \frac{S}{N} \right) \text{ bits s}^{-1} \text{Hz}^{-1}, \quad (5.92)$$

where S is the received signal power, N the noise power and the Shannon capacity I is measured in bits per second per Hertz of bandwidth available for transmission. Equation (5.92) states that the channel capacity increases with the signal-to-noise ratio. In a MIMO configuration with M_t transmitters and M_r receivers, (5.92) is changed into [5.58]

$$I \sim M_r \log_2 \left(1 + \frac{SM_r/M_t}{N} \right) \text{ bits s}^{-1} \text{Hz}^{-1}, \quad (5.93)$$

with $M_r \geq M_t$ to be able to decode the M_t separate transmitted signals. Sending M_t different bitstreams is advantageous since it gives a factor of M_t outside the log, linearly increasing the channel capacity I compared to a logarithmic increase when playing on the output power S .

Beside the optimized allocation of power between the M_r and M_t receivers and transmitters (the so-called water-filling approach [5.59]), other particular issues in underwater acoustic telemetry deal with Doppler tracking, channel estimation and signal-to-noise ratios. Those combined parameters often result in a tradeoff between data rate and error rate. For example, low frequencies propagate further with better signal-to-noise ratios and hence lower error rates but the data rate is poor. High frequencies provide high data rates but suffer from strong loss in the acoustic channel, potentially resulting in large error rates.

Another difficulty has to do with multipath propagation and/or reverberation in the ocean, causing intersymbol interference (ISI) and scattering, also called

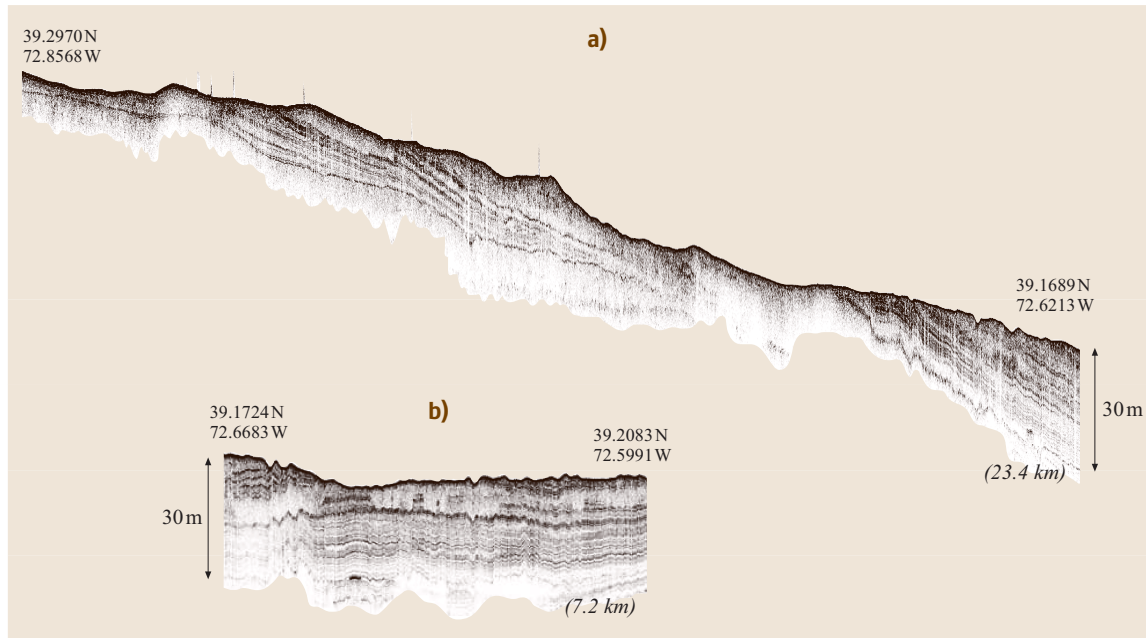


Fig. 5.50a,b Sub-bottom profiles along (a) cross-shelf and (b) along-shelf tracks on the New Jersey shelf collected by a hull-mounted chirp SONAR (2–12 kHz) during the shallow-water acoustic technology experiment (SWAT2000) (Courtesy A. Turgut, Naval Research Laboratory)

the fading effect (Fig. 5.53). As a consequence, the performance of a given system depends strongly on the acoustic environment.

Figure 5.54 shows examples of experimental channel impulse responses recorded at different frequencies in shallow-water waveguides. The difference in temporal dispersion (relative to the acoustic period) between Fig. 5.54a and Fig. 5.54c shows that high-frequency transmissions suffer from stronger ISI and shorter coherence time.

In the presence of ISI, Eqs. (5.92, 93) can be generalized so that the channel capacity I still depends on the signal-to-noise ratio S/N where the noise N now includes ISI [5.60]. However, there exist many ways to reduce propagation effects on the quality of the acoustic transmission. One technological solution is to use directional arrays/antenna. Another one is to further code digital signals (CDMA or turbo codes [5.61]) in order to detect and potentially correct transmission errors. But, most importantly, there are many powerful signal-processing techniques derived from telecommunications to take into account at the receiver of the channel impulse response. An efficient one is adaptive equalization that uses a time-dependent channel estimate in order to decode the next symbols from the previously decoded one [5.62]. Other methods to deal with multipath complexities use time-reversal methods, either alone or with equalization methods [5.63–65].

5.7.4 Travel-Time Tomography

Tomography [5.9, 66] generally refers to applying some form of inverse theory to observations in order to infer properties of the propagation medium. The received field from a source emitting a pulse will be spread in

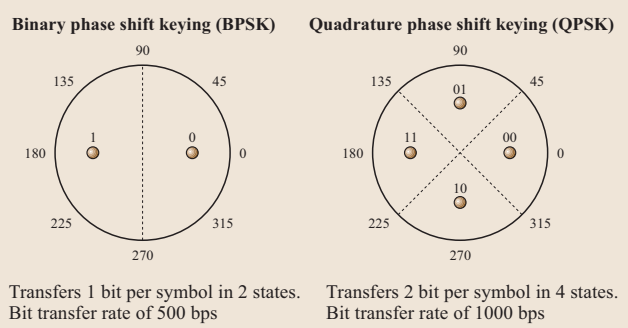


Fig. 5.51 Example of signal space diagrams for coherent communications

quadrature amplitude modulation (QAM)
 multiple-input multiple-output (MIMO)!configuration
 MIMO (multiple-input multiple-output)!configuration
 bit error rate (BER)
 BER (bit error rate)



time as a result of multiple paths, in which different paths have different arrival times (Fig. 5.55). Hence the arrival times are related to the acoustic sampling of the medium. In contrast, standard medical X-ray tomography utilizes the different attenuation of the paths rather than arrival time for the inversion process. Since the ocean sound speed is a function of temperature and other oceanographic parameters, the arrival structure is ultimately related to a map of these oceanographic parameters. Thus, measuring the fluctuations of the arrival times through the experiments theoretically leads to the knowledge of the spatial-temporal scale of the ocean fluctuations.

Tomographic inversion in the ocean has typically relied on these three points. First, only the arrival time (and not the amplitude) of the multipath structure is used as an observable (Table 5.2) [5.67]. Enhanced time-of-arrival resolution is typically obtained using pulse-compression techniques [5.68] as mentioned in the bottom-mapping section above. Depending on the experimental configuration, a choice of compression is to be made between M-sequences [5.69], which are strongly Doppler sensitive but have low temporal side-lobes and frequency-modulated chirps that are Doppler insensitive with higher side-lobes (Fig. 5.43). Second, the inversion is performed by comparing the experimental arrival times to those given by a model (Fig. 5.56). Last, tomographic inversion algorithm classically deals with a linearized problem. This means that the model has to match the experimental data so that the inversion only deals with small perturbations.

Thus, ocean tomography starts from a sound-speed profile $c(\mathbf{r})$ on which small perturbations are added $\delta c(\mathbf{r}, t) \ll c$. The ocean model $c(\mathbf{r})$ has to be accurate enough to relate without ambiguity an experimentally measured travel time T_i to a model-deduced ray path Γ_i . Typically, some baseline oceanographic information is known so that one searches for departures from this baseline information. The perturbation infers a change of travel time δT_i along the ray such that, in a first linear approximation

$$\delta T_i \approx \int_{\Gamma_i} \frac{-\delta c}{c^2} ds, \quad (5.94)$$

where Γ_i correspond to the Fermat path of the unperturbed ray. An efficient implementation of the inversion procedure utilizes a projection of the local sound-speed fluctuations $\delta c(\mathbf{r}, t)$ on a set of chosen functions $\Psi_k(\mathbf{r})$ that constitutes a basis of the ocean structure. We have

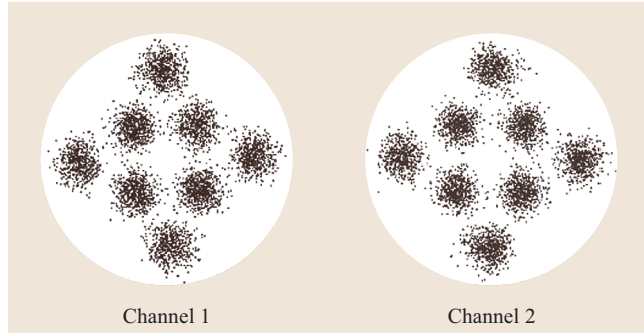


Fig. 5.52 Experimental examples of eight quadrature amplitude modulation (QAM) transmissions in a multiple-input multiple-output configuration (MIMO) at 3.5 kHz in a 9 km-long, 120 m-deep shallow-water ocean. The SNR is 30 dB on channel 1 and 2, the symbol duration is 1 ms (data rate is 8 kB/s per channel) and bit error rate (BER) is 1×10^{-4} (Courtesy H.C. Song, Scripps Institution of Oceanography)

then

$$\delta c(\mathbf{r}, t) = \sum_{k=1}^N p_k(t) \psi_k(\mathbf{r}), \quad (5.95)$$

where $p_k(t)$ is a set of unknown parameters. In its most primitive form, the ocean can be discretized into elementary cells, each cell being characterized by an unknown sound-speed perturbation p_k . Combining the

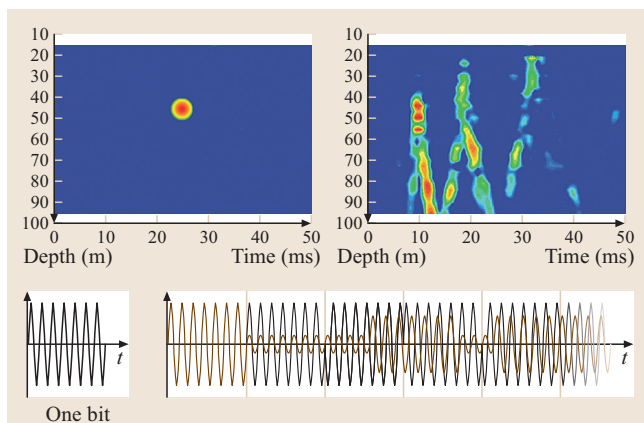
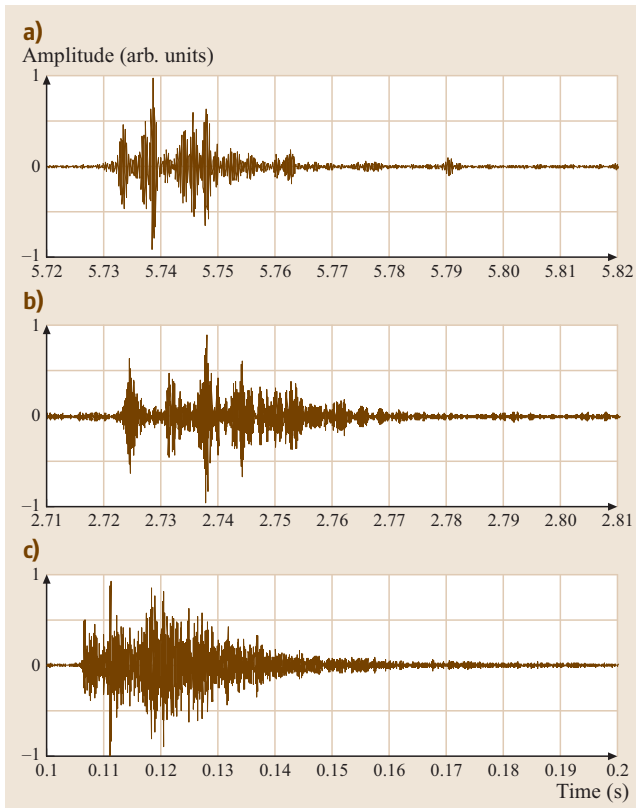


Fig. 5.53 A coherent digital communication system must deal with the intersymbol interference caused by dispersive multipath environment of the ocean waveguide (top right). When a sequence of phase-shifted symbols (in black) are sent, the resulting transmission (in brown) is fading out because of symbol interference



two above equations, it follows

$$\begin{aligned} \delta T_i &= \int_{\Gamma_i} \frac{-1}{c^2} \sum_{k=1}^N p_k \psi_k(\mathbf{r}) ds \\ &= \sum_{k=1}^N p_k \int_{\Gamma_i} \frac{-\Psi_k(\mathbf{r})}{c^2} ds = \sum_{k=1}^N p_k G_{ik}. \end{aligned} \quad (5.96)$$

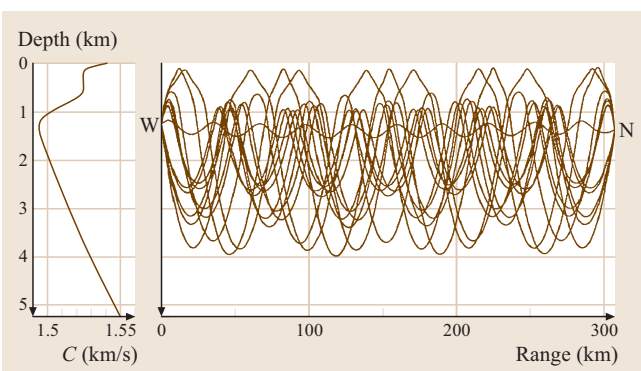


Fig. 5.54a–c Examples of transfer functions recorded at sea in different shallow-water environments at various frequencies. (a) Central frequency = 3.5 kHz with a 1 kHz bandwidth, 10 km range in a 120 m-deep waveguide. (b) Central frequency = 6.5 kHz with a 2 kHz bandwidth, 4 km range in a 50 m-deep waveguide. (c) Central frequency = 15 kHz with a 10 kHz bandwidth, 160 m range in a 12 m-deep waveguide ◀

Allowing for some noise in the measurement and assuming a set of arrival times $\delta T_i, i \in [1, M]$, (5.94) can be rewritten in an algebraic form [5.71]:

$$\delta \mathbf{T} = \mathbf{G} \mathbf{p} + \mathbf{n}. \quad (5.97)$$

There exists many algorithms to obtain an estimate of the parameters $\tilde{\mathbf{p}}$ of the parameters \mathbf{p} from the data $\delta \mathbf{T}$ knowing the matrix \mathbf{G} . For example, when $N > M$, a least-mean-square estimator gives

$$\tilde{\mathbf{p}} = \mathbf{G}^T (\mathbf{G} \mathbf{G}^T)^{-1} \delta \mathbf{T}. \quad (5.98)$$

Considerations about pertinent functions $\Psi_k(\mathbf{r})$ such as empirical orthogonal functions (EOFs) and the optimal inversion procedure can be found in the literature [5.72, 73].

Tomographic experiments have been performed to greater than megameter ranges. For example, two major experiments in the 1990s were performed by the Thetis 2 group in the western Mediterranean over a seasonal cycle [5.74] and by the North Pacific Acoustic Laboratory (NPAL, <http://npal.ucsd.edu>) in the North Pacific basin. The NPAL experiment was directed at using travel-time data obtained from a few acoustic sources and receivers located throughout the North Pacific Ocean to study temperature variations at large scale [5.75, 76]. The idea behind the project, known as acoustic thermometry of ocean climate (ATO), is that sound travels slightly faster in warm water than in cold water. Thus, precisely measuring the time it takes for a sound signal to travel between two points reveals the average temperature along the path. Sound travels at about 1500 m/s in water, while typical changes in the sound speed of the ocean as a result of temperature changes are only 5–10 m/s. The tomography

Fig. 5.55 Left: reference sound-speed profile $C_0(z)$. Right: corresponding ray traces. Table 5.2 identifies all plotted rays. Note the shallow and deep turning groups of rays as well as the axial ray (after [5.70]) (Courtesy Peter Worcester, Scripps Institution of Oceanography) ◀



technique is very sensitive, and experiments so far have shown that temperatures in the ocean can be measured to a precision of 0.01 °C, which is needed to detect subtle variations and trends of the ocean basin.

New trends in ocean tomography deal with full-wave inversion involving the use of both travel times and amplitudes of echoes for a better accuracy in the inversion algorithm. In this case, a full-wave kernel for acoustic propagation has to be used [5.77], which includes the sensitivity of the whole Green's functions (both travel times and amplitudes) to sound speed variations. In the case of high frequencies, the application of the travel-time-sensitivity kernel to an ocean acoustic waveguide gives a picture close to the ray-theoretic one. However, in the low-frequency case of interest in ocean acoustic tomography, there are significant deviations. Low-frequency travel times are sensitive to sound-speed changes in Fresnel-zone-scale areas surrounding the eigen-rays, but not on the eigen-rays themselves, where the sensitivity is zero. This diffraction phenomenon known as the *banana-doughnut* [5.78] debate is still actively discussed in the field of ocean and seismic tomography [5.79].

Table 5.2 Identification of rays (after [5.70]). The identifier is $\pm n(\theta_s, \theta_R, \hat{z}^+, \hat{z}^-)$, where positive (negative) rays depart upward (downward) from the source, n is the total number of upper and lower turning points, θ_s is the departure angle at the source, θ_R is the arrival angle at the receiver, and \hat{z}^+ and \hat{z}^- are the upper and lower turning depths, respectively (Courtesy Peter Worcester, Scripps Institution of Oceanography)

	$\pm n$	θ_s (deg)	θ_R (deg)	\hat{z}^+ (m)	\hat{z}^- (m)
1	8	11.6	11.6	126	3801
2	-8	-11.6	-11.7	125	3803
3	9	12.0	-12.0	99	3932
4	11	11.1	-11.1	617	3624
5	-11	-10.8	10.2	737	3303
6	12	9.7	9.7	776	3170
7	-12	-9.6	-9.7	780	3156
8	13	9.3	-9.3	809	3046
9	-13	-8.2	8.3	881	2746
10	14	7.9	8.0	901	2653
11	-14	-7.8	-7.9	905	2638
12	15	7.4	-7.5	925	2546
13	19	3.5	-3.8	1118	1790
	20	1.2	1.7	1221	1507

5.8 Acoustics and Marine Animals

In the context of contemporary acoustics, marine animal life is typically divided into the categories of marine mammals and non-marine mammals which include fish and other sea animals. The acoustics dealing with fish relates to either finding, counting and catching them. The acoustics concerned with marine mammals is for either studying their behavior or determining to what extent manmade sounds are harmful to them.

5.8.1 Fisheries Acoustics

An extensive introduction to fisheries acoustics is [5.80] and can be found online at <http://www.fao.org/docrep/X5818E/x5818e00.htm#Contents>. For more-detailed information, we recommend two special issues in [5.81, 82].

Following the development of SONAR systems, acoustic technology has had a major impact on fishing and on fisheries research. SONARs and echo sounders are now used as standard tools to search for concentrations of fish or to assess for biomass stock. With

SONAR, it is possible to sample the water column much faster than trawl fishing. Moreover, SONARs have helped in our understanding of how fish are distributed in the ocean and how they behave over time. Depending on the fish density in the water column, echo-counting or echo-integration [5.83] are used to evaluate the fish biomass in the water column. Research on the signature of the echo return for a specific fish [5.84] or for a fish school [5.85, 86] is still an active area of research.

Fisheries acoustics experiments are performed with SONAR in the same way as bottom profiling [5.87–89]. The ship covers the area of interest by transect lines [5.90] while the SONAR sends and receives acoustic pulses (pings) as often as allowed by the SONAR system and the water depth (the signal from the previous ping has to die out before the next ping is transmitted). Typical SONAR frequencies are 38 kHz, 70 kHz, and 120 kHz. An echogram is a display of the instantaneous received intensity along the ship track. The echograms in Fig. 5.57a,b reveal individual fish echoes as well as fish school backscattered signals.

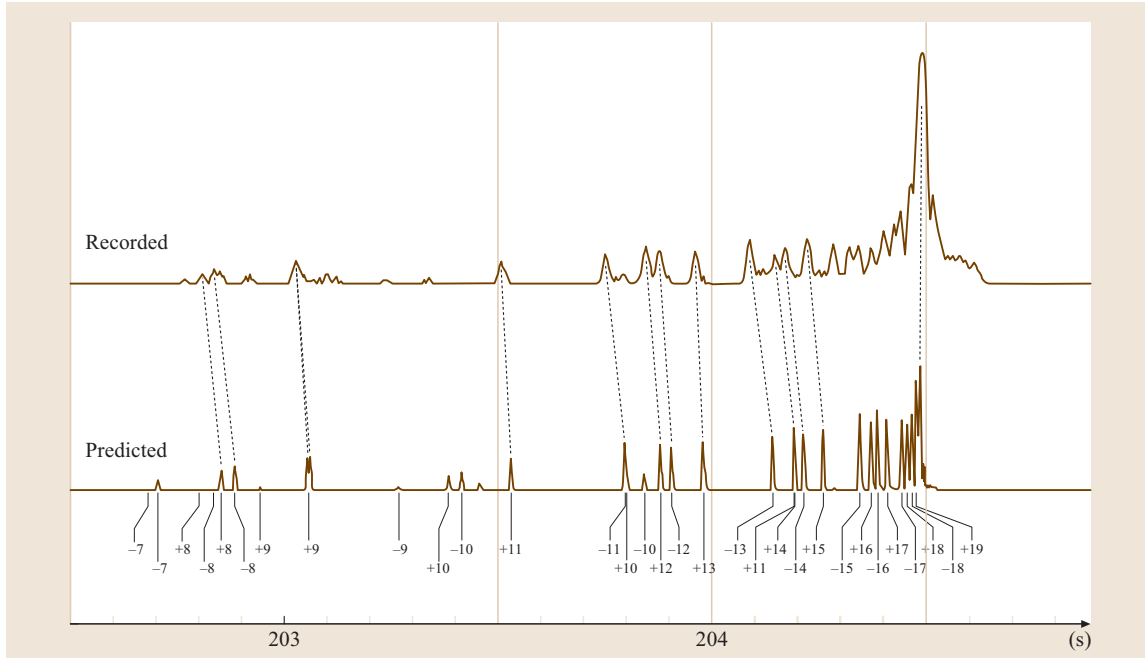


Fig. 5.56 Comparison of the predicted and measured arrival patterns (after [5.70]). The predicted arrival pattern was calculated from $C_0(z)$ as shown in Fig. 5.55. Geometric arrivals are labeled $\pm n$ as in Table 5.2. The peaks connected by dashed lines are the ray arrivals actually used (Courtesy Peter Worcester, Scripps Institution of Oceanography)

From a practical point of view, the relationship between an acoustic target and its received echo can be understood from the SONAR equation. With the procedure of Sect. 5.3.2 and 5.3.3, the echo level (in decibels) of a given target is

$$EL = SL + RG + TS - 2TL, \quad (5.99)$$

where SL is the source level and TL is the geometrical spreading loss in the medium. The target strength TS is defined as $TS = 10 \log_{10}(\sigma/4\pi)$, where σ is the backscattering cross section of the target. The receiver gain RG is often set up as a time-varied gain (TVG), which compensates for the geometrical spreading loss.

In (5.99), the target is supposed to be on the acoustic axis of the transducer. In general, a single-beam SONAR cannot distinguish between a small target on the transducer axis and a big target off-axis. The two echoes may have the same amplitude because the lower TS for the small target will be compensated by the off-axis power loss for the big target. One way to remove this ambiguity is to use a dual-beam SONAR [5.91] (or split-beam SONAR) that provides the position of the target in the beam pattern.

Echo-integration consists of integrating in time (as changed into depth from $R = ct/2$) the received intensity coming from the fish along the ship transects [5.92]. This value is then converted to a biomass via the backscattering cross section σ . In the case of a single target (Fig. 5.57a), the intensity of the echo E_1 is

$$E_1 = \bar{\sigma} \phi^2(r) \left[\frac{\exp(-2\beta r)}{r^4} \right], \quad (5.100)$$

where $\phi^2(R)$ is the depth-dependent (or time-varying) gain; the term in bracket describes the geometrical spreading ($1/r^4$) and loss ($\exp(-2\beta r)$) of the echo during its round trip between the source and the receiver and $\bar{\sigma}$ is the scattering cross section of the target averaged over the bandwidth of the transmitted signal. In (5.100) we did not include the effect of the beam pattern and the sensitivity of the system in emission-reception. These parameters depend on the type of SONAR used and are often measured in situ from a calibration experiment [5.93, 94]. In the case of a distributed targets in the water column [5.95, 96] (Fig. 5.57b), the received intensity E_h is integrated over a layer h at a depth r , which



Fig. 5.57a,b Typical echogram obtained during an echo-integration campaign using a single-beam SONAR on the Gambie river. (a) Biomass made of individual fish. (b) Biomass made of fish school (Courtesy Jean Guillard, INRA) ▶

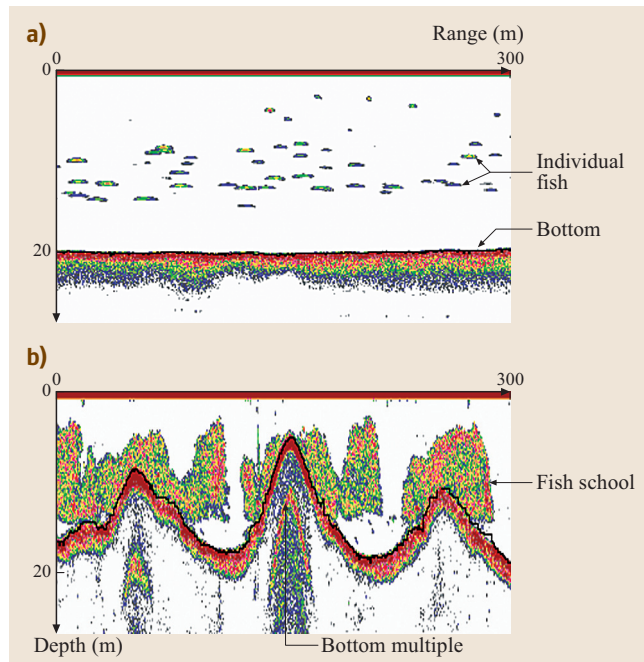
gives

$$E_h = h\bar{\sigma}n\phi^2(r) \left[\frac{\exp(-2\beta r)}{r^2} \right], \quad (5.101)$$

where n corresponds to the density of fish per unit volume in the layer h . Equation (5.101) is based on the linearity principle assumption, which states that, on the average over many pings, the intensity E_h is equal to the sum of the intensity produced by each fish individually [5.97].

In the case of either a single or multiple targets, the idea is to relate directly the echo-integrated result E_1 or E_h to the fish scattering amplitudes $\bar{\sigma}$ or $n\bar{\sigma}$. To that goal, the time-varying gain $\phi^2(r)$ has to compensate appropriately for the geometric and attenuation loss. For a volume integration, $\phi^2(r) = R^2 \exp(2\beta r)$, the so-called $20 \log r$ gain is used while a $40 \log r$ gain is applied in the case of individual echoes.

As a matter of fact, acoustic instruments, such as echo sounders and SONAR, are unique as underwater sampling tools since they detect objects at ranges of many hundreds of meters, independent of water clarity and depth. However, until recently, these instruments could only operate in two dimensions, providing observational slices through the water column. New trends in fisheries acoustics incorporate the use of multibeam SONAR – typically used in bottom mapping, see Sect. 5.7.2 – which provides detailed data describing the internal and external three-dimensional (3-D) structure of underwater objects such as fish schools [5.98] (Fig. 5.58). Multibeam SONARs are now used in a wide variety of fisheries research applications including: (1) three-dimensional descriptions of school structure and position in the water column [5.99]; knowledge of schooling is vital for understanding many aspects of



fish (and fisheries) ecology [5.100]; (2) detailed internal images of fish schools, providing insights into the organization of fish within a school, for example, indicating the presence of large gaps or vacuoles and areas of higher densities or nuclei (Fig. 5.58b,d) [5.101].

In general, one tries to convert the echo-integration result into a biomass or fish density. This requires the knowledge of the target strength TS or the equivalent backscattering cross section σ of the target under

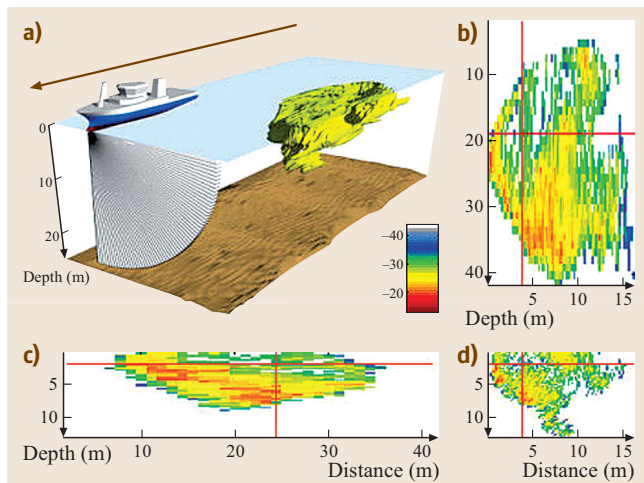


Fig. 5.58a-d Images of a fish school of *Sardinella aurita* from a multibeam SONAR. Arrows indicate vessel route. (a) 3-D reconstruction of the school. Multibeam SONAR receiving beams are shown at the front of the vessel. Remaining panels show cross sections of density in fish from: (b) the horizontal plane, (c) the vertical plane along-ships, (d) the vertical plane athwart ships. Red cross-hairs indicate location of the other two cross sections (Courtesy Francois Gerlotto, IRD) ▶



investigation [5.102]. Several models attempt to develop equations expressing σ/λ^2 as a function of L/λ , where L is the fish length. However, physiological and behavioral differences between species make a more empirical approach necessary, which often is of the form:

$$TS = 20 \log L + b, \quad (5.102)$$

where b depends on the acoustic frequency and the fish species. For example, we have $b = -71.3$ dB for herring and $b = -67.4$ dB for cod at 38 kHz, which makes the cod scattering cross section twice that of herring for the same fish length. In situ measurements of TS with fish at sea [5.103, 104] or in cages [5.105] have also been attempted to classify fish species acoustically.

Similar works on size distribution assessment have been performed at higher frequency (larger than 500 kHz) on small fish or zooplankton using multi-element arrays [5.106] and wide-band or multi-frequency methods [5.107, 108]. The advantage of combining the acoustic signature of fish at various frequencies is to provide an accurate target sizing. When multi-elements are used, then the position of each individual inside the acoustic beam is known. Using simultaneously multi-element arrays and broadband approaches may also be the key for the unsolved problem of species identification in fisheries acoustics.

In conclusion, SONAR systems and echo integration are now well-established techniques for the measurement of fish abundance. They provide quick results and accurate information about the pelagic fish distribution in the area covered by the ship during the survey. The recent development of multibeam SONAR has improved the reliability of the acoustic results and now provides 3-D information about fish-school size and shape. However, some important sources of error remain when performing echo-integration, among which are: (1) the discrimination between fish echoes and unwanted target echoes, (2) the difficulty of adequately sampling a large area in a limited time, (3) the problems related to the fish behavior (escaping from the transect line, for example) and (4) the physiological parameters that determine the fish target strength.

5.8.2 Marine Mammal Acoustics

In order to put into perspective both the sound levels that mammals emit and hear, we mention an assortment of sounds and noise found in the ocean. Note that the underwater acoustic decibel scale used is, as per the

Appendix, relative to 1 μPa . For source levels, one is also referencing the sound level at 1 m. Lightening can be as high as 260 dB and a seafloor volcanic eruption can be as high as 255 dB. Heavy rain increases the background noise by as much as 35 dB in a band from a few hundred Hz to 20 kHz. Snapping shrimp individually can have broadband source levels greater than 185 dB while fish choruses can raise ambient noise levels 20 dB in the range of 50–5000 Hz. Of course, the Wenz curves in Fig. 5.15 show a distribution of natural and manmade noise levels whereas specific examples of manmade noise are given in Table 5.3.

Table 5.3 Examples of manmade noise

Ships underway	Broadband source level (dB re 1 μPa at 1 m)
Tug and barge (18 km/hour)	171
Supply ship (example: Kigoriak)	181
Large tanker	186
Icebreaking	193
Seismic survey	Broadband source level (dB re 1 μPa at 1 m)
Air-gun array (32 guns)	259 (peak)
Military SONARS	Broadband source level (dB re 1 μPa at 1 m)
AN/SQS-53C (US Navy tactical mid-frequency SONAR, center frequencies 2.6 and 3.3 kHz)	235
AN/SQS-56 (US Navy tactical mid-frequency sonar, center frequencies 6.8 to 8.2 kHz)	223
Surveillance Towed Array Sensor System Low Frequency Active (SURTASS-LFA) (100–500 Hz)	215 dB per projector, with up to 18 projectors in a vertical array operating simultaneously
Ocean acoustic studies	Broadband source level (dB re 1 μPa at 1 m)
Heard island feasibility test (HIFT) (center frequency 57 Hz)	206 dB for a single projector, with up to 5 projectors in a vertical array operating simultaneously
Acoustic thermometry of ocean climate (ATOC)/North Pacific acoustic laboratory (NPAL) (center frequency 75 Hz)	195

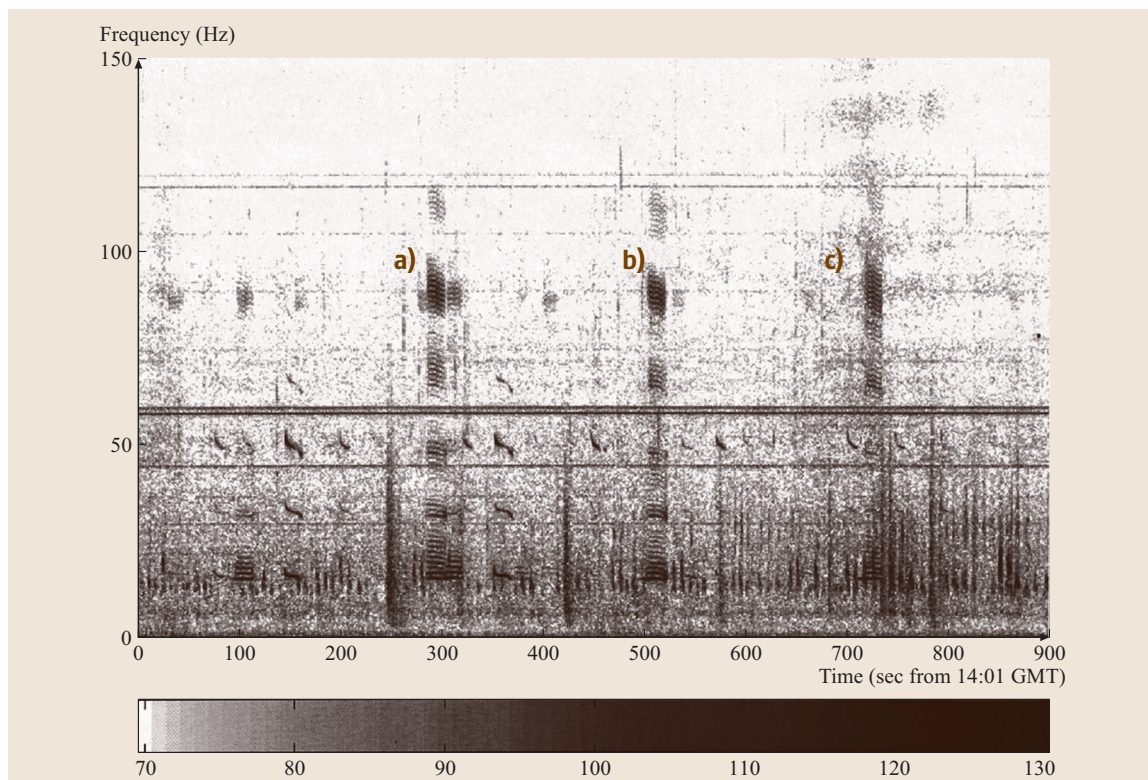


Fig. 5.59 Whale spectrogram power spectral density are in units of dB re $1 \mu\text{Pa}^2/\text{Hz}$. The blue-whale broadband signals denoted by (a), (b) and (c) are designated *type A calls*. The FM sweeps are *type B calls*. The multiple vertical energy bands between 20 and 30 Hz have the appearance of fin-whale vocalizations (after [5.109])

Marine mammal sounds span the spectrum from 10–200 000 kHz. Examples are: blue (see spectrogram in Fig. 5.59) and fin whales in the 20 Hz region with source levels as high as 190 dB, Weddell seals in the 1–10 kHz region producing 193 dB levels; bottlenose dolphin, 228 dB in a noisy background, sperm whale clicks are the loudest recorded levels at 232 dB. A list of typical levels is shown in Table 5.4. Most of the levels listed are substantial and strongly suggest acoustics as a modality for monitoring marine mammals. Thus, for example, Fig. 5.60 shows the acoustically derived track of a blue whale over 43 days and thousands of kilometers as determined from SOSUS arrays (see Introduction to this chapter) in the Atlantic Ocean.

The issues mostly dealt with in marine mammal acoustics are: understanding the physiology and behavior associated with the production and reception of sounds, and the effects that manmade sounds have on marine mammals from actual physical harm to causing changes in behavior. Physical harm includes actual

Table 5.4 Marine-mammal sound levels

Source	Broadband source level (dB re $1 \mu\text{Pa}$ at 1 m)
Sperm whale clicks	163–223
Beluga whale echo-location click	206–225 (peak to peak)
White-beaked dolphin echo-location clicks	194–219 (peak to peak)
Spinner dolphin pulse bursts	108–115
Bottlenose dolphin whistles	125–173
Fin whale moans	155–186
Blue whale moans	155–188
Gray whale moans	142–185
Bowhead whale tonals, moans and song	128–189
Humpback whale song	144–174
Humpback whale fluke and flipper slap	183–192
Southern right whale pulsive call	172–187
Snapping shrimp	183–189 (peak to peak)



52 Part A Propagation of Sound

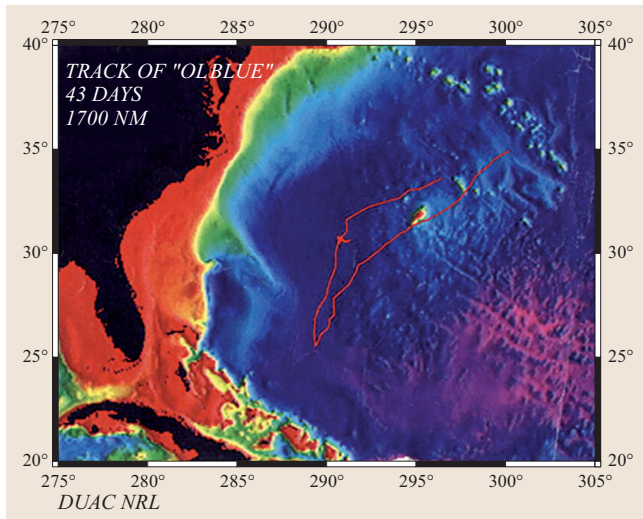


Fig. 5.60 Track of a blue whale in the Atlantic Ocean determined by US Navy personnel operating SOSUS stations. (Courtesy Clyde Nishimura, Naval Research Laboratory and Chris Clark, Cornell University) ▶

is to determine the safe levels of manmade sounds. Acoustics has now become an important research tool in the marine mammal arena ([5.110–115]).

Tables 5.3 and 5.4 have been taken from University of Rhode Island web site: <http://www.dosits.org/science/ssea/2.htm> with references to [5.24, 25, 116].

Advances in the bandwidth and data-storage capabilities of sea-floor autonomous acoustic recording packages (ARPs) have enabled the study of odontocete (toothed-whale) long-term acoustic behavior. Figure 5.61 illustrates one day of broadband (10 Hz–100 kHz) acoustic data collected in the Santa Barbara Channel. The passage of vocalizing dolphins is recorded by the aggregate spectra from their echolocation clicks (>20 kHz) and whistles (5–15 kHz). Varying proportions of clicks and whistles are seen for each

damage (acoustic trauma) and permanent and temporary threshold shifts in hearing. A major ongoing effort

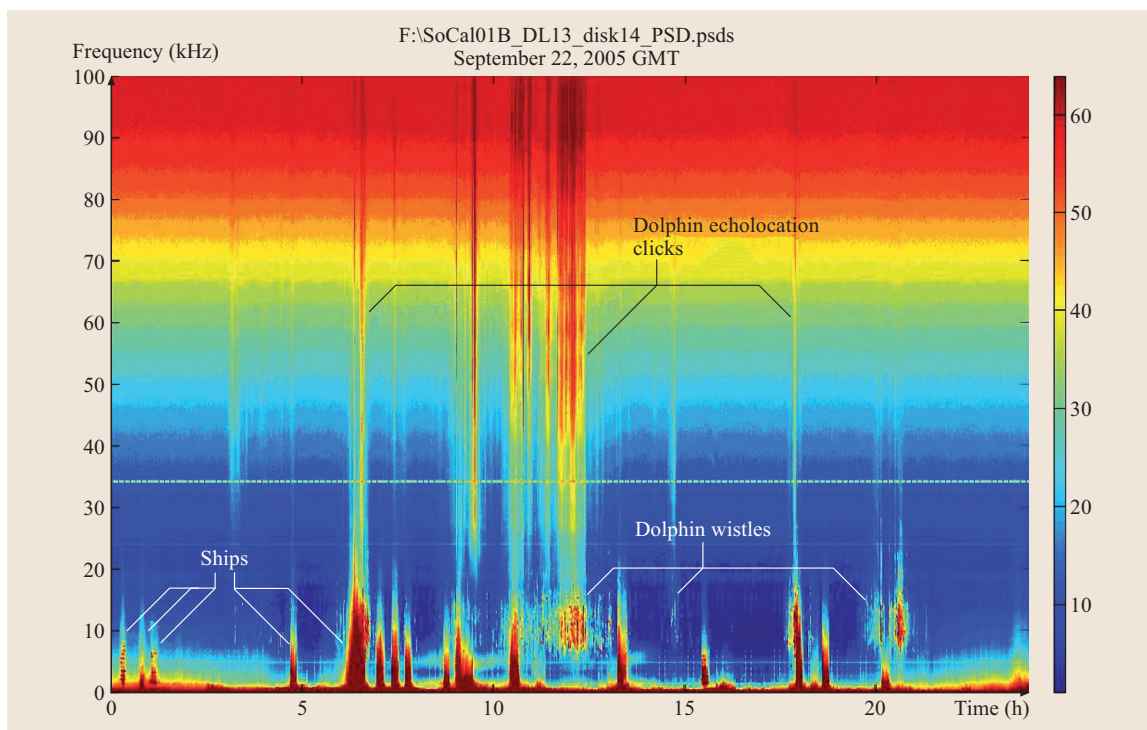


Fig. 5.61 Broadband (10 Hz–100 kHz) acoustic data collected in the Santa Barbara Channel, illustrating spectra from dolphin echolocation clicks (>20 kHz) and whistles (5–15 kHz) as seen in a daily sonogram (Sept 22, 2005). Passages of individual commercial ships are seen at mid and low frequencies (<15 kHz) (Courtesy John Hildebrand, Scripps Institution of Oceanography)



calling bout. These data allow for study of the acoustic behavior under varying conditions (day–night) and

for the determination of the seasonal presence of calling animals.

5.A Appendix: Units

The decibel (dB) is the dominant unit in underwater acoustics and denotes a ratio of intensities (not pressures) expressed in terms of a logarithmic (base 10) scale. Two intensities, I_1 and I_2 have a ratio I_1/I_2 in decibels of $10 \log I_1/I_2$ dB. Absolute intensities can therefore be expressed by using a reference intensity. The presently accepted reference intensity in underwater acoustics is based on a reference pressure of one micropascal. Therefore, taking I_2 as the intensity of a plane wave of pressure 1 μPa , a sound wave having an intensity, of, say, one million times that of a plane wave of rms pressure 1 μPa has a level of $10 \log(10^6/1) \equiv 60$ dB re 1 μPa . Pressure (p) ratios are expressed in dB re 1 μPa by taking $20 \log p_1/p_2$, where it is understood that the reference originates

from the intensity of a plane wave of pressure equal to 1 μPa .

The average intensity, I , of a plane wave with rms pressure p in a medium of density ρ and sound speed c is $I = p^2/\rho c$. In seawater, $(\rho c)_{\text{water}}$ is $1.5 \times 10^6 \text{ Pa sm}^{-1}$ so that a plane wave of rms pressure 1 μPa has an intensity of $6.76 \times 10^{-19} \text{ W/m}^2$.

For reference, we also mention the relevant units in air, where the reference pressure is related, more or less, to the minimum level of sound we can hear is. This is a pressure level 26 dB higher than the water reference. Further, since the intensity level associated with this reference is 10^{-12} W/m^2 . Therefore, one should be careful when relating units between water and air, as the latter's reference intensity is higher.

References

- 5.1 W.A. Kuperman, J.F. Lynch: Shallow-water acoustics, *Phys. Today* **57**, 55–61 (2004)
- 5.2 L.M. Brekhovskikh: *Waves in Layered Media*, 2nd edn. (Academic, New York 1980)
- 5.3 L.M. Brekhovskikh, Y.P. Lysanov: *Fundamentals of Ocean Acoustics* (Springer, Berlin, Heidelberg 1991)
- 5.4 F.B. Jensen, W.A. Kuperman, M.B. Porter, H. Schmidt: *Computational Ocean Acoustics* (Springer, Berlin, New York 2000)
- 5.5 B.G. Katsnelson, V.G. Petnikov: *Shallow Water Acoustics* (Springer, Berlin, Heidelberg 2001)
- 5.6 J.B. Keller, J.S. Papadakis (Eds.): *Wave Propagation in Underwater Acoustics* (Springer Berlin, New York 1977)
- 5.7 H. Medwin, C.S. Clay: *Fundamentals of Acoustical Oceanography* (Academic, San Diego 1997)
- 5.8 H. Medwin: *Sounds in the Sea: From Ocean Acoustics to Acoustical Oceanography* (Cambridge Univ. Press, Cambridge 2005)
- 5.9 W. Munk, P. Worcester, C. Wunsch: *Ocean Acoustic Tomography* (Cambridge Univ. Press, Cambridge 1995)
- 5.10 D. Ross: *Mechanics of Underwater Noise* (Pergamon, New York 1976)
- 5.11 B.D. Dushaw, P.F. Worcester, B.D. Cornuelle, B.M. Howe: On equations for the speed of sound in seawater, *J. Acoust. Soc. Am.* **93**, 255–275 (1993)
- 5.12 J.L. Spiesberger, K. Metzger: A new algorithm for sound speed in seawater, *J. Acoust. Soc. Am.* **89**, 2677–2688 (1991)
- 5.13 J. Northrup, J.G. Colborn: Sofar channel axial sound speed and depth in the Atlantic Ocean, *J. Geophys. Res.* **79**, 5633–5641 (1974)
- 5.14 W.H. Munk: Internal waves and small scale processes. In: *Evolution of Physical Oceanography*, ed. by B. Warren, C. Wunsch (MIT, Cambridge 1981) pp. 264–291
- 5.15 O.B. Wilson: *An Introduction to the Theory and Design of Sonar Transducers* (Government Printing Office, Washington 1985)
- 5.16 R.J. Urick: *Principles of Underwater Sound*, 3rd edn. (McGraw-Hill, New York 1983)
- 5.17 R.P. Chapman, J.R. Marchall: Reverberation from deep scattering layers in the Western North Atlantic, *J. Acoust. Soc. Am.* **40**, 405–411 (1966)
- 5.18 J.A. Ogilvy: Wave scattering from rough surfaces, *Rep. Prog. Phys.* **50**, 1553–1608 (1987)
- 5.19 E.I. Thorsos: Acoustic scattering from a "Pierson-Moskowitz" sea surface, *J. Acoust. Soc. Am.* **89**, 335–349 (1990)
- 5.20 P.H. Dahl: On bistatic sea surface scattering: Field measurements and modeling, *J. Acoust. Soc. Am.* **105**, 2155–2169 (1999)
- 5.21 R.P. Chapman, H.H. Harris: Surface backscattering strengths measured with explosive sound sources, *J. Acoust. Soc. Am.* **34**, 1592–1597 (1962)
- 5.22 M. Nicholas, P.M. Ogden, F.T. Erskine: Improved empirical descriptions for acoustic surface backscatter in the ocean, *IEEE J. Ocean. Eng.* **23**, 81–95 (1998)

- 5.23 N.C. Makris, S.C. Chia, L.T. Fialkowski: The bi-azimuthal scattering distribution of an abyssal hill, *J. Acoust. Soc. Am.* **106**, 2491–2512 (1999)
- 5.24 G.M. Wenz: Acoustics ambient noise in the ocean: spectra and sources, *J. Acoust. Soc. Am.* **34**, 1936–1956 (1962)
- 5.25 R.K. Andrew, B.M. Howe, J.A. Mercer, M.A. Dzieciuch: Ocean ambient sound: Comparing the 1960s with the 1990s for a receiver off the California coast, *Acoust. Res. Lett. Online* **3**(2), 65–70 (2002)
- 5.26 M.A. McDonald, J.A. Hildebrand, S.W. Wiggins: Increases in deep ocean ambient noise in the Northeast Pacific west of San Nicolas Island, California, *J. Acoust. Soc. Am.* **120**, 711–718 (2006)
- 5.27 W.A. Kuperman, F. Ingenito: Spatial correlation of surface generated noise in a stratified ocean, *J. Acoust. Soc. Am.* **67**, 1988–1996 (1980)
- 5.28 T.G. Leighton: *The Acoustic Bubble* (Academic, London 1994)
- 5.29 C.E. Brennen: *Cavitation and Bubble Dynamics* (Oxford Univ. Press, Oxford 1995)
- 5.30 G.B. Morris: Depth dependence of ambient noise in the Northeastern Pacific Ocean, *J. Acoust. Soc. Am.* **64**, 581–590 (1978)
- 5.31 V.C. Anderson: Variations of the vertical directivity of noise with depth in the North Pacific, *J. Acoust. Soc. Am.* **66**, 1446–1452 (1979)
- 5.32 F. Ingenito, S.N. Wolf: Acoustic propagation in shallow water overlying a consolidated bottom, *J. Acoust. Soc. Am.* **60**(6), 611–617 (1976)
- 5.33 H. Schmidt, W.A. Kuperman: Spectral and modal representation of the Doppler-shifted field in ocean waveguides, *J. Acoust. Soc. Am.* **96**, 386–395 (1994)
- 5.34 M.D. Collins, D.K. Dacol: A mapping approach for handling sloping interfaces, *J. Acoust. Soc. Am.* **107**, 1937–1942 (2000)
- 5.35 W.A. Kuperman, G.L. D'Spain (Eds.): *Ocean Acoustics Interference Phenomena and Signal Processing* (American Institution of Physics, Melville 2002)
- 5.36 H.L. Van Trees: *Detection Estimation and Modulation Theory* (Wiley, New York 1971)
- 5.37 H.L. Van Trees: *Optimum Array Processing* (Wiley, New York 2002)
- 5.38 D.H. Johnson, D.E. Dudgeon: *Array Signal Processing: Concepts and Techniques* (Prentice Hall, Englewood Cliffs 1993)
- 5.39 G.L. D'Spain, J.C. Luby, G.R. Wilson, R.A. Gramann: Vector sensors and vector line arrays: Comments on optiman array gain and detection, *J. Acoust. Soc. Am.* **120**, 171–185 (2006)
- 5.40 P. Roux, W.A. Kuperman, NPAL Group: Extracting coherent wavefronts from acoustic ambient noise in the ocean, *J. Acoust. Soc. Am.* **116**, 1995–2003 (2004)
- 5.41 M. Siderius, C.H. Harrison, M.B. Porter: A passive fathometer for determing bottom depth and imaging seabed layering using ambient noise, *J. Acoust. Soc. Am.* **12**, 1315–1323 (2006)
- 5.42 A.B. Baggeroer, W.A. Kuperman, P.N. Mikhalevsky: An Overview of matched field methods in ocean acoustics, *IEEE J. Ocean. Eng.* **18**(4), 401–424 (1993)
- 5.43 W.A. Kuperman, D.R. Jackson: Ocean acoustics, matched-field processing and phase conjugation. In: *Imaging of complex media with acoustic and seismic waves*, Topics in Applied Physics, Vol. 84, ed. by M. Fink, W.A. Kuperman, J.-P. Montagner, A. Tourin (Springer, Berlin, Heidelberg 2002) pp. 43–97
- 5.44 M. Fink: Time reversed physics, *Phys. Today* **50**, 34–40 (1997)
- 5.45 A. Parvelescu, C.S. Clay: Reproducibility of signal transmissions in the ocean, *Radio Electron. Eng.* **29**, 223–228 (1965)
- 5.46 W.A. Kuperman, W.S. Hodgkiss, H.C. Song, T. Akal, C. Ferla, D. Jackson: Phase conjugation in the ocean: Experimental demonstration of an acoustical time-reversal mirror in the ocean, *J. Acoust. Soc. Am.* **102**, 25–40 (1998)
- 5.47 H. Cox, R.M. Zeskind, M.O. Owen: Robust Adaptive Beamforming, *IEEE Trans. Acoust. Speech Signal Proc.* **35**, 10 (1987)
- 5.48 J.L. Krolik: Matched-field minimum variance beamforming in a random ocean channel, *J. Acoust. Soc. Am.* **92**, 1408–1419 (1992)
- 5.49 A. Tolstoy, O. Diachok, L.N. Frazer: Acoustic tomography via matched field processing, *J. Acoust. Soc. Am.* **89**, 1119–1127 (1991)
- 5.50 A.B. Baggeroer: *Applications of Digital Signal Processing*, ed. by A.V. Oppenheim (Prentice Hall, Englewood Cliffs 1978)
- 5.51 C. De Moustier: Beyond bathymetry: mapping acoustic backscattering from the deep seafloor with Sea Beam, *J. Acoust. Soc. Am.* **79**, 316–331 (1986)
- 5.52 P. Cervenka, C. De Moustier: Sidescan sonar image processing techniques, *IEEE J. Ocean. Eng.* **18**, 108–122 (1993)
- 5.53 C. De Moustier, H. Matsumoto: Seafloor acoustic remote sensing with multibeam echo-sounders and bathymetric sidescan sonar systems, *Marine Geophys. Res.* **15**, 27–42 (1993)
- 5.54 A. Turgut, M. McCord, J. Newcomb, R. Fisher: *Chirp sonar sediment characterization at the northern Gulf of Mexico Littoral Acoustic Demonstration Center experimental site*, Proc. OCEANS 2002 MTS/IEEE Conf. (IEEE, New York 2002)
- 5.55 D.B. Kilfoyle, A.B. Baggeroer: The state of the art in underwater acoustic telemetry, *IEEE J. Ocean. Eng.* **25**(1), 4–27 (2000)
- 5.56 D.B. Kilfoyle, J.C. Preissig, A.B. Baggeroer: Spatial modulation of partially coherent multiple-input/multiple-output channels, *IEEE Trans. Signal Proc.* **51**, 794–804 (2003)
- 5.57 C.E. Shannon: A mathematical theory of communication, *Bell Syst. Tech. J.* **27**, 379 (1948)

- 5.58 S.H. Simon, A.L. Moustakas, M. Stoychev, H. Safar: Communication in a disordered world, *Phys. Today* **54**(9) (2001)
- 5.59 G. Raleigh, J.M. Cioffi: Spatio-temporal coding for wireless communication, *IEEE Trans. Commun.* **46**, 357–366 (1998)
- 5.60 G.J. Foschini, M.J. Gans: On limits of wireless communications in a fading environment whe using multiple antennas, *Wireless Personnal Communications* **6**, 311–335 (1998)
- 5.61 C. Berrou, A. Glavieux: Near optimum error correcting coding and decoding: turbo-codes, *IEEE Trans. Commun.* **2**, 1064–1070 (1996)
- 5.62 J.G. Proakis: *Digital Communications* (McGraw Hill, New York 1989)
- 5.63 M. Stojanovich: Retrofocusing techniques for high rate acoustic communications, *J. Acoust. Soc. Am.* **117**, 1173–1185 (2005)
- 5.64 H.C. Song, W.S. Hodgkiss, W.A. Kuperman, M. Stevenson, T. Akal: Improvement of time-reversal communications using adaptive channel equalizers, *IEEE J Ocean. Eng.* **31**, 487–496 (2006)
- 5.65 T.C. Yang: Temporal resolution of time-reversal and passive-phase onjugation for underwater acoustic communications, *IEEE J. Ocean. Eng.* **28**, 229–245 (2003)
- 5.66 C. Wunsch: *The ocean circulation inverse problem* (Cambridge Univ. Press, Cambridge 1996)
- 5.67 E.K. Skarsoulis, B.D. Cornuelle: Travel-time sensitivity kernels in ocean acoustic tomography, *J. Acoust. Soc. Am.* **116**, 227 (2004)
- 5.68 T.G. Birdsall, K. Metzger, M.A. Dzieciuch: Signals, signal processing, and general results, *J. Acoust. Soc. Am.* **96**, 2343 (1994)
- 5.69 P.N. Mikhalevsky, A.B. Baggeroer, A. Gavrilov, M. Slavinsky: Continuous wave and M-sequence transmissions across the Arctic, *J. Acoust. Soc. Am.* **96**, 3235 (1994)
- 5.70 B.M. Howe, P.F. Worcester, R.C. Spindel: Ocean acoustic tomography: Mesoscale velocity, *J. Geophys. Res.* **92**, 3785–3805 (1987)
- 5.71 R.A. Knox: Ocean acoustic tomography: A primer. In: *Ocean Circulation Models: Combining Data and Dynamics*, ed. by D.L.T. Anderson, J. Willebrand (Kluwer Academic, Dordrecht 1989)
- 5.72 M.I. Taroudakis: Ocean Acoustic Tomography, Lect. Notes ECUA, 77–95 (2002)
- 5.73 A.J.W. Duijndam, M.A. Schoneville, C.O.H. Hindriks: Reconstruction of band-limited signals, irregularly sampled along one spatial direction, *Geophysics* **64**(2), 524–538 (1999)
- 5.74 U. Send, The THETIS-2 Group: Acoustic observations of heat content across the Mediterranean Sea, *Nature* **38**, 615–617 (1997)
- 5.75 J.A. Colosi, E.K. Scheer, S.M. Flatté, B.D. Cornuelle, M.A. Dzieciuch, W.H. Munk, P.F. Worcester, B.M. Howe, J.A. Mercer, R.C. Spindel, K. Metzger, T.G. Birdsall, A.B. Baggeroer: Comparisons of meas-ured and predicted acoustic fluctuations for a 3250 km propagation experiment in the eastern North Pacific Ocean, *J. Acoust. Soc. Am.* **105**, 3202–3218 (1999)
- 5.76 J.A. Colosi, A.B. Baggeroer, B.D. Cornuelle, M.A. Dzieciuch, W.H. Munk, P.F. Worcester, B.D. Dushaw, B.M. Howe, J.A. Mercer, R.C. Spindel, T.G. Birdsall, K. Metzger, A.M.G. Forbes: Analysis of multipath acoustic field variability and coherence in the finale of broadband basin-scale transmissions in the North Pacific Ocean, *J. Acoust. Soc. Am.* **117**, 1538–1564 (2005)
- 5.77 M. De Hoop, R. van der Hilst: On sensitivity kernels for wave equation transmission tomography, *Geophys. J. Int.* **160**, 621–633 (2005)
- 5.78 R. van der Hilst, M. de Hoop: Banana-doughnut kernels and mantle tomography, *Geophys. J. Int.* **163**, 956–961 (2005)
- 5.79 F. Dahlen, G. Nolet: Comment on the paper on sensitivity kernels for wave equation transmission tomography by de Hoop and van der Hilst, *Geophys. J. Int.* **163**, 949–951 (2005)
- 5.80 K.A. Johannesson, R.B. Mitson: *Fisheries acoustics – A practical manual for aquatic biomass estimation*, FAO Fish. Tech. Paper 240 (FAO, Rome 1983)
- 5.81 G.L. Thomas: *Fisheries Acoustics, Special Issue, Fish. Res.* **14**(2/3) (Elsevier, Amsterdam 1992)
- 5.82 A. Duncan: *Shallow Water Fisheries Acoustics* 35(1/2) (Elsevier, Amsterdam 1998), Please check this reference. Is this a reference to a contribution in a proceeding/to the proceedings of a conference as a whole?
- 5.83 B.J. Robinson: Statistics of single fish echoes observed at sea, *ICES C. M. B* **16**, 1–4 (1976)
- 5.84 D. B.Reeder, J.M. Jech, T.K. Stanton: Broadband acoustic backscatter and high-resolution morphology of fish: Measurement and modeling, *J. Acoust. Soc. Am.* **116**, 2489 (2004)
- 5.85 A. Alvarez, Z. Ye: Effects of fish school structures on acoustic scattering, *ICES J. Marine Sci.* **56**(3), 361–369 (1999)
- 5.86 D. Reid, C. Scalabrin, P. Petitgas, J. Masse, R. Aukland, P. Carrera, S. Georgakarakos: Standard protocols for the analysis of school based data from echo sounder surveys, *Fish. Res.* **47**(2/3), 125–136 (2000)
- 5.87 D.V. Holliday: Resonance structure in echoes from schooled pelagic fish, *J. Acoust. Soc. Am.* **51**, 1322–1332 (1972)
- 5.88 D.N. MacLennan: Acoustical measurement of fish abundance, *J. Acoust. Soc. Am.* **87**(1), 1–15 (1990)
- 5.89 D.N. Mac Lennan, E.J. Simmonds: *Fisheries Acoustics* (Chapman Hall, London 1992)
- 5.90 P. Petitgas: A method for the identification and characterization of clusters of schools along the transect lines of fisheries-acoustic surveys, *ICES J. Marine Sci.* **60**(4), 872–884 (2003)

- 5.91 Y. Takao, M. Furusawa: Dual-beam echo integration method for precise acoustic surveys, *ICES J. Marine Sci.* **53**(2), 351–358 (1996)
- 5.92 E. Marchal, P. Petitgas: Precision of acoustic fish stock estimates: separating the number of schools from the biomass in the schools, *Aquat. Living Res.* **6**(3), 211–219 (1993)
- 5.93 T.K. Stanton: Effects of transducer motion on echo-integration techniques, *J. Acoust. Soc. Am.* **72**, 947–949 (1982)
- 5.94 K.G. Foote, H.P. Knudsen, G. Vestnes, D.N. MacLennan, E.J. Simmonds: Calibration of acoustic instruments for fish density estimation: a practical guide, *ICES Coop. Res. Rep.* **144**, 69 (1987)
- 5.95 K.G. Foote: Energy in acoustic echoes from fish aggregations, *Fish. Res.* **1**, 129–140 (1981)
- 5.96 P. Petitgas, D. Reid, P. Carrera, M. Iglesias, S. Georgakarakos, B. Liorzou, J. Massé: On the relation between schools, clusters of schools, and abundance in pelagic fish stocks, *ICES J. Marine Sci.* **58**(6), 1150–1160 (2001)
- 5.97 K.G. Foote: Linearity of fisheries acoustics, with addition theorems, *J. Acoust. Soc. Am.* **73**(6), 1932–1940 (1983)
- 5.98 F. Gerlotto, M. Soria, P. Freon: From two dimensions to three: the use of multibeam sonar for a new approach in fisheries acoustics, *Can. J. Fish. Aquat. Sci.* **56**, 6–12 (1999)
- 5.99 L. Mayer, Y. Li, G. Melvin: 3D visualization for pelagic fisheries research and assessment, *ICES J. Marine Sci.* **59**(1), 216–225 (2002)
- 5.100 C. Scalabrin, N. Diner, A. Weill, A. Hillion, M.-C. Mouchot: Narrowband acoustic identification of monospecific fish shoals, *ICES J. Marine Sci.* **53**, 181–188 (1996)
- 5.101 J. Guillard, P. Brehmer, M. Colon, Y. Guennegan: 3-D characteristics of young-of-year pelagic fish schools in lake, *Aqu. Liv. Res.* **19**, 115–122 (2006)
- 5.102 K.G. Foote: Fish target strengths for use in echo integrator surveys, *J. Acoust. Soc. Am.* **82**, 981 (1987)
- 5.103 E. Josse, A. Bertrand: In situ acoustic target strength measurements of tuna associated with a fish aggregating device, *ICES J. Marine Sci.* **57**(4), 911–918 (2000)
- 5.104 B.J. Robinson: *In situ measurements of the target strengths of pelagic fishes, ICES/FAO Symp. Fish. Acoust* (FAO, Rome 2000) pp. 1–7
- 5.105 S. Gauthier, G.A. Rose: Target strength of encaged Atlantic redfish, *ICES J. Marine Sci.* **58**, 562–568 (2001)
- 5.106 J.S. Jaffe: Target localization for a three-dimensional multibeam sonar imaging system, *J. Acoust. Soc. Am.* **105**(6), 3168–3175 (1999)
- 5.107 D.V. Holliday, R.E. Pieper: Volume scattering strengths and zooplankton distributions at acoustic frequencies between 0.5 and 3 MHz, *J. Acoust. Soc. Am.* **67**, 135 (1980)
- 5.108 C.F. Greenlaw, D.V. Holliday, D.E. McGehee: Multi-static, multifrequency scattering from zooplankton, *J. Acoust. Soc. Am.* **103**, 3069 (1998)
- 5.109 A.M. Thode, G.L. D'Spain, W.A. Kuperman: Mathed-field processing, geoacoustic inversion, and source signature recovery of blue whale vocalizations, *J. Acoust. Soc. Am.* **107**, 1286–1300 (2000)
- 5.110 M. Johnson, P. Tyack, D. Nowacek: A digital recording tag for measuring the response of marine mammals to sound, *J. Acoust. Soc. Am.* **108**, 2582–2583 (2000)
- 5.111 D.K. Mellinger, K.M. Stafford, G.C. Fox: Seasonal occurrence of sperm whale (*Physeter macrocephalus*) sounds in the Gulf of Alaska, 1999–2001, *Marine Mammal Sci.* **20**(1), 48–62 (2004)
- 5.112 W.J. Richardson, C.R. Greene, C.I. Malme, D.H. Thomson: *Marine Mammals and Noise* (Academic, San Diego 1995)
- 5.113 A. Sirovic, J.A. Hildebrand, S.M. Wiggins, M.A. McDonald, S.E. Moore, D. Thiele: Seasonality of blue and fin whale calls and the influence of sea ice in the western Antarctic peninsula, *Deep Sea Res.* **51**(II), 2327–2344 (2004)
- 5.114 A.M. Thode, D.K. Mellinger, S. Stienessen, A. Martinez, K. Mullin: Depth-dependent acoustic features of diving sperm whales (*Physeter macrocephalus*) in the Gulf of Mexico, *J. Acoust. Soc. Am.* **112**, 308–321 (2002)
- 5.115 P. Tyack: Acoustics communications under the sea. In: *Animal Acoustic Communication: Recent Advances*, ed. by S.L. Hopp, M.J. Owren, C.S. Evans (Springer, Berlin, Heidelberg 1988) pp. 163–220
- 5.116 National Research Council: *Ocean Noise and Marine Mammals* (National Academy, Washington 2003) p. 192